Diss. ETH NO. 26894

COMPLEX POLAR STATES IN ULTRATHIN EPITAXIAL OXIDES

A thesis submitted to attain the degree of

DOCTOR OF SCIENCES of ETH ZURICH

(Dr. sc. ETH Zurich)

presented by

JOHANNA NORDLANDER

M. Sc., Lund University

born on 28.02.1991

citizen of Sweden

accepted on the recommendation of

Prof. Dr. Manfred Fiebig
Dr. Morgan Trassin
Prof. Dr. Beatriz Noheda
Prof. Dr. Kathrin Dörr

2020

Declaration of Originality

I hereby declare that the following submitted thesis is original work which I alone have authored and which is written in my own words.

Title:	Complex polar states in ultrathin epitaxial oxides
Author:	Johanna Nordlander
Supervisor:	Prof. Dr. Manfred Fiebig

With my signature I declare that I have been informed regarding normal academic citation rules and that I have read and understood the information on "Citation etiquette". The citation conventions usual to the discipline in question here have been respected.

Furthermore, I declare that I have truthfully documented all methods, data, and operational procedures and not manipulated any data. All persons who have substantially supported me in my work are identified in the acknowledgments.

The above work may be tested electronically for plagiarism.

Zürich, 24.05.2020

Johanna Nordlander

Acknowledgment

This work was only made possible because of the great support of my colleagues, friends and family. I am deeply grateful to all of you.

First of all, I would like to thank Prof. Manfred Fiebig and Dr. Morgan Trassin for advising and mentoring me during the past four years, helping me navigate the many facets that make up academic research. I thank you both for giving me the opportunity to work with you on a groundbreaking experimental setup in the first place, and for always being open to discuss new ideas and directions throughout my PhD. For participating on my thesis committee, I additionally would like to thank Prof. Beatriz Noheda, Prof. Kathrin Dörr and Prof. Ralph Spolenak.

This thesis is the product of many great, often international, collaborations and it has been my pleasure to work with so many talented scientists. While all collaborators that contributed to this work are specifically highlighted in the Contributions chapter, some special mentions are in order also here. I want to thank Dr. Gabriele De Luca for introducing me to the laser-optical setup in general and SHG on thin films in particular, and Nives Strkalj for sharing with me our initial struggles with understanding, (re-)building and optimizing in-situ SHG such that it can reveal all we want to know and more about our ferroelectric thin films. I also want to thank Dr. Marta Rossell and Dr. Marco Campanini for the extensive STEM analysis, in particular the temperature-dependent imaging, of my improper ferroelectric films. Furthermore, I would like to thank Prof. Nicola Spaldin, Dr. Andres Cano and Dr. Thomas Lottermoser for enlightening discussions on polarization and other order parameters.

I have had the fortune to work alongside great people in the FERROIC group – all past and present members – including the NEAT lab, in which all our discussions on amazing, weird, bad, disappointing, successful and surprising results have contributed greatly to my view and understanding of complex oxide thin films. Beyond science and research, however, I would like to extend a special thank you to all the FERROICs for creating a fun and supportive environment also outside the work bubble. Pub nights, movie nights, hikes and SOLA runs! On this note, I am also deeply grateful to my unihockey team at Floorball Zurich Lioness for taking me in two years ago even though I only understood a handful of words in Swiss German. Unihockey has been a great counterweight allowing me some life–work balance and

Abstract

The diverse functional properties of transition-metal oxides have given rise to entire fields of research spanning fundamental aspects such as quantum phenomena to the highly applied field of oxide electronics. In the latter, electrically ordered oxides, such as ferroelectrics, stand out as prominent materials for implementation in low-energy-consuming oxide applications due to their characteristic response under the application of mechanical stress, electric field or optical irradiation.

The significant progress in oxide thin-film engineering over the last 20 years has enabled studies of such oxide functionality to go beyond bulk crystals and include characterization under confinement of the materials to the nanoscale. However, in epitaxially grown ultrathin films, the manifestation of electric polarization specifically and functionality in general can greatly differ from the behavior of the corresponding bulk crystals. In order to make use of the exotic functionality of ultrathin oxide films, it is therefore essential to understand when and how the polar states are set with respect to the thin-film synthesis and, upon implementation in electronic devices, with respect to device operation. This is however a challenging task. So far, detailed understanding of the ultrathin limit of polarity in oxide thin films remains restricted to a few model systems.

In this thesis, we present an approach to probe such polar states in ultrathin oxide layers with high sensitivity and in a nondestructive manner by nonlinear optics. We demonstrate the of use optical second harmonic generation both *in situ*, during thin-film synthesis, and *operando*, during device operation, to provide unique insight into the evolution of polar states in oxide films in these highly dynamic environments. Here, we focus on a set of oxide materials whose polar architecture becomes particularly involved in the nanometer limit. We first establish the sensitivity of our optical probe to distinguish between differently oriented polar states with a complex nanoscale microstructure in a single-phase material, and its evolution under electric-field application. We next exploit this sensitivity to follow the phase coexistence of emergent polar phases in an epitaxially strained system during the thin-film synthesis process. We thus obtain novel insight into an unusually robust, yet metastable high-temperature polar phase. We further investigate the peculiar coupling between polarization and structural order in a so-called improper ferroelectric in the ultrathin regime. Here, a combination of nonlinear optics and electron microscopy could

reveal the crucial impact of epitaxial interfaces on the evolution of polarization. Finally, we reveal emergent symmetry-breaking in layered oxides during epitaxial growth, allowing the nanoscale design of symmetry and functionality beyond polar compounds.

Common to all of these systems, we find that the mechanical and electrostatic boundary conditions set during the thin-film synthesis itself dictates the emergence of electric polarity in the oxide films, which can even result in the emergence of new material phases that are unique to the thin-film geometry and do not have a bulk counterpart. The results presented in this thesis hence point to the many possibilities of designing ultrathin oxides with unique, yet robust, polar properties of interest for both oxide electronics applications and the emergent field of thin-film quantum materials.

Zusammenfassung

Die vielfältigen funktionalen Eigenschaften von Übergangsmetalloxiden bilden die Grundlage für ganze Forschungsfelder, die von fundamentalen Aspekten der Quantenphysik bis hin zum anwendungsnahen Gebiet der Oxidelektronik reichen. Insbesondere in der Oxidelektronik stechen elektrisch geordnete Oxide, wie Ferroelektrika, hervor, die aufgrund ihres charakteristischen Verhaltens unter mechanischer Belastung, elektrischen Feldern oder optischer Bestrahlung herausragende Materialien für den Einsatz in energiesparenden Oxidanwendungen darstellen.

Über die Charakterisierung von makroskopischen Einkristallen hinausgehend, haben bedeutende Fortschritte in der Oxid-Dünnfilmtechnik in den letzten 20 Jahren Untersuchungen von Proben ermöglicht, die in einer Dimension of wenige Nanometer beschränkt sind. Unter derartigen Beschränkungen können sich jedoch sowohl die Entstehung der Polarisation als auch die allgemeinen Eigenschaften eines epitaktisch gewachsenen Dünnfilms stark vom Verhalten der entsprechenden Einkristalle unterscheiden. Um die exotischen Funktionalitäten ultradünner Oxidschichten nutzen zu können, ist es daher unerlässlich zu verstehen, wann und wie ein polarer Zustand während der Dünnschichtsynthese und, bei der Implementierung in elektronische Anwendungen, während des Betriebs definiert wird. Dies ist jedoch eine herausfordernde Aufgabe. Bislang ist ein detailliertes Verständnis der ultradünnen Form der Polarität auf einige wenige Modellsysteme beschränkt.

In dieser Arbeit stellen wir einen neuen Ansatz vor um solche polaren Zustände in ultradünnen Oxidschichten mittels nichtlinearer Optik zerstörungsfrei und mit hoher Sensitivität zu untersuchen. Wir nutzen optische Frequenzverdopplung sowohl *in situ* während der Dünnschichtsynthese als auch *operando* während des Betriebs eines Bauelements, um einen einzigartigen Einblick in die Entwicklung polarer Zustände in Oxidschichten in diesen hochdynamischen Umgebungen zu erhalten. Hier konzentrieren wir uns auf eine Reihe von Oxidmaterialien, deren polare Architektur im Nanometerbereich besonders herausfordernd ist. Zunächst demonstrieren wir anhand eines einphasigen Materials mit einer komplexen Mikrostruktur im Nanometerbereich die Sensitivität unserer optischen Methode bezüglich unterschiedlich orientierter polarer Zustände und ihrer Entwicklung in elektrischen Feldern. Anschliessend nutzen wir diese Sensitivität, um die Phasenkoexistenz emergenter polarer Phasen in einem epitaktisch verspannten System während der

Dünnschichtsynthese zu verfolgen. Auf diese Weise erhalten wir neue Einblicke in eine ungewöhnlich robuste, aber dennoch metastabile polare Hochtemperaturphase. Wir untersuchen weiter die eigentümliche Kopplung zwischen Polarisation und struktureller Ordnung im ultradünnen Regime in einem sogenannten uneigentlichen Ferroelektrikum. Die Kombination von nichtlinearer Optik und Elektronenmikroskopie zeigt hier den entscheidenden Einfluss von epitaktischen Grenzflächen auf die Evolution der Polarisation auf. Abschliessend decken wir eine emergente Form der Symmetriebrechung in geschichteten Oxiden während des epitaktischen Wachstums auf, was die Gestaltung von Symmetrie und Funktionalität im Nanometerbereich über polare Verbindungen hinaus ermöglicht.

In all diesen Systemen diktieren mechanische und elektrostatische Randbedingungen, die während der Dünnschichtsynthese definiert werden, die Entwicklung elektrischer Polarität in den Oxidschichten. Dies kann sogar zur Ausprägung neuer Materialphasen führen kann, die nur in der Dünnschichtgeometrie existieren und kein makroskopisches Gegenstück haben. Die in dieser Arbeit vorgestellten Ergebnisse weisen daher auf die vielen Möglichkeiten hin, ultradünne Oxide mit einzigartigen, jedoch robusten, polaren Eigenschaften zu entwerfen, die sowohl für Anwendungen in der Oxid-Elektronik als auch für den aufkommenden Bereich der Dünnschicht-Quantenmaterialien von Interesse sind.

Contents

Introduction

At the heart of materials science lies the strive to design *functional* materials [1–4]. A material can be deemed functional if it exhibits properties that can be set by design and changed on demand, such that they can perform a specific function. In everyday life, functional materials are found both in large-scale construction and in the very smallest devices in nanotechnology: they appear as reinforcement of concrete [5, 6], in self-cleaning coatings [7, 8], and in sensors such as thermometers [9–11], gas detectors [12], solar cells [13, 14] and microphones [15, 16]. In microelectronics, functional materials are used for rechargeable batteries [17–19], data storage [20, 21] and touchscreens [22] , to name just a few. The age of functional materials is, however, only in its infancy, and this field is envisioned to revolutionize the way we live in a similar manner as the silicon-based electronics industry did. We imagine a single, 'smart' material that can replace what now requires a complex system of interconnected devices.

At the very smallest of length scales, state-of-the-art nanotechnology has seen the field of oxide electronics emerging [23–26], making use of the many and versatile functional properties found in crystalline complex oxides. Current research envisions the design of advanced electronic oxides that can emulate the learning process of a brain to efficiently process large amounts of data [27, 28], that can process information carried by electric fields or light rather than electric current [29], and that can host circuitry which can be rewritten on demand for reconfigurable devices [30]. However, many of these inventions still remain on a conceptual level, and the search for new functionality in oxide materials is an ongoing quest.

This thesis specifically explores polar properties found in ultrathin transition-metal oxide films only a few nanometers in thickness. The transition-metal oxides constitute a class of materials that shows a next to infinite range of functional properties that can be accessed or tuned by small perturbations to the systems [31–33]. Due to their strongly correlated electronic structure, a small change in strain, chemical composition, temperature, etc., may result in vastly different functional properties, spanning insulating, conducting, and superconducting states [34, 35]; catalytic activity [36]; strong light-matter interactions; and magnetic and electric long-range order [37]. All this makes transition-metal oxides the playground of choice for designing novel oxide-based electronics applications.

1

The basis for all these functional properties resides in the specific microstructure of the material. In crystalline materials such as oxides, the positions of the constituent atoms are ordered. The atoms sit in a certain, periodic pattern: a lattice. Superimposed on this crystallographic lattice are also the electronic and magnetic states of the constituent atoms, which exhibit their own periodic pattern, defining the electronic and magnetic sublattices. Their combined configuration in a given material defines its macroscopic properties. In particular, a change in such periodicity, meaning a change of *symmetry*, leads to a corresponding change in properties [38].

Many functional properties appear only in materials that lack inversion symmetry [39], that is, in materials that do not appear the same when you flip them around. This is, for example, the case for a battery with its opposite poles. In technology, this lack of inversion symmetry can be used to define states of a device. In the simplest example, we can use the polarity of a material to define '0' and '1' or 'on' and 'off'. Since materials with such polar states also exhibit characteristic responses to electrical and optical fields, they are envisioned to find their use in novel electronic and photonic applications, in particular at the nanoscale [40].

To be compatible with current nanotechnological applications, functional oxides are usually implemented in devices in the form of ultrathin films only a few nanometers in thickness. Due to the finite size and strong confinement of such thin-film systems, their functional properties can behave very differently than in the case of a bulk crystal. On the other hand, the unprecedented control in state-of-the-art oxide thin-film synthesis also allows precise tuning and manipulation of the thin-film material at the atomic scale, beyond what is possible in bulk crystals [41].

The polar properties of oxide thin films have been subjected to intense research in the last years in terms of both fundamental physical phenomena and prospective technological applications [42, 43]. Here, we seek to illuminate the unique manifestation and modification of such functionality in the limit of ultrathin oxide films. In an experimental approach, we will combine state-of-the-art thin-film deposition and characterization techniques for both *in-situ* and *operando* studies of complex polar states in transition-metal oxide films that are envisioned for applications in the emerging field of oxide-based electronics. We seek to go beyond understanding the ultrathin regime manifestation of polar states in comparison to their behavior in bulk crystals; we also aim to understand the control of these polar states in oxide thin films, such that we can set their polar functionality by design.

This thesis exploits the characteristic nonlinear-optical response exhibited by polar oxides to probe their functional properties [44]. Due to the non-invasive nature of optical probing, this method is perfectly suited for *operando* or *in-situ* studies of polar states at the moment of their formation, such as during thin-film synthesis, or modification, such as during application of electric fields. This work highlights the origin of polar properties found in complex oxide thin films beyond what is expected based on their bulk counterparts. Here, we provide insight into the emergence

of, and mutual interaction between, coexisting polar states and their impact on the functional properties of ultrathin epitaxial films. We furthermore explore new material classes for engineering polar properties beyond conventional ferroelectric systems. Ultimately, this work demonstrates how controlling symmetry aspects at the nanoscale can reveal novel polar functionality in ultrathin oxides beyond what is possible in the bulk.

This thesis is outlined as follows:

Chapter 1 serves as a brief introduction to the general topic of polar states in functional oxides, with a focus on their manifestation in thin films. It furthermore presents the specific polar oxide materials investigated in this work.

Chapters 2 and 3 introduce the methods used for thin-film synthesis and characterization of structural and functional properties. Specifically, **Chapter 2** covers the thin-film growth and all structural characterization techniques except optical second harmonic generation, which due to its role as main characterization method of this work is presented in **Chapter 3**. It details the use of laser-optical second harmonic generation as a probe of polar states in epitaxial thin films. It covers a general introduction, thin-film specific considerations and finally, it presents the implementation of the optical probe with the thin-film deposition system to enable *in-situ* measurements for polar states directly in the growth environment, establishing the novel field of in-situ SHG.

Chapters 4 to 8 present the investigation of coexisting polar states in different oxide thin film systems. The chapters are ordered by increasing complexity of the polar states investigated. Beginning in **Chapter 4** with a prototypical ferroelectric, $BaTiO_3$, we investigate the coexistence and distinction of ferroelectric domains with in-plane- and out-of-plane-oriented spontaneous polarization states when the films are integrated on technologically relevant silicon substrates. In **Chapter 5**, we move to a slightly more complex ferroelectric system, namely $BiFeO_3$ films grown close to the strain-driven morphotropic phase boundary. Here, we investigate polar properties in relation to emergent phase coexistence between tetragonal-like and rhombohedral-like monoclinic phases. Moving beyond the conventional ferroelectric polar states, we spend **Chapters 6 and 7** on discussing the thin-film manifestation of improper ferroelectricity in hexagonal $YMnO_3$, where the polarization state is driven by a another polar, yet non-ferroelectric, mode. We use complementary experimental in-situ techniques to probe each order parameter individually, for the first time revealing the interplay between the two, in a nanoscale confined epitaxial thin-film system. Finally, in **Chapter 8**, we explore the emergence of an exotic polar state related to sub-unit-cell symmetry breaking in h-RMnO$_3$ thin films. We hence

3

demonstrate polar properties that are independent from the ferroic properties, yet may coexist with them, creating opportunities for novel functionality.

Finally, **Chapter 9** presents a concluding, overarching view of the results obtained in this thesis and discusses the general direction of future work.

Polar states in oxides for oxide thin-film technology

<div style="text-align: right; font-size: 3em; color: blue;">1</div>

1.1 Electronic polar states in oxides

In this work, we focus on different types of *electronic* polarity in crystalline oxides. Here, we will use the term *polar state* broadly, to refer to the specific arrangement of the electric dipoles (paired positive and negative charge) in a material. Our main focus is set on investigating polar states found in polar oxides, that is, in oxides where the alignment of local electric dipoles sums up to a net electric polarization, as schematized in Fig. 1.1(a). In addition, we will also use the term polar state to refer to cases where dipoles are ordered in a way that breaks inversion symmetry, but does not yield a net polarization, see (Fig. 1.1(b)). We note that while such noncentrosymmetric systems may not necessarily belong to a polar crystal class, in that they might not allow for a first-rank polar vector to be defined, they do exhibit characteristic higher-order *polar properties* that for instance can manifest as specific optical effects useful for photonic applications [39, 45] or that enable exotic electronic configurations in quantum materials [46, 47]. The relation between noncentrosymmetric and polar materials is seen in Fig. 1.1(c), where the material types are grouped by their crystallographic point-group symmetry. In the following, the properties of these subgroups are briefly described.

Piezoelectricity

20 out of the 21 noncentrosymmetric crystal classes are *piezoelectric*. This means that when mechanical stress is applied to the material, it polarizes, and conversely, applying an electric field to the material can induce strain. Because of this electro-mechanical coupling, piezoelectrics are extensively used as mechanical elements in technological applications, such as in sensors and actuators [48]. Materials belonging to the piezoelectric class also allow nonlinear optical effects such as second-harmonic generation and the linear electro-optic effect [38].
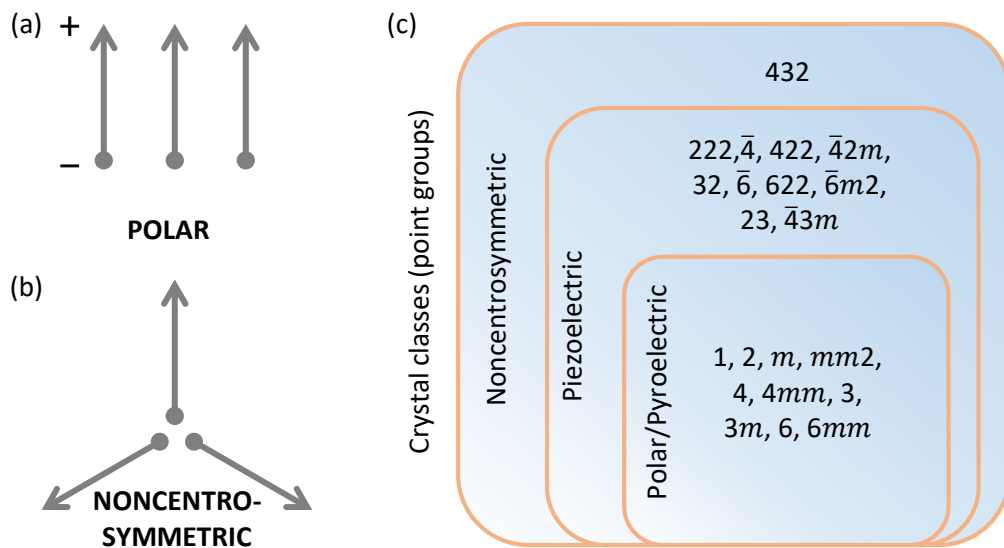
Figure 1.1: Schematics of (a) a polar and (b) a noncentrosymmetric (yet nonpolar) configuration of electric dipoles. (c) Diagram showing the classification of noncentrosymmetric crystal classes.

Pyroelectricity

A subset of the piezoelectric materials exhibit a permanently polarized structure and are, therefore, polar (Fig. 1.2(a-c)). Because the magnitude of the resulting *spontaneous polarization* is temperature dependent (Fig. 1.2(d)), these materials are termed *pyroelectric*: a change in temperature leads to a change in electric polarization, which leads to a transient electric current flowing through the material.

Ferroelectricity

A special case of pyroelectricity occurs in materials where the direction of the spontaneous polarization can be remanently reoriented between at least two degenerate polarization states by an applied electric field. Such materials are termed *ferroelectrics* [49]. The polarization states of a ferroelectric are separated by an energy barrier such that electric fields need to exceed a certain threshold to switch the polarization. This gives rise to a hysteretic behavior of the electric-field dependent polarization, see Fig. 1.2(e). The polarization in a ferroelectric need not be uniformly distributed across the entire specimen. There may exist *polarization domains*, inside which the material is in a single polarization state, but between which the polarization state can differ. Such domains are separated by domain walls where the polarization transitions from one state to the other. By applying electric fields locally in a ferroelectric material, specific domain and domain-wall configurations can be written or erased by design.
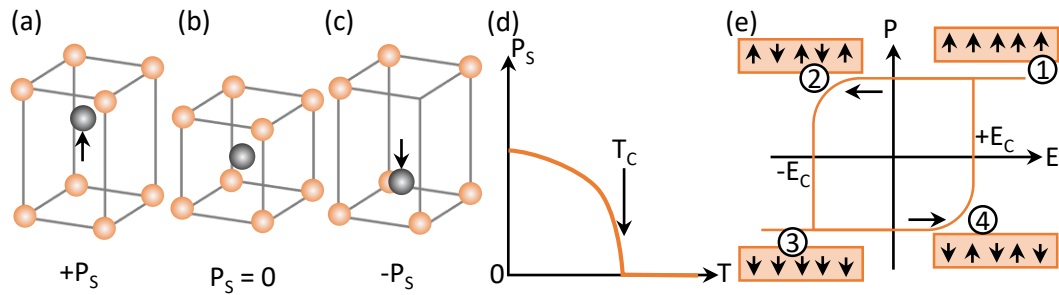
Figure 1.2: (a-c) Schematics of the displacement of charges in a unit cell leading to a polarization P_S. (d) Temperature dependence of polarization in a pyro- or ferroelectric material with onset at the critical temperature T_C. (e) Idealized schematic of the dependence of polarization on electric field in a ferroelectric. (1) A single domain state. (2) Applying an electric field oppositely oriented to the polarization at a coercive field strength E_C leads to reorientation of polarization by forming and/or expanding domains. (3) A single domain state with polarization along the electric-field direction is achieved above E_C. (4) Reversing the field reverses the polarization again. The remanence of polarization below E_C causes a hysteresis in the electric-field dependence.

Definition

Proper and improper ferroelectrics When a material undergoes a symmetry-lowering phase transition - for example from a centrosymmetric to a noncentrosymmetric phase - this transformation can be described by an *order parameter* that represents this symmetry loss [50]. For many ferroelectric materials, the change of crystal symmetry that occurs at the ferroelectric ordering temperature T_C, is completely defined by the symmetry of the polarization vector itself. Therefore, in all conventional ferroelectrics, the polarization vector is the leading order parameter of the phase transition. In contrast, there are certain ferroelectric materials where the polarization is an *improper* order parameter because it emerges as a byproduct of another order parameter, which has a lower symmetry than that of the polarization vector itself [50, 51]. In such *improper ferroelectrics*, the polarization state is fully defined by the non-ferroelectric primary order parameter. This primary order can be geometric, magnetic or stem from charge order. Because of the coupling to this primary order, improper ferroelectrics can be expected to behave differently in response to perturbations compared to the conventional ferroelectrics. In particular, improper ferroelectrics are susceptible to modification through their primary order parameter and can in some cases be less affected by their electrostatic boundary conditions than their proper counterparts.

The applications of ferroelectrics are many [42, 43, 52–54]. Due to the possibility to pole a ferroelectric, its piezoelectric response was shown to be especially

enhanced, establishing the technological relevance of ferroelectric ceramics for applications such as sensors and actuators. The high dielectric constant of ferroelectric oxides places them as prominent constituents in capacitors, whereas optical transparency and electro-optic effects make some ferroelectrics indispensable to telecommunication. More recently, thin-film technology has enabled their integration with microelectronics as ferroelectric memories, tunnel junctions and field-effect transistors [55–57]. With the discovery of enhanced conductivity at ferroelectric domain walls as a consequence of charge discontinuities at these nanoscale interfaces [58], a new field of research has emerged focusing on the functionality of such reconfigurable, conducting elements in the otherwise insulating ferroelectric matrix [59].

1.2   Polar properties in the ultrathin regime

In ultrathin oxide films, well below 100 nm in thickness, the emergence and evolution of polar states can differ greatly from that of bulk crystals. In extreme cases, the expected polar properties may be completely suppressed, or, conversely, novel polar phases may suddenly appear [60]. The modification of functional properties in the limit of ultrathin films are a consequence of the highly anisotropic dimensionality of the system: one out of three dimensions is strongly restricted to the nanoscale, yielding an extremely high surface-to-volume ratio. This has as effect that discontinuities in crystal structure and polarization at the thin-film surfaces may dominate the macroscopic behavior of the system. In fact, it can be almost impossible to distinguish the surface from the rest of the film [61]. Furthermore, charge accumulation at the closely spaced top and bottom surfaces can cause very high electric fields inside the ultrathin film, and thereby alter the stability of the polar state. Since most thin-films are not free-standing, but rather grown as a 'coating' on top of a substrate material, the electrostatic and mechanical properties of this substrate can significantly alter the level of distortion or polarization in the interfaced thin-film layer.

All this leads to modifications of polar states at the thin film level. These modifications can either be considered detrimental to the targeted functionality and need to be circumvented, or, alternatively, be mastered in order to be used to our advantage.

Size effects

In thin films, the energetically most favorable polarization state can differ significantly from the bulk-stable state. Size effects and electrical and mechanical boundary conditions at interfaces play dominating roles in setting the polar properties. For example, the bound charges at the interfaces of a polarized material lead to an electric field antiparallel to the polarization, a *depolarizing field*, see Fig. 1.3(a-c). For low film thickness and with a polarization direction perpendicular to the plane of
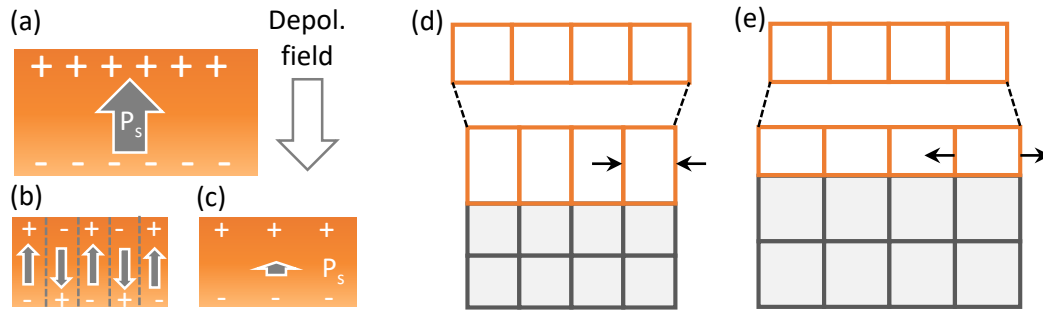
Figure 1.3: (a-c) Depolarizing-field effects in ferroelectrics. (a) Bound charges at the interfaces of a polarized material leads to a depolarizing field opposite to the polarization. To reduce this field inside the material, the ferroelectric can (b) form domains or (c) reduce its polarization. (d-e) The epitaxial relationship between substrate and film defines crystallographic phase, orientation and strain state. A lattice mismatch between film (orange) and substrate (gray), can impose for example (d) compressive or (e) tensile strain in the thin film, causing it to deform from its bulk-like structure.

the film, this depolarizing field can become large enough to trigger the formation of nanoscale domains [62], or suppress the spontaneous polarization entirely [63], in order to reduce the energy of the system.

The recent progress in oxide thin-film engineering has enabled seminal work on size effects in ultrathin films of conventional ferroelectrics. In epitaxial thin films, it was shown that the critical thickness needed to overcome the depolarizing field and stabilize a single domain polarization state can be reduced by providing free charges to the interfaces of the ferroelectric layer to electrically screen the polarization [64, 65], for instance by interfacing it with a metallic layer. In materials where the polarization can be oriented along both out-of-plane and in-plane directions in the films, unscreened interfaces may result in ferroelectric flux-closure or vortex domains in order to further minimize the electrostatic cost [66].

In the limit of ultrathin crystals, the long-range order can only be defined in the plane of the layer. The discontinuities in the crystal structure in the direction normal to the film, however, may exhibit a fundamentally different symmetry, and therefore different properties, than what is expected for the bulk crystal. In this 2D limit, a surface or interface may be polar even if the constituent materials are not [67].

Epitaxial constraints

Using state-of-the art oxide thin-film deposition techniques, it is possible to grow crystalline thin films with monolayer thickness precision [41]. When grown on a suitable, crystalline substrate, such a controlled growth allows the thin film to adapt to the crystal structure of the substrate, forming an *epitaxial* thin film (Fig. 1.3(d,e)) [68]. Such epitaxial growth can be used to favor a certain crystal structure or orientation of the thin film material [69]. Additionally, if there is mismatch in lattice

parameters between substrate an film, it is possible to strain the thin film by up to a few percent compared to its bulk lattice – levels that would cause cracking in bulk crystals but can be sustained in ultrathin films. Beyond epitaxial strain, the mechanical stiffness and possible lattice distortion of the substrate also plays a defining role for the propagation of lattice distortions in the thin film layer. By imposing such mechanical boundary conditions [70], completely new phases may even be stabilized in ultrathin epitaxial films that are otherwise unstable in bulk [71]. Often, these films exhibit symmetries that are different from the bulk-stable crystalline order. Due to the intimate relationship between symmetry and property, the stabilization of such metastable phases allows, for example, the realization of novel polar functionalities that are inaccessible in bulk [60].

The epitaxial control of crystalline order is essential for the stabilization and systematic investigation of polar properties in oxide thin films [72]. For many ferroelectric materials, the ferroelectric polarization is directly linked to a lattice distortion and therefore highly susceptible to strain [73]. In some cases, epitaxial-stress-induced lattice distortion is known to significantly increase both the polarization value and T_C [74].

1.3 Challenges in characterizing polar states in thin films

The detailed characterization of polar properties in ultrathin films is often hampered by their limited sampling volume and small domain sizes[1]. Since polar materials respond uniquely to applied electric fields, electrical measurements have been the method of choice for characterizing their functionality. However, in ultrathin films, the application of an electric field can easily cause a current to run through the thin layer and, as a result of the following thermal degradation, hinder electrical characterization below a certain thickness. In more complex thin-film systems, consisting of several thin-film materials grown on top of each other, the polar material of interest may be buried inside the heterostructure. Conventional characterization techniques relying on electrical contact fail also in this case. A very successful method to probe crystalline polar materials is to directly map the distortions of the lattice at the atomic scale by transmission electron microscopy. However, to guarantee transmission of enough electrons, this requires cutting out a very small part of the thin film, thus destroying most of the sample in the process.

Furthermore, the polar state of many thin-film oxides is set directly during the synthesis of the material [75]. As such, it is difficult to fully understand the mechanisms of polar state formation by post-deposition characterization alone. To extend the understanding and utilization of ultrathin functional polar oxides, it is important to

---

[1]According to the Kittel law, the width, w, of ferroelectric domains tend to scale as the square root of the film thickness t: $w \propto t^{1/2}$ [56]

be able to probe and distinguish the behavior of multiple, potentially coupled, polar states in thin films in the very environment where they are formed and controlled.

For this purpose, the distinct nonlinear-optical properties of noncentrosymmetric materials come in useful. When irradiating a noncentrosymmetric material with intense light, such as from a laser, the material can emit light at both the incoming light frequency and the doubled frequency [76, 77]. The frequency doubling of light is termed *optical second harmonic generation*, and its light-polarization dependence is given by the specific symmetry of the noncentrosymmetric material. Therefore, analyzing the second harmonic generation light emitted from a thin film yields information on its polar properties [44]. Using this optical approach, no destructive sample preparation is needed and there is also no need for electrical contacts. In this work we exploit these two characteristics of second harmonic generation to implement an optical probe that can access polar properties directly in the thin-film growth environment [78] yielding unprecedented insight on the emergence of polarity in the instant the material is synthesized.

1.4   Materials

While the family of transition metal oxides is vast, and can crystallize in multifarious noncentrosymmetric or even polar phases, this thesis investigates three specific systems that together represent this polar diversity. We select a set of thin-film systems whose prominent polar behavior in the ultrathin regime suggests great technological prospects, yet where the mechanisms guiding the formation and manifestation of these properties remain underexplored. The materials in question, namely $BaTiO_3$, $BiFeO_3$ and the family of hexagonal manganites, span prototypical perovskites and layered materials, exhibiting proper or improper ferroelectricity and emergent phenomena such as metastable polar states. Each of these material systems are briefly introduced below.

1.4.1 $BaTiO_3$

The first perovskite ferroelectric material to be discovered was tetragonal $BaTiO_3$. It is a displacive ferroelectric where the polarization transforms the centrosymmetric cubic phase into a tetragonal phase via an off-centering of the Ti atom (Fig. 1.4(a)). The displacement of the Ti atom leads to a polarization of 26 μC/cm^2 along the tetragonal c-axis. In bulk crystals, the ferroelectric transition temperature is 393 K [79, 80]. Because of the possibility of two polarization directions along each principal axis, ferroelectric $BaTiO_3$ has six degenerate polarization states. The ferroelectricity is accompanied by an improper spontaneous strain which manifests itself as an elongation of the c-axis at a ratio of approximately 1.01 to the tetragonal a-axes. This spontaneous strain can be rotated or switched by applying stress to the system,
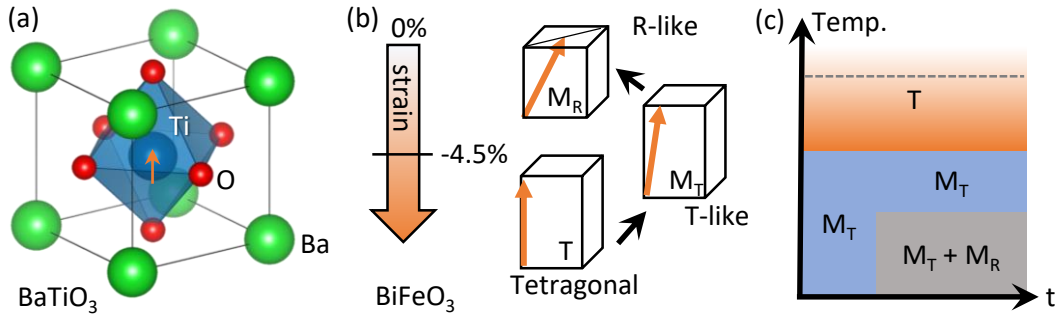
Figure 1.4: (a) $BaTiO_3$ crystal structure. (b,c) Metastable monoclinic polar phases at the strain-driven morphotropic phase boundary in $BiFeO_3$. (b) The highly strained tetragonal (T) phase relaxes by forming monoclinic distortions that result in tetragonal-like (T-like) and rhombohedral-like (R-like) phases. The orange arrows indicate the direction of the polar axis in both (a) and (b). The temperature-thickness phase diagram is schematized in (c) [81–83]. The thin-film epitaxial growth is in the temperature range of the tetragonal phase, indicated by the dashed line.

making $BaTiO_3$ ferroelastic in addition to ferroelectric. There are three degenerate ferroelastic states in the system, one along each principal crystallographic axis.

The nanotechnological relevance of $BaTiO_3$ was emphasized in the seminal work demonstrating that epitaxial strain could increase the transition temperature in $BaTiO_3$ thin films by more than $500\,K$ and enhance the polarization value several times over [74]. Ferroelectric $BaTiO_3$ also possesses one of the highest linear electro-optic coefficients of oxide materials, both in bulk and thin films [29]. This means that aside from piezoelectric and ferroelectric functionality for oxide electronics, $BaTiO_3$ thin films are also envisioned as a prominent building block for novel photonic integrated circuits. Indeed, the recent success in integrating high-quality epitaxial $BaTiO_3$ films with standardized silicon-based electronics [84] has triggered the vision of a hybrid technology platform combining the polar functionality of oxides with the electronic functionality of semiconductors. Yet, it remains unclear how the complex multidomain state with coexisting polar orientations behaves during the operation of such an electro-optic device.

1.4.2 $BiFeO_3$

Some ferroelectric oxides allow the coveted coexistence and coupling between electric polarization and magnetic order, making them multiferroic and/or magnetoelectric. One of the most promising technologically relevant multiferroics is $BiFeO_3$[85]. It is known as one of the few room-temperature multiferroics, where in the case of $BiFeO_3$, the ferroelectric order coexists with antiferromagnetic order. Below its ferroelectric transition temperature of $\sim 1100\,K$, $BiFeO_3$ has a rhombohedral bulk crystal symmetry with a spontaneous polarization of $60\,\mu C/cm^2$ along one of the pseudocubic $\langle 111 \rangle$ directions [86]. The spontaneous polarization arises from the

alignment of lone-pair electrons at the Bi ion. At $\sim 640\,$K the material becomes antiferromagnetic due to ordering of the Fe spins. Because of the coupling between these ferroic orders [87], and the subsequent proof of magnetoelectric switching in BiFeO$_3$ thin films [88], this material has been intensely investigated in thin-film form for the prospective implementation in magnetoelectric and spintronic devices.

Recently, it was also found that by applying large compressive stress to BiFeO$_3$ thin films, a phase transition to a tetragonal- (T-) like monoclinic phase is triggered [89], exhibiting a giant spontaneous polarization along [001] reaching up to 150 μC/cm^2 [90]. This T-like phase is very close in energy to the R-like monoclinic phase and at -4.5% strain, the system sits on a strain-driven morphotropic phase boundary [89], where T-like, R-like and a set of intermediate transition phases can coexist (see Fig. 1.4(b,c)). Because of the closeness in energy between these phases, small shifts in total energy, such as by a change in temperature or strain-state, or under application of mechanical pressure or electric field, can lead to reversible phase transformations and, hence, exceptionally large mechanical and electrical response [91]. Such giant piezoelectric response is also found at the composition-driven morphotropic phase boundary in one of the most widely used piezoelectric systems: antiferroelectric-ferroelectric PbZr$_{1-x}$Ti$_x$O$_3$ (PZT). The combination of magnetoelectricity and a strong polarizaton in absence of strain, and large electro-mechanical response at the strain-driven morphotropic phase boundary, sets BiFeO$_3$ apart as one of the most versatile room-temperature ferroic oxides currently known. Yet, despite the technological prospects of this material, surprisingly little is known about the emergence of polarization at the morphotropic phase boundary in ultrathin films.

1.4.3 Hexagonal manganites

The hexagonal manganites, h-RMnO$_3$ (R = Sc, Y, In, Dy-Lu), constitute a class of materials that exhibits a geometrically driven type of improper ferroelectricity [92]. This means that the improper spontaneous polarization, $\mathbf{P}_\mathrm{S}$, is driven by its coupling to a primary-order geometric distortion of the lattice related to ionic size effects. In the hexagonal manganites, the improper ferroelectricity sets in around 1250 to 1650 K [93, 94]. Its primary-order distortion consists of a coordinated tilt and rotation of the MnO$_5$ bipyramids around a central R^{3+} ion, leading in addition to a corrugation of the R-ion planes along the c axis. This distortion results in a tripling of the unit cell and is therefore referred to as a lattice *trimerization* (Fig. 1.5(a-c)).

Because of the triangular symmetry of the lattice ab planes, there exists a three-fold choice of central R^{3+} ion site. As additional degree of freedom, the MnO$_5$ bipyramids can tilt towards of away from this trimerization center. This leads to a total of 3 $\times$ 2 = 6 possible trimerization domain states in h-RMnO$_3$. The order parameter describing this trimerization is denoted $\mathbf{Q}$ and is a two-component order
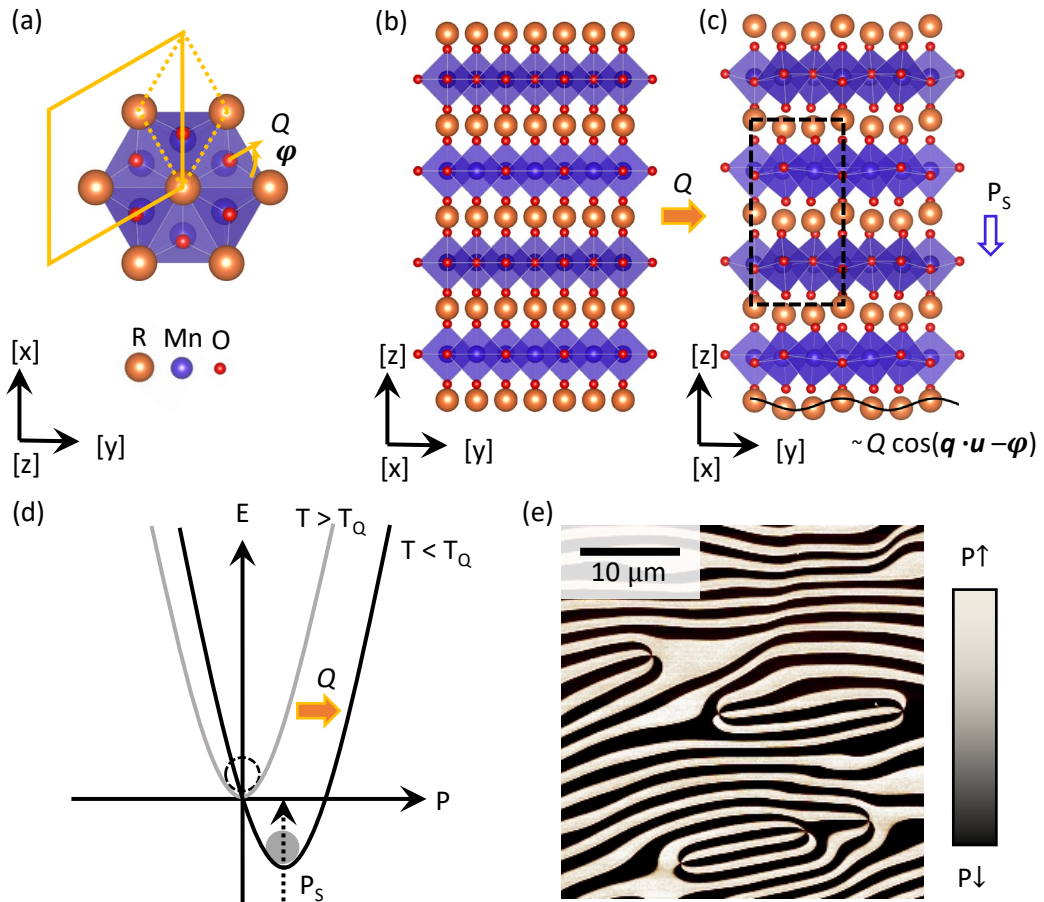
13

Figure 1.5: (a-c) Hexagonal RMnO$_3$ crystal structure in the nonpolar ($\mathbf{Q} = 0$) and the polar ($\mathbf{Q} \neq 0$) phase. (a) Top view (along hexagonal c-axis) of the nonpolar structure. The yellow arrows define the parametrization of the structural distortion $\mathbf{Q}$ with amplitude Q and phase φ. The dotted yellow box indicates the unit cell in the nonpolar phase and the solid yellow box indicates the unit-cell tripling brought on by the trimerization. Note also the resulting 30° rotation of the hexagonal in-plane axes. (b,c) Side view of (b) the nonpolar and (c) the polar structure. The trimerization is manifested as a tilt and rotation of Mn-O bipyramids together with an corrugation of the R-ion planes seen as an 'up-up-down'displacement along the present view. The dashed black box indicates the unit cell. Note that due to the layered structure of the material, each unit cell consists of two R and two Mn-O planes each. (d) Energy diagram for the improper spontaneous polarization. (e) Piezo-response force microscopy on a c-cut hexagonal YMnO$_3$ crystal, revealing the vortex domain pattern in the polarization [Data from this work].

parameter with tilt amplitude Q and angle φ, Fig. 1.5(a). Equivalently, $\mathbf{Q}$ describes the sinusoidal corrugation of R ions along the c axis with amplitude Q and phase φ [95], see Fig. 1.5(c).

The trimerization breaks the inversion symmetry of the system but does not by itself carry a polarization. Yet, it can be thought of as a geometric field that couples to the polar instability and pushes it towards a finite polarization (see Fig. 1.5(d)). The improper polarization reaches a value of about $5\,\mu C/cm^2$ in the hexagonal manganites [93]. It appears along the c-axis, making these compounds uniaxial ferroelectrics, and consequently they have two polarization domain states. The direction of the improper spontaneous polarization is unambiguously set by the value of $\mathbf{Q}$, where the P^- or P^+ are given by a trimerization tilt either towards or away from the trimerization center, respectively. In contrast, the polarization state is independent of the choice central R^{3+} ion. This is a characteristic property of an improper ferroelectric [51]: there exist polarization domains that have the same polarization direction, yet they are not equivalent, because they belong to different states of the primary order parameter, in this case $\mathbf{Q}$.

Through its coupling to the trimerization, the improper polarization can persist in configurations that are energetically unfavorable and are therefore avoided in a conventional ferroelectric system. In particular, the ferroelectric domain structure is set by the trimerization when the polarization is vanishingly small, due to the coupling term $\mathbf{P}_S \sim \mathbf{Q}^3$ for $Q \ll 1$ at the transition temperature [96], meaning that no electrostatic effects, such as depolarizing-field effects, acting mainly on $\mathbf{P}_S$, can influence the resulting domain pattern, neither can they suppress the phase transition. Instead, it is the topological nature of the trimerization order parameter that dictates the domain formation and leads to an exotic six-fold vortex domain pattern [97, 98] (Fig. 1.5(e)). This domain pattern is common to both order parameters, and thus, the polarization domains can possess meandering domain walls irrespective of the high electrostatic cost of their curvature and frequent head-to-head and tail-to-tail polarization configurations, causing polarization discontinuities. Such domain walls in the hexagonal manganites have been shown to have enhanced electronic conductivity that can be tuned by the application of an electric field [99, 100].

In addition to this unconventional type of ferroelectricity, the hexagonal manganites become multiferroic at temperatures below 130 K, with the onset of anti-ferromagnetic order in the Mn sublattice [101, 102]. In conventional ferroelectrics, coexistance of polarization with magnetic order is contraindicated [103]. Here, however, the improper nature of $\mathbf{P}_S$ allows circumventing such exclusive conditions. In the hexagonal manganites, a coupling between the domain structures of two orders is even seen [104].

Because of these features, the hexagonal manganites host unusual physical properties and exotic functionality. This, in combination with the expectation of a particular robustness of the polarization against unfavorable electrostatic boundary

conditions [105], puts the hexagonal manganites as prominent candidates for supplying novel functionality to oxide electronics. However, studies on the manifestation of improper polarization in thin-film systems, especially in the ultrathin regime, remain scarce.

Thin-film growth and characterization

2

To study the functional properties of oxide thin films, a method to synthesize high-quality films with a defined crystal structure and orientation is essential. For studies of films in the ultrathin regime (< 50 nm), precise thickness control is also necessary.

All oxide thin films that are part of this work were grown by pulsed laser deposition (PLD). Metal thin films were deposited by sputtering. In order to iteratively optimize the thin film quality in all cases, a combination of in-situ reflection high-energy electron diffraction (RHEED), post-deposition x-ray diffraction (XRD) and scanning probe microscopy (SPM) was used for obtaining feedback on the crystallographic structure. Finally, atomic-scale imaging on selected samples was acquired using scanning transmission electron microscopy (STEM), which was performed by Marta Rossell and Marco Campanini at the Electron Microscopy Center at Empa, Switzerland. In the following, a brief background on the fundamentals of each technique is presented.

2.1 Deposition techniques

Epitaxy denotes the growth of one crystalline material (thin film) on top of another (substrate), such that the crystalline orientation of the top layer is well-defined with respect to that of the substrate [41, 68]. To achieve such epitaxial growth of thin films, we need first of all to identify a crystalline substrate whose atomic arrangement of the surface provides a template whose lattice matches that of the desired crystalline phase and orientation of the thin-film material. Second, we need an ultraclean, controlled atmosphere during the deposition, to prevent incorporation of impurities. This is achieved by maintaining a high vacuum ($< 10^{-6}$ mbar) in the growth chamber before deposition, and introducing the only desired background gas and material species into the vacuum chamber during deposition. Finally, we need to supply enough energy to the thin-film material to allow movement of the randomly deposited atoms on the sample surface in order for them to arrange themselves into a precisely ordered structure. For the PLD and sputtering techniques described below, this energy is typically supplied by heating the substrate in both cases, while the methods of supplying the materials species to the substrate in the first place differ.
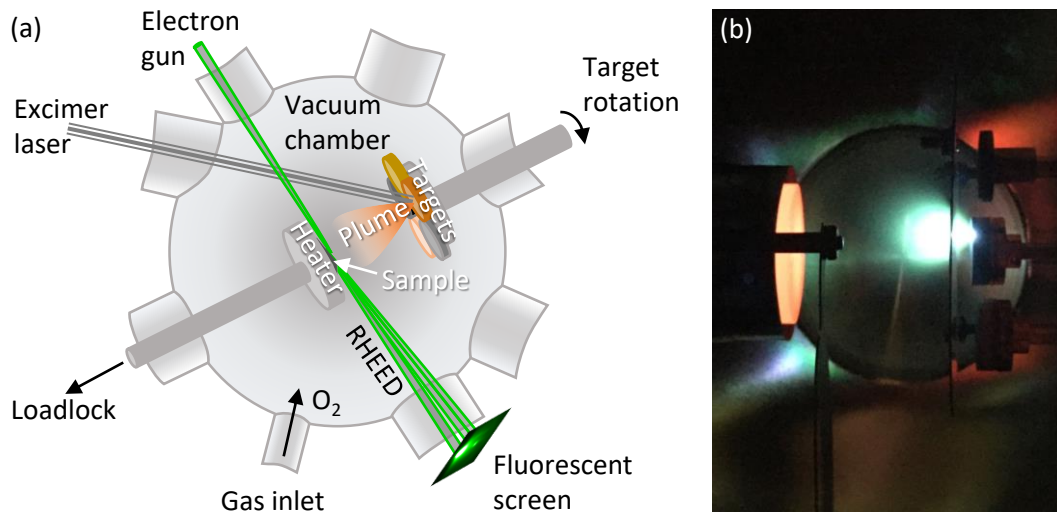
Figure 2.1: (a) Schematic of the PLD vacuum chamber. The substrate is mounted on a heater stage for deposition at elevated temperature. At a distance of a few centimeters a set of stoichiometric ceramic or single crystal targets are mounted on a rotating stage. The target rotation enables laser ablation from a bigger area of the target as well as changing materials during growth of multilayers. For controlled chemical composition of the films, the chamber is pumped to ultra-high vacuum ($\sim 10^{-7}$ mbar) before deposition to ensure a clean environment. (b) Photograph of thin-film deposition from an $ErMnO_3$ ceramic. The greenish plume created by the excimer laser transports the material towards the substrate, which is heated to 750 °C.

Pulsed laser deposition

PLD is a particularly convenient tool for depositing epitaxial oxide thin films [106]. It is a physical vapor deposition technique where the target material is ablated from a crystal or ceramic pellet by high-energy fluence UV laser pulses to create a plasma of the material species, which subsequently is transferred to a crystalline substrate (see schematic in Fig. 2.1). PLD in an oxygen atmosphere is used for ensuring oxidation of the materials species. In this work, we use laser pulses generated from a KrF excimer laser with $\lambda = 248$ nm and a pulse length of 20 ns. The targets can be bulk crystals or ceramic pellets with the desired material stoichiometry. To favor epitaxial growth over amorphous deposition, the substrate is usually kept at an elevated temperature in the range of 400-900 °C. Furthermore, to ensure a single crystalline orientation of the film and to minimize defect formation, the deposition rate is often kept low with respect to the mobility of deposited species on the sample surface. For this work, typical growth rates lie in the interval 0.1-5 nm per minute. The choice of substrate (type of crystal and orientation), as well as temperature, background oxygen pressure and laser fluence and repetition rate, are all control parameters that define the thin-film growth mode, structure and quality.

The evolution of structural and functional properties of the thin films during the growth process itself can be monitored by certain in-situ characterization tools. How-
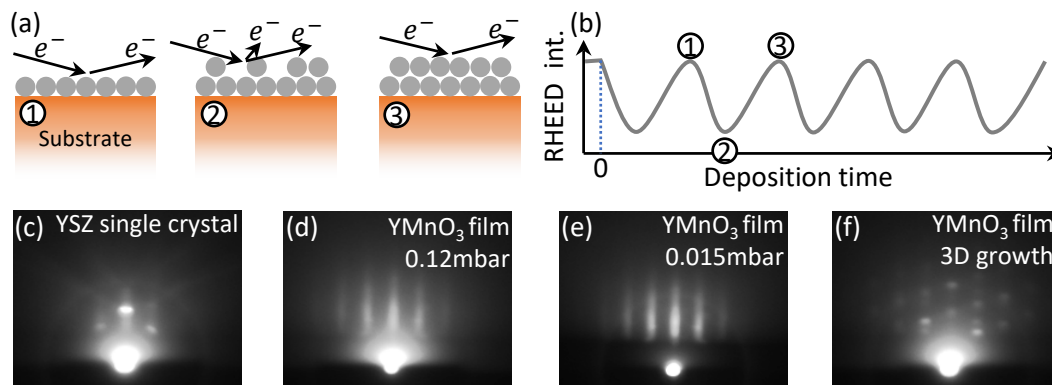
Figure 2.2: (a,b) Origin of RHEED intensity oscillations during layer-by-layer growth. (1) One complete monolayer has been deposited, a maximum in reflected electron intensity is observed. (2) As deposition of the material continues, islands nucleate on the surface, causing scattering of electrons and only a reduced fraction of the electrons contribute to the detected diffraction pattern: the RHEED intensity drops. As the islands begin to merge when more material is deposited, the roughness of the uppermost layer is reduced. (3) When the monolayer has been completed, the detected RHEED intensity recovers its maximum value.(c-f) RHEED diffraction patterns for different surfaces. (c) Single crystal substrate. Diffraction pattern shows discrete spots from a perfect 2D lattice. Kikuchi lines originating from diffuse scattering are discernible along the diagonals. (d) Low-rougness thin-film surface. Due to the film having randomly oriented surface steps and terraces, streaking of the diffraction pattern is observed. (e) The same film as in (d) in lower oxygen partial pressure. The diffuse scattering is significantly diminished. (f) Diffraction pattern during 3D growth. The electrons are transmitted through small islands of thin film material, and diffract on the bulk lattice to form a 3D diffraction pattern.

ever, due to the harsh environment in the growth chamber, real-time characterization of the deposited film remains challenging. For this thesis, high-pressure RHEED was used to follow the growth mode and thickness evolution [107]. The principle of RHEED is described briefly in the next section. In addition to this structural analysis, a unique in-situ optical second harmonic generation (ISHG) technique was developed in our lab for the specific purpose of monitoring the emergence of functional polar properties during thin film growth. The ISHG tool was co-developed and optimized as part of this thesis, and is presented in Chapter 3.

In-situ reflection high-energy electron diffraction

Electron diffraction on the surface of thin-film samples yields information on their surface properties [107, 108]. The diffraction pattern reveals the crystal orientation and strain state and the reflected intensity can be used for real-time monitoring of surface roughness.

The grazing-incidence geometry of RHEED renders the intensity of both reflected and diffracted electrons very sensitive to surface roughness. Therefore, the intensity of the specular RHEED reflection enables real-time monitoring of the growth mode.

19

For a 2D growth mode, the nucleation of islands on the surface will increase its roughness. Due to the scattering of electrons on step edges, the total RHEED intensity decreases with increasing edge density until the resulting islands start to merge and complete the layer. At that point, the edge density decreases again, and the reflected RHEED intensity is maximized by the completion of the layer. Hence, each time the RHEED intensity reaches a maximum, a full monolayer has been deposited, and the film thickness and growth rate can be inferred by the oscillation period (see schematic in Fig. 2.2). In a perfect crystal, the RHEED results in a 2D diffraction pattern with sharp reflections in addition to so-called Kikuchi lines stemming from diffusely scattered electrons that subsequently diffract on the lattice under different incidence than the original beam. For a thin-film surface with random orientation of surface steps and terraces, the 2D diffraction spots broaden and streaking is observed in the diffraction pattern [108]. In case of a 3D growth mode, nucleation of new islands occur before the completion of the previous layer and the surface roughness is constantly high. This manifests as a different type of RHEED pattern, since the electrons are diffracted not only on the 2D lattice of the surface, but also in transmission through the 3D bulk lattice of the islands. However, for thin-film deposition under high oxygen background pressure, as is typical for PLD, a considerable amount of diffuse scattering on the oxygen gas molecules washes out the RHEED contrast. While differential pumping at the electron gun greatly reduces the path traveled in oxygen atmosphere for the electrons, enabling in-situ RHEED also at high pressure [107], the detailed analysis of the diffraction pattern remains challenging. Hence, for the work presented here, RHEED monitoring is used mainly for following the growth mode and deposition rate through the intensity oscillations of the specular reflection.

Sputtering

An important part of the investigation of ferroelectric materials is their response to external and internal electric fields, as explained in the introduction. Therefore, the insertion of highly conducting materials, to serve as electrode or charge-screening layer next to the ferroelectric thin films is necessary.

While it is possible to deposit metal films by PLD, their different absorption, thermal conductivity and binding energy compared to oxides with a band gap results in the need of roughly one order of magnitue higher energy fluences to create a plasma, which imposes a practical challenge. On the other hand, to be able to deposit the electrodes in the same process as the oxide thin film has the advantage of cleaner interfaces between the two materials, since the sample does not need to be transferred between different deposition chambers. For this reason, conducting oxides such as indium tin oxide (ITO) can be used instead of elemental metals. When elemental metal films such as platinum were required, another physical
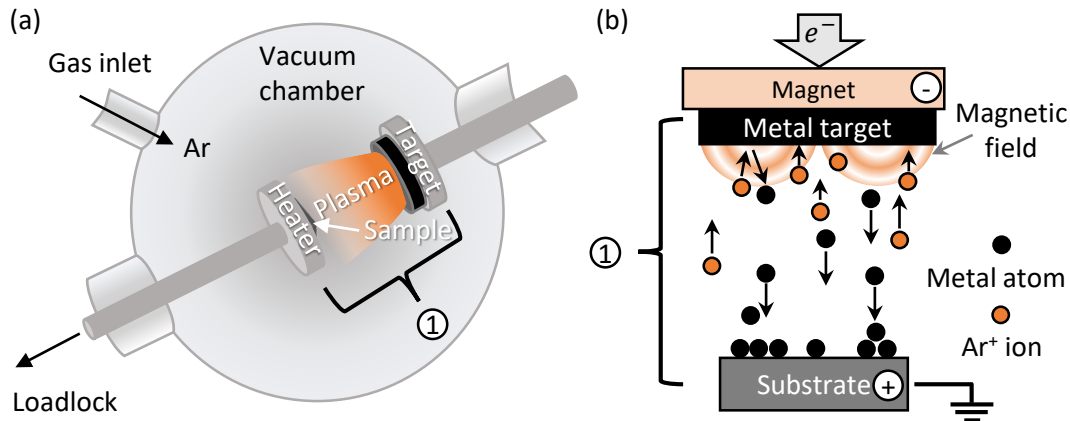
Figure 2.3: DC magnetron sputtering of metal thin films. (a) Schematic of the sputtering chamber. (b) The principle of DC magnetron sputtering.

vapor deposition technique was employed, namely, direct-current (DC) magnetron sputtering. In our case, the sputter chamber is in direct contact with the PLD chamber, and thus heterostructures involving films from both chambers can be synthesized without breaking vacuum.

In DC magnetron sputtering [109], the metallic source material is sputtered off the target by ionized species of the argon gas atmosphere (here at a typical partial pressure of $5 \cdot 10^{-2}$ mbar) being bombarded into the target material. These metal atoms travel towards, and subsequently condense upon, the substrate. This process is sketched in Fig. 2.3. To make the process more efficient (higher deposition rate), strong magnets are incorporated with the target holder, whose magnetic field contains the electrons close to the target surface, which increases the rate of sputter-gas ionization. In order to achieve epitaxial metal films, the substrate is heated to enable crystallization. Here, the deposition rate was calibrated by post-deposition x-ray reflectivity measurements of the resulting film thickness for different deposition conditions.

2.2 Structural characterization

X-ray diffraction

Because the wavelength of x-rays is on the same length scale as the distances between atoms in materials, they interact strongly, where for crystalline materials, the x-rays diffract on the crystallographic planes [110]. See Fig. 2.4.

The condition for constructive interference of diffracted coherent x-rays, leading to intense so-called Bragg peaks in x-ray intensity, is given by the Bragg condition:

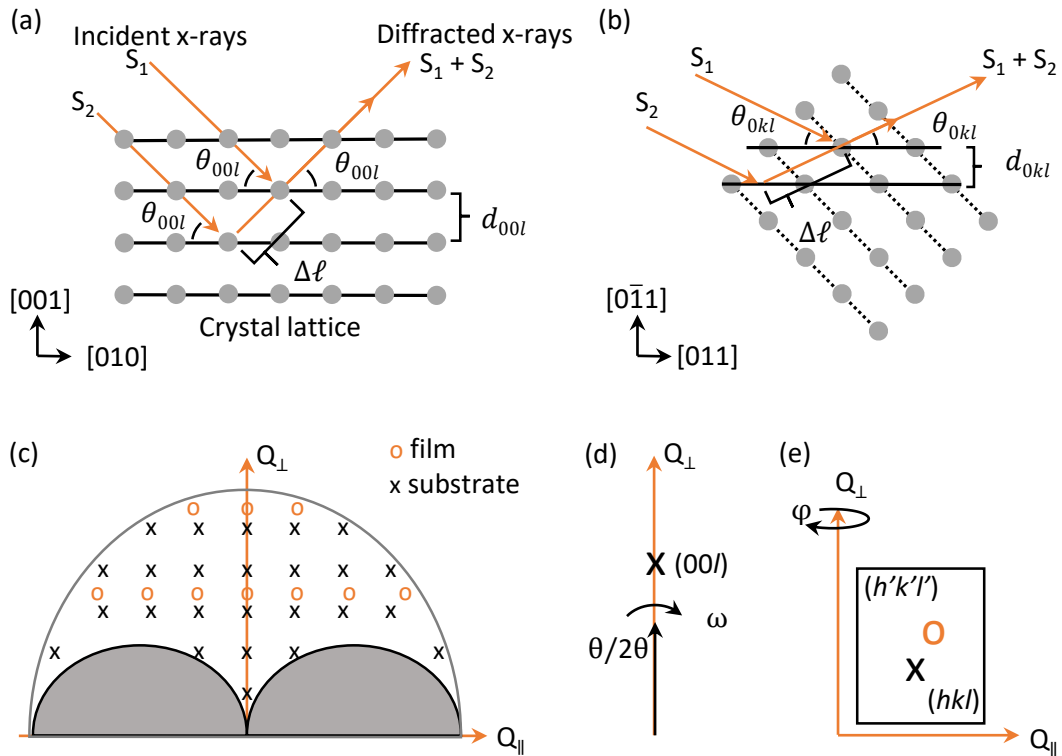$$2d \sin \theta = n\lambda; \; n = 1, 2, 3...,$$ (2.1)

21

Figure 2.4: Principle of x-ray diffraction. Bragg condition leads to constructive interference for certain incident and diffracted angles when diffracting on crystallographic planes. At these angles, intense peaks in the detected x-ray intensity appears. (a) Bragg reflection on the ($00l$) planes yields the out-of-plane lattice parameter. (b) Tilting the sample enables diffraction on off-axis planes, from which in-plane lattice parameters can be extracted. (c) The reciprocal space accessible by the diffractometer. The outer sphere is the limit set by the x-ray wavelength and the inner spheres are limits set by the measurement geometry. (d) A line scan with $Q_{||} = 0$ is denoted $\theta/2\theta$. A scan of the sample tilt (by angle ω) around a diffraction peak in $\theta/2\theta$ is denoted an omega scan or rocking curve. (e) Reciprocal space mapping (RSM) yields a 2D map of a part of the reciprocal space of the sample. For thin-film systems this is particularly useful for comparing the film orientation and lattice parameters with respect to the substrate lattice. By rotating the sample around its z axis (by angle φ), at a certain off-axis diffraction peak, the in-plane orientation and potential crystal twinning can be detected in a so-called phi scan.

where d is the spacing between the lattice planes, θ is the angle of incidence and diffraction and λ is the wavelength of the x-rays. Essentially, this means that the difference in travelled path length, Δl, between x-rays diffracting on equivalent crystallographic planes needs to correspond to an integer n multiple of the wavelength to obtain constructive interference.

The scattering angles θ at which diffraction peaks occur, with respect to the sample orientation, defines a specific diffraction pattern in reciprocal space (Fig. 2.4(c)). Each reflection in reciprocal space can be indexed by its Q vector, which is related to the distance d between crystallogrphic planes in real space as $Q = 2\pi/d$.

For the work presented here, a PanAnalytical X'Pert[3] MRD four-circle diffractometer was used for XRD analysis of the thin film samples. It uses monochromatic CuK$_\alpha$ radiation at λ = 1.5418 Å. This diffractometer dedicated for thin-film analysis supports both high-resolution line scans and 2D reciprocal space mapping (RSM), as sketched in Fig. 2.4(c,d). XRD yields information about the lattice parameters of the film and the substrate, their potential lattice mismatch, and the resulting strain state [110]. The crystallographic orientation can also be determined as well as the texture and twinning of the film. For thin layers, the effect of a finite number of atomic planes contributing to the diffraction results in (i) a broadening of the peaks (for an infinite crystal the diffraction peaks become delta functions) and (ii) so-called Laue oscillations around the diffraction peak. The period of the Laue oscillations depends on the number of atomic planes contributing the diffraction peak, and is therefore related to the film thickness. Such thickness oscillations can only be seen if the film interfaces are smooth with little or no misoriented grains and thickness variation. The presence of Laue oscillations in the diffraction patterns of thin films is therefore a good indicator for high-quality epitaxy.

In grazing incidence geometry ($\theta < 10°$), the x-rays reflect from interfaces between layers with different density. This is in contrast to diffraction that is sensitive to the atomic planes within each layer. Since the total-reflection conditions depend on the layer thicknesses, Kiessig fringes appear in the reflected beam intensity as function of the incident angle. From the periodicity and attenuation of these fringes in x-ray reflectivity (XRR) measurements, the film thickness and interface roughness can be estimated for both single layers and, with appropriate fitting models, also multilayers.

Scanning probe microscopy

Atomic-force microscopy (AFM) and piezo-response force microscopy (PFM) were used for spatially resolving and characterizing the surface properties of the thin films [111]. Their working principle is sketched in Fig. 2.5. A sharp tip with an apex of about 20 nm is attached to a cantilever and scanned across the sample in close proximity to the sample surface. Hence, both AFM and PFM are scanning probe microscopy techniques and which usually represent distinct operating modes of the same microscope. The position of the tip with respect to the sample surface is minutely controlled by applying a voltage to piezostages that extend or contract the stage in the x, y and z directions.

The AFM mode is used for measuring the surface topography. The tip is placed in such close proximity with the sample surface, that the atomic forces it experiences depend very strongly on the tip–sample distance. Hence, a small protrusion or step on the surface can lead to large deflection of the cantilever, either away or towards the sample surface. Thus, a vertical resolution of about 0.1 nm can be achieved. A
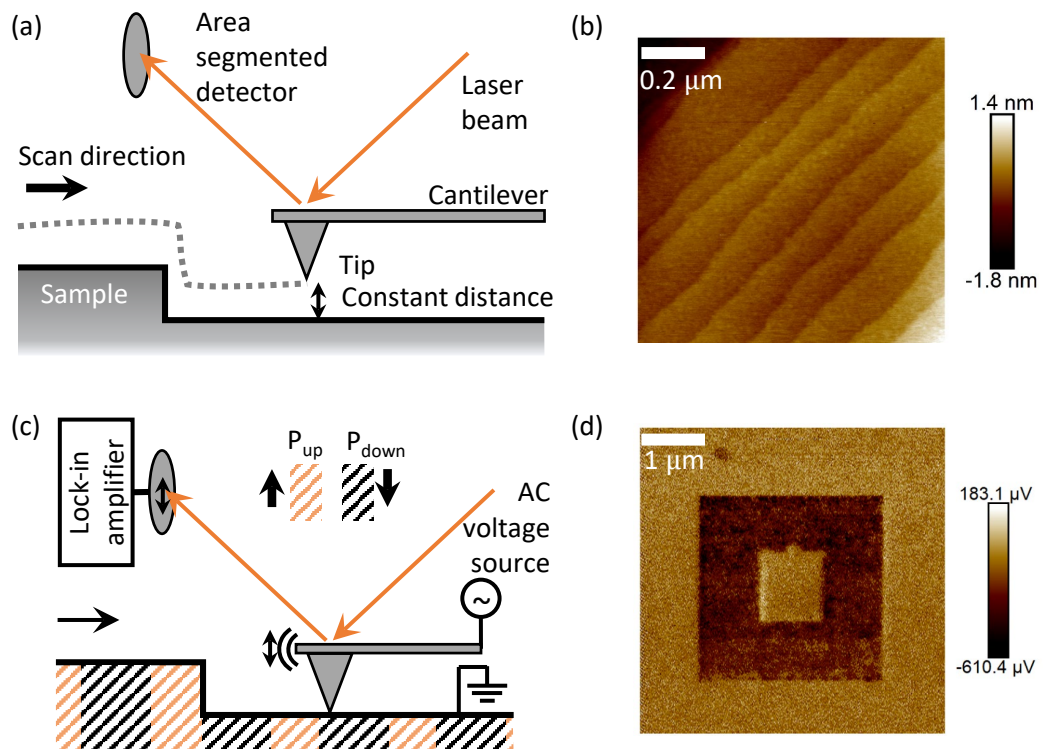
Figure 2.5: Scanning-probe analysis of thin-film surface properties. (a) Schematic of AFM in non-contact mode. (c) AFM topography image of atomic step terraces on the surface of a typical substrate. Here with a step height of approx. 300 pm. (b) Schematic of PFM in contact mode. (d) Out-of-plane PFM signal from an area of a PZT thin film where the as-grown up-polarized (bright) state has been switched to down-polarized (dark) in the outer square and back to up-polarized in the inner square by a PFM tip with an applied DC voltage in a sequence of preceding scans.

laser beam is reflected on the top of the cantilever and its position is recorded by a segmented detector. Thus, any deflection of the cantilever will lead to a deflection of the laser beam on the detector. In a typical non-contact AFM mode, the sample-tip distance is kept constant by minimizing deflections through a feedback loop. The correction movements of the vertical sample position can then be translated to the surface topography.

In PFM, the surface topography is recorded as in AFM, with the additional restriction that a conducting tip is used and that the tip is in contact with the sample. Aside from the mechanical deflection caused by changes in topography, an AC voltage is applied between the conducting tip and the sample holder, i.e., an AC electric field is created across the thin film if it is insulating. If the thin-film material is ferroelectric, it is also piezoelectric, and this AC electric field will cause sample surface oscillations through the inverse piezoelectric effect. This results in a deflection of the PFM tip that occurs at the same frequency as the applied AC voltage, yet with a shifted phase that depends on the sign of the piezoelectric coefficients. The
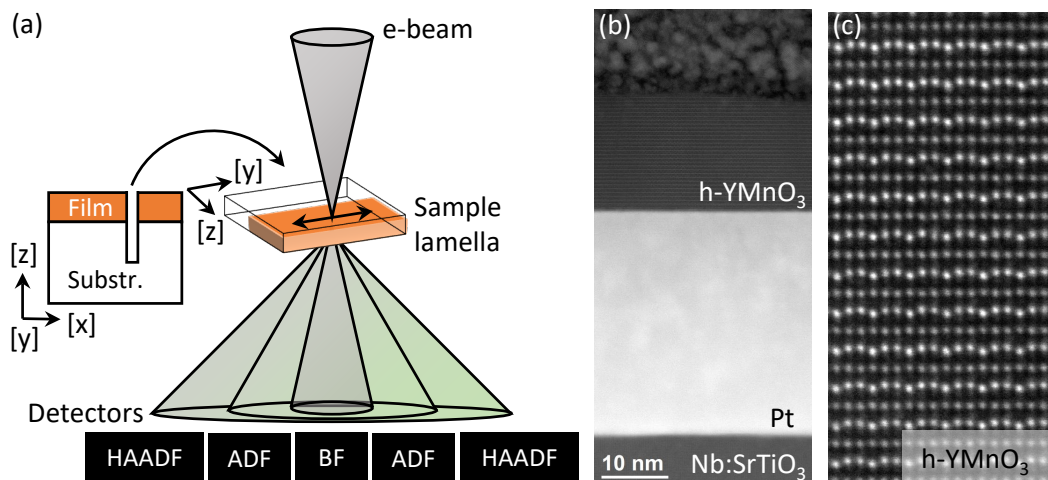
Figure 2.6: Scanning transmission electron microscopy (STEM). (a) A tightly convergent electron beam is scanned over a very thin lamella of the sample. The transmitted beam is detected by the bright-field (BF) detector. Annular dark-field (ADF) and high angle annular dark-field (HAADF) detectors record incoherently scattered electrons, where the intensity depends in an approximately quadratic way on the atomic number Z. (b) Low-magnification HAADF image of an $YMnO_3$ layer on a Pt-buffered $Nb:SrTiO_3$ substrate. The higher atomic number of Pt compared to the the two oxides results in a much brighter contrast from this layer. (c) A high-magnification, high-resolution HAADF image of a hexagonal $YMnO_3$ film. Each atomic column can be resolved. The Y atoms appear brighter than the Mn atoms. The much lighter oxygen atoms are not visible. STEM images in (b) and (c) courtesy of Marta Rossell.

piezoresponse is distinguished from the quasi-static deflections due to topography by using a lock-in amplifier. By scanning the PFM tip over an area of the thin-film surface, the piezoeletric properties can be spatially resolved. Since in ferroelectrics the piezoelectric properties are defined by the direction of spontaneous polarization, PFM is heavily used to infer the domain structure of ferroelectrics. Finally, by applying a DC voltage that exceeds the coercive voltage of the ferroelectric, it is possible to switch the spontaneous polarization in areas of the film where the tip has touched, and thereby write domains with very high local control.

Scanning transmission electron microscopy

To connect the microscopic properties of the thin films with their structure at the atomic scale, STEM was performed in collaboration with Empa. The superior spatial resolution of STEM reaches below 1 Å, therefore allowing, in particular, imaging of atomic columns in crystalline materials. Figure 2.6 depicts a simplified sketch of the experimental geometry [112]. A lamella is cut out of the sample that is thin enough to enable good transmission of the electron beam. The bright-field (BF) detector records the transmitted intensity. Incoherent scattering is detected by the high-angle annular dark-field (HAADF) detector, where the intensity is roughly quadratic in

atomic number Z. The spatial resolution for STEM is mainly limited by the size of the electron probe beam on the sample [113]. Nowadays, sub-Å resolution is standard and state-of-the-art STEM can reach resolutions below 0.5 Å.

A recent development in state-of-the-art application of STEM involves mounting the lamella on a microchip, which allows applying a voltage to or heating of the sample. The in-situ heating of the sample during STEM imaging played a crucial part in the investigation of the structural phase transition in hexagonal manganite thin films, which is the topic of Chapter 6.

Optical second harmonic generation in thin films

3

This chapter introduces the nonlinear optical process known as second harmonic generation (SHG) and its application as probe of polar properties in thin films. This method has served as the workhorse characterization tool of this thesis. A particular focus is put on the integration of the SHG tool into the PLD growth environment. This was implemented as part of the ERC Advanced Grant project INSEETO and constituted the initial stage of this thesis work.

The following sections present the basic principles of SHG in thin films. A review detailing the most recent work using SHG as a probe of ferroic thin films is published as[44]:

J. Nordlander, G. De Luca, N. Strkalj, M. Fiebig, M. Trassin, Probing Ferroic States in Oxide Thin Films Using Optical Second Harmonic Generation, *Applied Sciences* **8**, 570 (2018).

3.1   Optical second harmonic generation

The interaction between a light field and the electric dipole moments[1] inside a material is described by

$$P(t) = \epsilon_0 \chi E(t),   \tag{3.1}$$

where $P(t)$ is the induced, time-varying electric polarization in the material, which arises in addition to any preexisting polarization, ϵ_0 is the vacuum permittivity, χ is the material-dependent electric susceptibility parametrizing the strength of the light-matter interaction, and $E(t)$ is the time-varying electric-field component of the propagating light [76, 77]. According to Maxwell's equations, a time-varying polarization with a non-zero second derivative, such as the sinusoidal oscillation induced by the electric field of a light wave, acts itself as a source of emitted electromagnetic radiation. This process defines the optical properties of a material.

---

[1]In the leading order electric-dipole approximation, this defines the light-matter interaction. For a complete description of the light-matter interaction, the material response has to be expanded in further multipoles, to include for instance magnetic dipole and electric quadrupoles contributions. These are, however, often negligible for optical processes with a non-vanishing electric-dipole response.
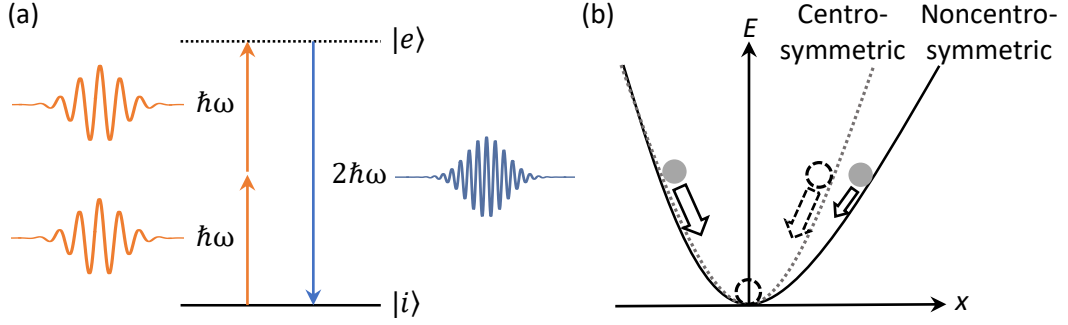
Figure 3.1: Visualizing the SHG process. (a) Frequency-doubling of light through two-photon conversion. (b) The symmetry-sensitivity of nonlinear optical processes in the ED approximation can be visualized considering an electron being driven to oscillate by a light field in a potential well. The total motion of the electron will consist of the driving frequency together with higher-frequency components to account for the anharmonicity of the potential. In a centrosymmetric potential, some of these higher-frequency contributions, among them $\chi^{(2)}$, will have to be zero.

For low electric-field amplitudes, χ is expressed by a rank-two tensor describing *linear* optical properties of the material, i.e., by the linear susceptibility $\chi^{(1)}$. It defines, for example, the refractive index n as $n^2 = 1 + \chi$. For intense light fields, such as can be obtained by laser light, the linear dependence of P on E no longer holds, and χ has to be expanded higher order terms of the electric field components of the light:

$$P(t) = \epsilon_0[\chi^{(1)} + \chi^{(2)}E(t) + \chi^{(3)}E^2(t) + ...]E(t). \tag{3.2}$$

Such expansion reveals additional, *nonlinear* optical processes. Equation (3.2) states that the induced polarization $P(t)$ can acquire a different time dependence than that of $E(t)$, and hence act as a source of light emission at new frequencies. The simplest of such nonlinear optical processes is optical second harmonic generation (SHG), i.e., the generation of frequency-doubled light. It appears already in the second term of the expansion in Eq. (3.2), and is thus related to the second-order nonlinear susceptibility. Assuming the waves propagating in the material are coherent and monochromatic at frequency ω, such as from a laser, we can express the electric-field component of the incident light as $E(t) = E_0 e^{-i\omega t} +$ c. c. Accounting for the vector properties of $P = [P_x, P_y, P_z]$ and $E = [E_x, E_y, E_z]$, SHG is then described in the frequency domain as an induced nonlinear polarization

$$P_i^{(2)}(2\omega) = \epsilon_0 \chi_{ijk}^{(2)}(2\omega, \omega, \omega)E_j(\omega)E_k(\omega), \tag{3.3}$$

where the indices i, j, and k are to be taken as a summation each over x, y, and z. This nonlinear polarization acts as source for light emission from the material at 2ω, i.e., it leads to the emission of SHG light.

In a more intuitive picture, SHG can be thought of as an instantaneous, conversion of two incident photons into a single, emitted photon having their combined energy in an energy-conserving process, see Fig. 3.1(a). This process is highly sensitive to the symmetry of the material. In the leading-order electric-dipole (ED) approximation employed here, nonlinear optical effects related to $\chi^{(2)}$ are only allowed in materials that are noncentrosymmetric, i.e., lacking a center of inversion, which includes all polar materials. This symmetry requirement for ED-SHG can be visualized considering an electron being induced to oscillate by a light field while sitting in a centrosymmetric vs. noncentrosymmetric potential well [77], see Fig. 3.1(b). In the centrosymmetric case, the forces on the displaced electron are identical upon spatial inversion. This leads to a symmetric oscillating motion of the electron that requires certain frequency terms to be zero. Here this corresponds to all terms vanishing that are odd in E in the expansion of χ (Eq. (3.2)): in particular, it requires $\chi^{(2)}$ = 0. Therefore, in the ED approximation, materials that are inversion symmetric do not emit SHG. For noncentrosymmetric materials, a subset of the $\chi^{(2)}$ components may still vanish, as a consequence of certain mirror and rotation symmetries in the material. The allowed components of the $\chi^{(2)}$ tensor are specified by the material's point-group symmetry.

While SHG in itself is a functional property of a material, used for example for wavelength-conversion in lasers [114], SHG can also function as a probe of certain materials properties, owing to its nondestructive nature and its sensitivity to the symmetry of the material. Hence, SHG is a revolutionary probe of functional properties that changes the symmetry of a material and which can be difficult to probe by other techniques. Applications range from probing the reduced symmetry of surfaces [115, 116] to characterizing ferroelectric and antiferromagnetic order [117, 118]. SHG can be measured in harsh environments such as at cryogenic temperatures and inside the thin-film growth chamber [44, 78]. SHG characterization of thin films was in particular made possible with the development of ultrashort-pulsed lasers, where high peak intensities could be achieved leading to high conversion efficiency in thin films despite the limited material volume.

3.2 Special considerations for SHG in polar thin films

As can be seen from Eq. 3.3, the SHG intensity, going as the square of the nonlinear polarization, is proportional to the square of the $\chi^{(2)}$ tensor and the square of the intensity of the fundamental beam, see Fig. 3.2. In ferroelectrics, the χ components are furthermore linear in the order parameter P_S, the spontaneous polarization. The SHG signal from a thin-film sample is in general the result of a combination of additional dependencies that require special considerations. They are summarized below.
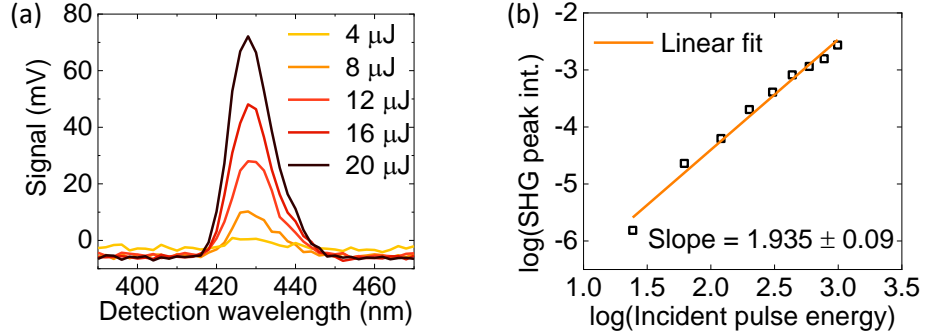
Figure 3.2: SHG response measured in our ISHG setup from a YMnO$_3$ thin film for fundamental radiation at 860 nm. (a) Spectral dependence of the signal measured by a tunable monochromator for different pulse energies of the fundamental beam. (b) Double-logarithmic plot showing the quadratic dependence (slope = 2) of SHG intensity on irradiated intensity.

Thickness effects

The amplitude of the SHG wave is proportional to the coherent nonlinear polarization response of the volume of material that the incident light beam probes. Therefore the SHG amplitude is linear in the film thickness × illuminated area, and its intensity grows as the square of the thickness (Fig. 3.3(a)) [76]:

$$I_{2\omega} \propto [t \cdot \chi^{(2)} \cdot I_{\omega}]^2.$$

(3.4)

Given a fixed beam diameter and a materials whose lateral dimensions are much larger than this diameter, where the microstructure of the material is uniform within this beam area, such as is common for thin films, it is sufficient to parametrize the SHG intensity in terms of the thickness t that the beam is travelling through. While a possible phase mismatch between the fundamental wave and the frequency-doubled wave, parametrized by the difference in refractive index between the two frequencies may reduce the overall SHG intensity in bulk crystals, this effect is vanishing for films up to several hundred nanometers in thickness. Another effect, however, that can result in a deviation from the expected quadratic thickness dependence of the SHG intensity is optical absorption of the fundamental and SHG light,

$$I(t) = I_0 e^{-\alpha \cdot t}$$

(3.5)

where the absorption at the SHG wavelength usually dominates. Typical absorption values for α in insulating oxides lie in the range of 10-100 cm^{-1} [119]. Thus, for most ultrathin oxide films, the optical absorption can be ignored. However, in the case of SHG propagation through a conducting oxide or metal layer, such as a top or bottom electrode, the absorption in this layer can be larger by several orders of magnitude, and in such a heterostructure, optical absorption can no longer be neglected. In addition, for a metallic layer covering the polar oxide, the reflectance of
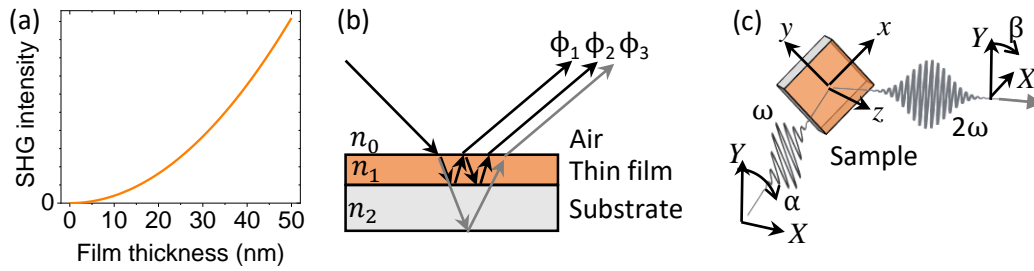
Figure 3.3: (a) Simulation of SHG thickness dependence, in case of negligible phase mismatch and low absorption (b) The propagation of a laser beam in a thin film sample. The difference in refractive index reduces the angle of incidence inside the sample compared to air (Snell's law). Multiple reflections in the films can yield SHG waves with different relative phases ϕ that depend on the thickness of the film. Also, a polished back side of the substrate may generate an additional SHG wave (gray) in the film that may not have the same phase as the beam reflected at the interface (black). (c) Definition of coordinate systems for the sample ($\chi^{(2)}$) as x, y and z and the light polarization component of the fundamental and SHG beam respectively as X, Y and Z.

the incident fundamental beam may be significantly higher than that of the insulating oxide surface, such that the intensity of the incident light in the thin film is significantly reduced, leading to decreased SHG.

Finally, for film thicknesses approaching $\lambda_{\text{SHG}}/4n$, that is, for thicknesses where the optical path inside the film approaches a quarter wavelength, destructive interference due to multiple reflections inside the heterostructure may also have to be considered [120] (Fig. 3.3(b)). In fact, such effects are already expected around a thickness of 50 nm, and can only be safely ignored for much lower thicknesses. Therefore, in the following, we restrict our quantitative thickness-dependent analysis of the SHG signal to thicknesses below 10 nm.

Other, secondary effects, stemming from thickness-dependent properties of the material itself, such as strain relaxation, phase transitions, gradient chemical composition or depolarizing-field effects in ferroelectrics, may also influence the SHG yield. Thus, after having corrected for the possible optical effects stated above, remaining deviations from the quadratic thickness dependence may be attributed to modification of one or several of these materials properties, all of which can, therefore, be probed by SHG.

Interference effects in films with sub-resolution crystallographic or polar domains

Laser-generated SHG is a coherent process where the SHG light has a defined amplitude and phase. Therefore, the SHG waves generated in different parts of a material will interfere, as long as they are within the coherence length of the light. In thin films, the domains, either with differing crystallographic orientation, such as

crystal twinning, or with differently directed polar axes, such as ferroelectric domains, often have a lateral extension much below that of the optical resolution limit ($< \lambda/2$). The SHG generated inside such different domains may differ in both amplitude and phase at a given light polarization configuration and the overall SHG response of the film reflects their interference as

$$I_{2\omega}^{\text{tot}} \propto [(\chi_{\text{A}}^{(2)} + \chi_{\text{B}}^{(2)})I_\omega]^2, \tag{3.6}$$

where $\chi_{\text{A,B}}^{(2)}$ denotes the amplitude and phase of the χ components in domain A and domain B, respectively, expressed in the same coordinate system. For antiparallel polarization domains of equal size, this results in destructive interference as the SHG amplitude is the same for both domain types, yet the phase differs by $180°$. In contrast, for orthogonal polar axes, interference can be seen in some, but not necessarily all, SHG components, see Ch. 4. For a single domain state in a ferroelectric, the overall phase of the SHG wave, related to the sign of the spontaneous polarization, cannot be measured. However, by using this principle of SHG interference, the *relative* orientation of polar states can be inferred by interfering the SHG waves of one domain type with a reference SHG wave from another source, such as a surface contribution of the sample [121] (see section below), or from an external reference generated in another crystal [122].

When the interfering domains exhibit an order among themselves, the macroscopic symmetry of the system reflected in the SHG response may be different than that of the individual domains. This could, for example, be ordered ferroelectric stripe domains [121]. Alternatively, in-plane twinning of crystallographic domains can also lead to an increase of the overall rotational symmetry of the system [123].

Equivalent to SHG interference of different domains in a single material, SHG waves from different materials in a thin-film heterostructure can also interfere.

Inversion-symmetry breaking at surfaces and interfaces

Crystals are not infinitely extended and have, in general, a reduced symmetry at surfaces and interfaces where their periodicity is interrupted. Often, inversion symmetry is broken at these positions, even if the material itself would be perfectly centrosymmetric. Therefore, SHG is commonly observed from surfaces. Indeed, SHG was first used in materials characterization as a surface probe [115].

In thin-film systems, this surface SHG interferes with the SHG from the film which can make it difficult to determine the origin of the SHG signal, especially if the SHG from the film is of the same order as the SHG from the substrate interface. The symmetry of the surface depends on the crystal symmetry and the orientation of the surface with respect to the crystal. The nonzero $\chi^{(2)}$ components for different surface symmetries are tabulated in the literature [124].

Measurement geometry

While SHG from noncentrosymmetric bulk crystals can be readily measured in almost any configuration, since they can be cut along the crystallographic direction of choice and subsequently polished for optical transmission, the epitaxial growth dictates the crystallographic orientation of thin-film samples. To still access polar properties along different crystallographic axes, different measurement modes are required. A normal-incidence measurement mode in transmission is used for projecting the light polarization onto the plane of the film, allowing us to access polar properties with in-plane $\chi^{(2)}$ components ($i, j, k \in x, y$). By tilting the sample with respect to the k vector of the incident light, i.e., in a tilted-incidence geometry, SHG stemming from the z components of $\chi^{(2)}$, often related to out-of-plane polar properties, can be detected. While the transmission mode is versatile in terms of sample orientation, transmission through certain substrates can cause absorption or birefringence of the light beams. A reflection measurement mode (Fig. 3.3(b,c)) can instead be employed where the beam is reflected at the interface between the film and the substrate. In this case, care should be taken if the backside of the substrate is polished, where additional reflections at this surface can cause unwanted interference effects (Fig. 3.3(b)). The $\chi^{(2)}$ components of the sample are evaluated from the characteristic dependence of the SHG intensity on the direction of the light polarization of the fundamental and SHG beams, so-called SHG polarimetry (see information box).

The SHG experimental configurations used for this thesis are depicted in Fig. 3.4. The SHG signal is usually selectively detected by using a monochromator or interference filter set at the SHG wavelength. The signal is usually integrated over the entire illuminated area for fast measurements. By replacing the collecting lens and photomultiplier with an objective and a CCD camera, the SHG signal can be spatially resolved. The resolution obtained can reach a few hundred nanometers, depending on the wavelength used and the numerical aperture of the optics. SHG in imaging mode is particularly powerful for visualizing ferroic domain structures or to locate and measure SHG in a specific spot on a sample.

> **Definition**
>
> **SHG polarimetry scans**   We define an *anisotropy* measurement as recording the SHG intensity while rotating the light polarization of the fundamental beam by angle α clockwise from $0°$ to $360°$ where $0°$ is parallel to the Y laboratory axis, see Fig. 3.3(c), with the SHG light detected at angle β, parallel or orthogonal ($90°$ offset) to α. A *polarizer* measurement is defined by a fixed angle β while rotating α as for the anisotropy measurement. In reflection geometry, light polarization along $0°$ is polarized perpendicular to the plane of reflection (s-polarized) while light polarization along $90°$ is polarized parallel to this plane (p-polarized).
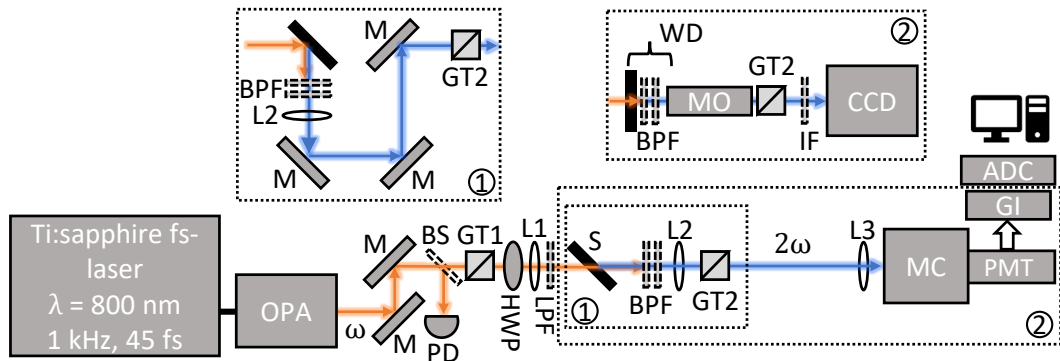
Figure 3.4: Schematic of the a typical experimental setup illustrating the different SHG geometries employed for this thesis work. A fs pulsed laser pumps an optical parametric amplifier (OPA) that is used for tuning the wavelength of the fundamental beam. The two mirrors (M) after the OPA are needed to align the beam in the setup. A beam splitter (BS) picks off a small part of the fundamental beam for monitoring the input intensity. A Glan-Taylor prism (GT1) is used to ensure defined linearly polarized light. A subsequent half-wave plate (HWP) is mounted on a rotation stage to rotate linearly polarized light hence setting its polarization direction. The lens (L1) focuses the beam onto the sample (S). Before the sample a low-pass filter (LPF) is used to filter out any previously generated SHG. After the sample, the fundamental beam is blocked by a band-pass filter (BPF), which only transmits the SHG light. The light is collected lens L2. In order to analyze the light polarization dependence of the SHG, a GT prism (GT2) is mounted on a rotation stage enabling selection of the polarization component to detect. A monochromator (MC) is used to set the wavelength to detect and a photomultiplier tube (PMT) converts the signal from optical to electrical. The signal is then integrated and digitally converted by a gated integrator (GI) and an analog-to-digital converter (ADC), respectively. This setup depicts SHG in transmission mode. The insets (1) and (2) indicate the necessary adjustments for reflection and imaging mode, respectively. In (2) the detection optics are exchanged for a microscope objective (MO) and a nitrogen-cooled CCD camera. The sample placement is dependent of the working distance (WD) of the objective.

3.3 In-situ optical second harmonic generation

The contact-free and non-destructive nature of SHG renders it perfect for in-situ and operando measurements. Yet, such applications of this technique have been mainly restricted to the analysis of surface symmetry during thin film deposition [125] and only in very few cases employed for probing emergent functional properties such as a spontaneous polarization. During this thesis, SHG was implemented into the PLD growth chamber, see Fig. 3.5. With the aim to probe emergent spontaneous polarization in ferroelectrics, this tool is a unique invention that enables real-time monitoring of the formation and evolution of polar states in the very moment that the material is constructed. It enables unparalleled insight into the polarization dynamics of polar materials in their growth environment and allows to design the polar properties in heterostructures in one-shot experiments that would otherwise require a tedious iterative process of growth and postdeposition characterization.
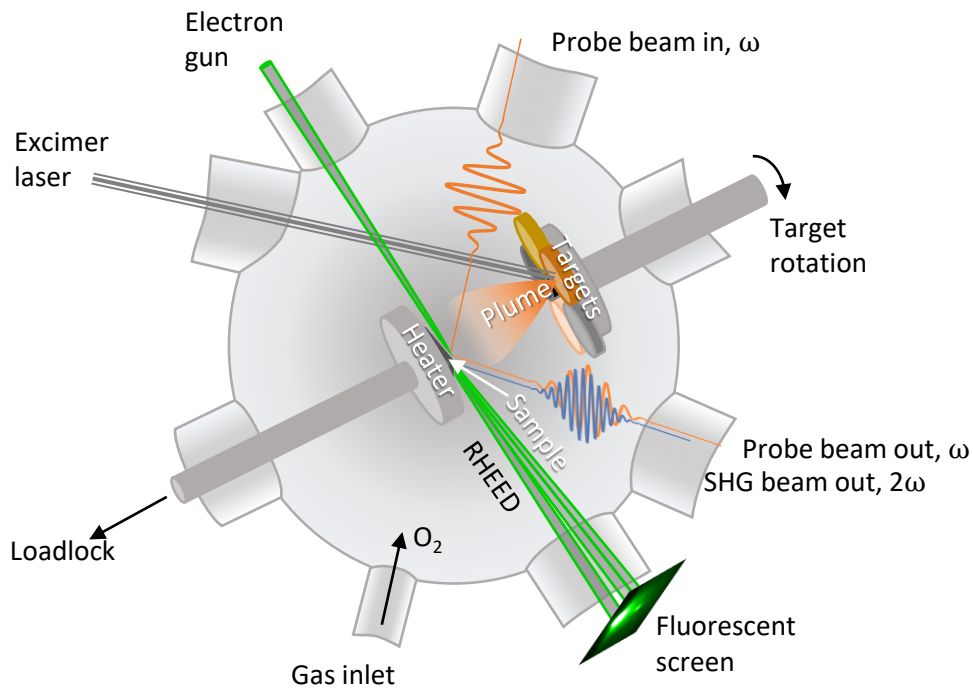
Figure 3.5: Schematic of the ISHG measurement geometry in the PLD chamber. The beams travel in and out of the vacuum chamber through a pair of windows. The measurement geometry is limited to reflection at a specific angle due to the position and diameter of the two windows.

The ISHG tool was co-developed by me during the time of this thesis as part of the ERC Advanced Grant INSEETO. In particular, as will be seen in Ch. 8, I extended the power of this tool beyond ferroelectric characterization, to also detect local symmetry breaking in layered oxides during the growth.

The ISHG intensity is measured with an integration time of about 1 second at fixed light polarizations. The ISHG measurement is synchronized with RHEED monitoring during deposition. The simultaneous RHEED analysis imposes, however, additional restrictions on the measurement geometry, since a RHEED diffraction pattern is only obtained for certain sample orientations. The imposed reflection geometry is nevertheless well suited for probing polar materials with an out-of-plane oriented polarization since this requires a tilted-incidence geometry and is largely independent on the sample alignment for RHEED. In contrast, for in-plane polarized materials, the optimal overlap between the light polarization and the polar axis depends on the azimuthal angle of the sample, which is heavily restricted by the RHEED alignment.

The full light polarization dependence at any given point in the growth can be measured by pausing the growth, measure anisotropy and polarizer scans, and then continuing the growth. Hence, information about the thickness dependence of a material's polar properties that usually requires the consecutive growth of many
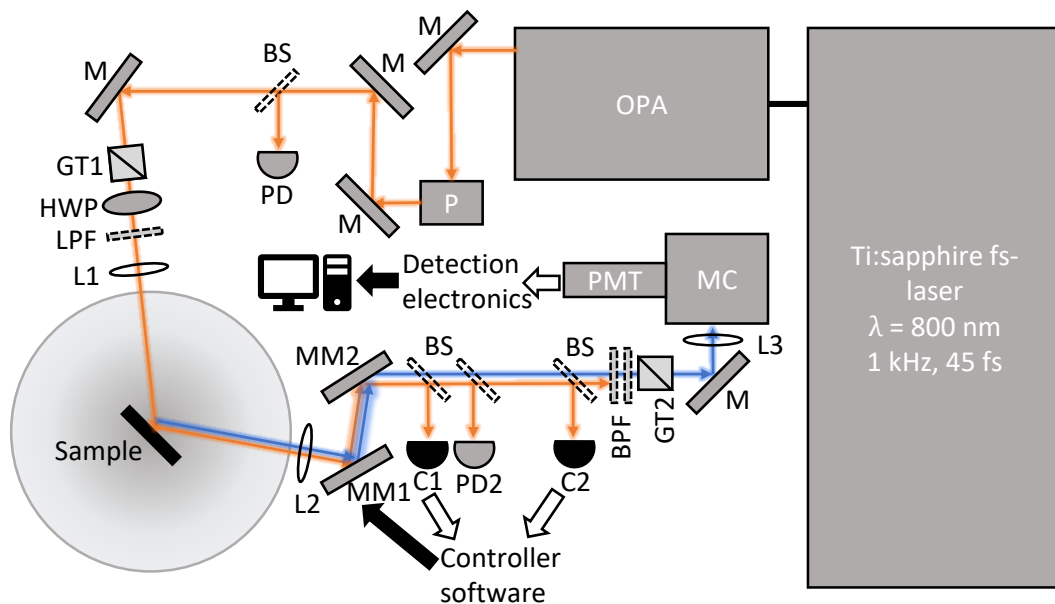
Figure 3.6: Schematic of the ISHG setup. A periscope (P) is needed to adjust the beam height to the PLD chamber. Two motorized mirrors (MM1,2) and two cameras (C1,2) are used for correcting the outgoing beams to reduce drift of the signal due to thermally induced movement of the sample. An additional photodiode (PD2) is used to monitor the reflected fundamental beam. Other components are labeled after Fig. 3.4. The beam diameter on the sample is focused to 250 μm.

sample and subsequent characterization, can be obtained in a single growth run with ISHG. With simultaneous RHEED monitoring, these properties can be directly related to the thickness down to sub-unit-cell precision.

Because of the large range of background pressure and sample temperature available in the PLD system, the ISHG probe can also be used to track polar properties that emerge after growth, at lower temperatures or different pressures.

Experimental setup

Figure 3.6 shows the experimental setup of ISHG as implemented with our PLD system. The reflection-mode geometry is similar to the one presented in Fig. 3.4. Because there can be considerable movement of the sample at elevated temperatures, such as during thin-film deposition, two cameras (C1 and C2) are used for monitoring the position of the outgoing beam and two motorized mirrors (MM1 and MM2) are used together with automated software to adjust the beam to an initially set beam path. This ensures that the beam is always aligned for optimal detection, and thus reduces long-term drift of the signal. During thin film deposition, the surface of the sample, and therefore also its reflectivity, can change rapidly. An additional photodiode (PD2) is therefore used to monitor the reflected fundamental beam.

"Roads? Where we're going, we don't need... roads."

Back to the Future, 1985.

Ferroelectric response of multidomain BaTiO$_3$ on Si

<div align="right">

4

</div>

This chapter discusses the ferroelectric multidomain architecture in BaTiO$_3$ films grown on silicon and its influence on the electric-field-dependent functional properties relevant for photonic applications. Using *operando* SHG we study ferroelectric BaTiO$_3$ thin films in device-like heterostructures. Exploiting the fingerprint SHG response of differently oriented polarization domains, we are able to disentangle the behavior of each domain state under application of an in-plane electric field. We find that the thin films intrinsically exhibit a multidomain state with coexisting domains oriented along all three principal crystallographic axis. Our operando SHG measurements further reveal that electrical poling induces 180° domain reorientation, while no indication of 90° reorientation is found. Beyond advancing the understanding of a complex domain architecture in BaTiO$_3$ on Si, the selective access to individual domain populations shown here suggest its prospect for multidirectional control of functionality in the rapidly developing field of hybrid oxide–semiconductor technology. The results summarized in this chapter are published as [126]:

J. Nordlander, F. Eltes, M. Reynaud, J. Nürnberg, G. De Luca, D. Caimi, A. A. Demkov, S. Abel, M. Fiebig, J. Fompeyrine, M. Trassin. Ferroelectric domain architecture and poling of BaTiO$_3$ on Si, *Phys. Rev. Mater.* **4**, 034406 (2020).

The manuscript can be found in its entirety in Appendix A.

4.1   Ferroelectric BaTiO$_3$ for silicon-based photonics

The prototypical ferroelectric BaTiO$_3$ has proven extremely successful in its thin-film integration with the established silicon-based technology platform [29, 127], thereby allowing to combine ferroelectric functionality with semiconductor electronics. A particular interest in BaTiO$_3$ thin films has emerged due to their pronounced electro-optic properties that are intimately linked with the orientation of the spontaneous polarization of the material. The strong linear electro-optic effect [77] (also known as the Pockels effect) found in BaTiO$_3$ can be used for energy-efficient modulation of light propagation in photonic devices [84], where light instead of electrons acts as carrier of information.
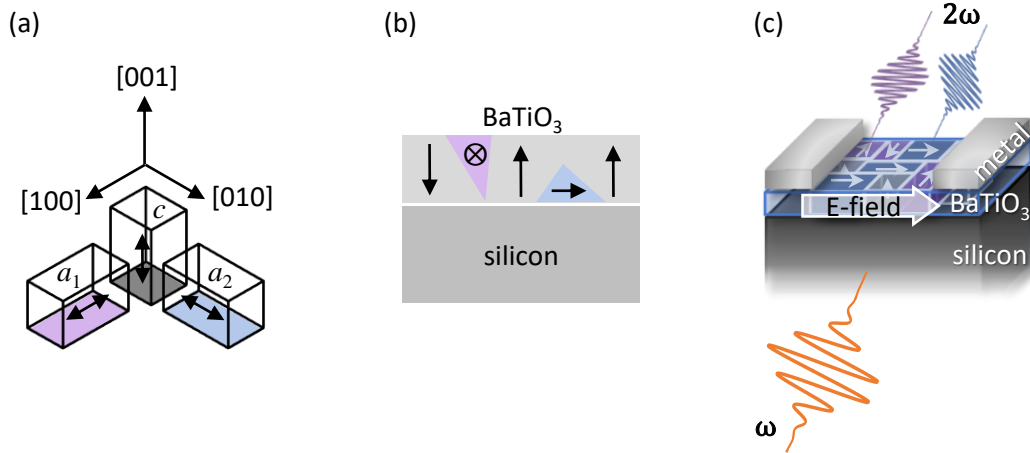
Figure 4.1: (a) Definition of the six possible polarization states with respect to the cubic BaTiO$_3$ lattice. The arrows indicate the polar axes. (b) Distribution of multiple polariztion domain states in the BaTiO$_3$films on Si. (c) The characteristic SHG response of each domain type allows *operando* monitoring of the domain architecture in BaTiO$_3$ during poling.

In ferroelectric materials like BaTiO$_3$, the macroscopic electro-optic response depends on the polarization distribution in the material. When integrating epitaxial BaTiO$_3$ films on Si substrates, the combination of epitaxial strain and a mismatch in thermal expansion between Si and the ferroelastic BaTiO$_3$ often yields a multidomain ferroelectric state as the sample is cooled down to room temperature after thin-film deposition [128]. In this system, the polarization can point in six different directions corresponding to $\pm$P along each principal crystallographic axis, see Fig. 4.1(a,b). In the following, we denote domains with their polar axis normal to the thin-film surface as c-domains, and domains with their polar axis along either of the in-plane directions as a-domains, where a_1 corresponds to polar axis along [100]$_{BTO}$ and a_2 corresponds to polar axis along [010]$_{BTO}$. In such a complex system, with up to six coexisting domain-state populations, the macroscopic polar properties become difficult to characterize. The macroscopic electro-optic response will be a result of the convoluted responses of those individual domain states. Furthermore, if the electric field is high enough, these polarization domains may switch their polarization to align with the applied field. Such switching events lead to new domain architectures where the change in net polarization magnitude and direction in the film leads to changes in magnitude or sign of the electro-optic response. For their successful implementation with silicon based electronics, an understanding of the manifestation of such domain architectures in ultrathin films and their behavior under the application of an electric field are of particular importance for predicting and optimizing device operation.
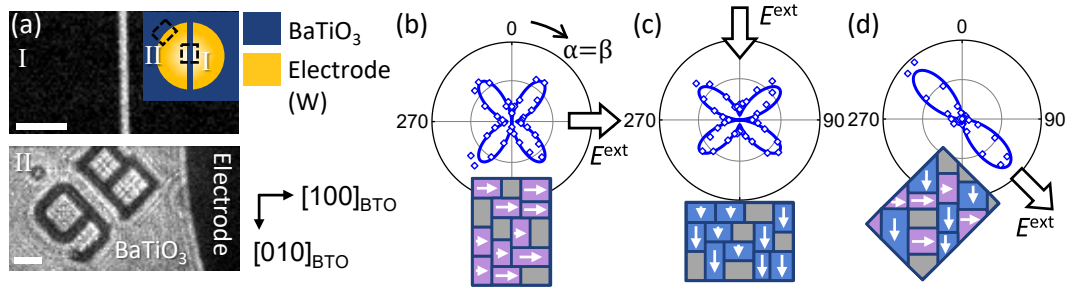
Figure 4.2: (a) SHG imaging allows monitoring the domain configuration in just the area where the electric field is applied. (b-d) While in the pristine $BaTiO_3$ film, no a-SHG is observed, the post-poling devices yield a a-SHG contribution whose characteristic polarization dependences yield a fingerprint of the different polarization configurations after poling in different directions poled, i.e. along (b) $[100]_{BTO}$, (c) $[010]_{BTO}$ and (d) $[110]_{BTO}$.

4.2 *Operando* SHG characterization of orthogonal ferroelectric domain populations in BaTiO₃ on Si

There are several challenges in probing orthogonal domain populations in a ferro-electric thin film on silicon during a poling sequence. In bulk crystals of $BaTiO_3$, switching between both anti-parallel polarization directions ($180°$) and between orthogonal polarization directions ($90°$) have been observed [129]. We therefore require a nondestructive method that can be applied *operando*, and that can give a distinct response from different domain populations even if the domains themselves are only a few tens of nanometer in size.

Many standard characterization techniques have been used to probe $BaTiO_3$ grown on Si, such as STEM, XRD and PFM, providing essential information on their ferroelectric properties. Yet, none of them fulfill all of our stated criteria. STEM can map the polarization direction in ferroelectric domains with atomic resolution, yet it is a decidedly destructive technique. XRD can detect the presence of differently oriented tetragonal axes, yet it does not distinguish between antiparallel oriented polarizations. PFM is non-destructive and can distinguish both antiparallel and orthogonal polarization directions down to domain sizes of approximately 50 nm. However for optimal piezoelectric response, an electrode below the film is needed to apply an electric AC-bias across the material. In $BaTiO_3$-based heterostructures designed for photonics, such a bottom-electrode layer is not compatible with device operation due to excessive absorption of the optical signal in the electrode material.

To overcome these challenges, we design an experiment where we take advantage of SHG as a noninvasive probe of the polarization state of the film. It does not require a bottom electrode since the probing field is supplied by the electric-field component of the incident laser pulse. The polarization direction of each domain population is distinguished by yielding a distinct light polarization and phase to the
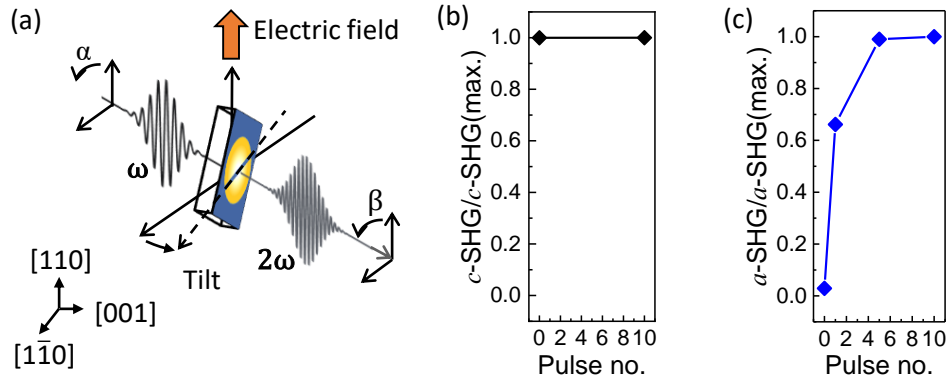
Figure 4.3: (a) When poling a_1- and a_2-domains simultaneously to produce an in-plane polarization along $[110]_{BTO}$, the sample can be oriented such that the c-SHG signal appears orthogonal to the a-SHG signal, and simultaneous monitoring of both contributions is thus possible. (b) and (c) *Operando* monitoring of the c- and a-SHG contributions, respectively.

SHG light wave, see Fig. 4.1(c). For sub-optical-resolution domain sizes, the SHG light from each domain-state population interferes, and the detected intensity during SHG polarimetry reveals a characteristic interference shape, serving as a fingerprint of the domain architecture. We deposit planar electrode pairs on the $BaTiO_3$ surface to apply an in-plane electric field to the film, mimicking electro-optic device operation. We use spatially resolved SHG imaging to single out only the SHG light from the active device area where the electric field has been applied (Fig. 4.2(a)). By comparing the SHG anisotropy (as defined in Ch. 2) in the as-grown state to that of the electrically poled state, we can infer the change in domain architecture without affecting the device itself or its operation.

We find that the pristine $BaTiO_3$ film on Si (before electrical poling) only shows a signature of out-of-plane-oriented polarization belonging to a c-domain population. This is in agreement with XRD characterization that shows a predominantly c-axis-oriented film. Yet, after the application of an in-plane electric field, an in-plane oriented polarization state is revealed, see Fig. 4.2(b-d). The unexpected presence of such a-domain-related SHG where there previously was none, warrants further investigation into the poling dynamics of the $BaTiO_3$ film. Recalling that both 90° (i.e. 'c-to-a') and 180° (i.e. 'a-to-a') domain reorientation is known to occur in $BaTiO_3$ bulk crystals upon application of electric fields in the a_1-a_2 plane [129], we consider each of these two cases to explain the appearance of a-domains. A c-to-a type of domain reorientation would suggest an initial absence of a-domains, where the applied electric field transforms a fraction of the c-domains to a-domains. In the case of pure a-domain reorientation, the pristine thin film would have to have an a-domain population intermixed with the c-domains, yet lacking a macroscopic net in-plane polarization.

To clarify the origin of these a-domains, we monitor the c-domain-related SHG

40

(c-SHG) signal simultaneously with the a-domain-related SHG (a-SHG) signal as a function of applied electric-field pulses in the plane of the film. We use an experimental configuration where a- and c-SHG are detected at orthogonal light polarizations such that the two signals do not exhibit mutual interference, and are hence independently measured. As seen in Fig. 4.3, this *operando* approach reveals a c-domain population that remains unchanged after the in-plane electric field application. The simultaneous appearance of a polarized a-domain population therefore indicates reversal within the preexisting a-domain population, whose net polarization averaged to zero in the unpoled state due to an equal distribution of polarization in all in-plane directions. Hence we conclude that the in-plane field acts exclusively on the preexisting a-domains, and the c-domain population remains intact throughout the process. Specifically, a c-to-a type of domain reorientation is not observed.

4.3 Discussion and outlook

The absence of c-to-a domain reorientation highlighted in this work points to a significant anisotropy of the BaTiO$_3$/Si system. This observation in the BaTiO$_3$ thin films stands in contrast to studies of domain reorientation in bulk BaTiO$_3$ crystals, and remains an open question that will require further work. We note, that in contrast to other thin-film perovskite ferroelectrics, such as PbTiO$_3$, c-to-a domain reorientation in BaTiO$_3$films is also not extensively discussed in the literature. It is possible that the epitaxial strain present in the ultrathin regime of the BaTiO$_3$films integrated on Si, that favors the predominant formation of c-domains, also leads to domain pinning. This strain may thus lift the energy degeneracy between a- and c-domains. It is therefore possible that at some higher electric-field values, c-to-a domain transformation could take place. While such an experiment was outside our scope in this work, we suggest that the SHG method presented here would be ideally suited to detect this domain transformation, presenting an opportunity for follow-up studies. We further note, that the absence of *in-plane* anisotropy in this thin-film system implies that the a_1- and a_2-domain states remain degenerate in energy, and begs the question if a_1-to-a_2 domain reorientation occurs. This scenario is slightly more complicated to investigate, as it requires poling in, at first, one selected in-plane direction, and subsequent monitoring of this polarized domain population during poling in the orthogonal in-plane direction. To enable this type of experiment, the design of a four-terminal device on top of the BaTiO$_3$ films would be required. The combined results of the two follow-up experiments suggested here would provide even further insight into the ferroelectric domain dynamics of BaTiO$_3$ integrated on Si.

Finally, we note the complex multidomain architecture revealed in this study

provides a system with a mixed in-plane and out-of-plane polar anisotropy, where we have shown that the individual domain populations can be manipulated separately with oriented electric fields. This opens up for new device concepts that offer advanced functionality and versatility [130], both for photonic but also electronic applications, offering controlled switching between more remanent polarization states, compared to a perfectly uniaxial ferroelectric system.

Competing polar phases in highly strained BiFeO$_3$

<div style="text-align:right">5</div>

In the previous chapter, we saw how the symmetry sensitivity and noninvasive nature of SHG enabled distinguishing differently oriented polar axes in a multidomain, yet single-phase, ferroelectric thin film. In this chapter, we exploit this same principle of our SHG probe, but here applied to a system where different polar *phases* coexist. We furthermore take an additional step and instead of using *operando* characterization to infer the polar domain architecture after it has already formed, we now follow the very emergence of the polar phases *in situ* in the dynamic environment of our growth chamber. Here, we investigate the polar properties of BiFeO$_3$ at highly compressive epitaxial strain. At this strain-driven morphotropic phase boundary, a series of competing metastable polar states, including a supertetragonal phase and several monoclinic phases, can coexist. This system is envisioned for novel energy-efficient device concepts as it is highly susceptible to external stimuli such as temperature, pressure or electric field [131]. However, because of the complex composition of the different metastable phases, the parameters governing the emergence of polarization in such thin-films have yet to be fully explored. Using ISHG, we provide unique insight into the formation and evolution of these coexisting polar states in the ultrathin regime. We study in particular the polar behavior BiFeO$_3$ in relation to electrostatic boundary conditions upon insertion in capacitor-like heterostructures. Our results demonstrate the unique robustness of polarization in the ultrathin regime of the strain-driven supertetragonal phase, yielding a striking absence of critical thickness.

The results presented in this chapter are partly published as [132]:
J. Nordlander, A. Maillard, M. Fiebig and M. Trassin. Emergence of ferroelectricity at the morphotropic phase boundary of ultrathin BiFeO$_3$, arXiv:2005.09685 (2020). The manuscript can be found in its entirety in Appendix B.
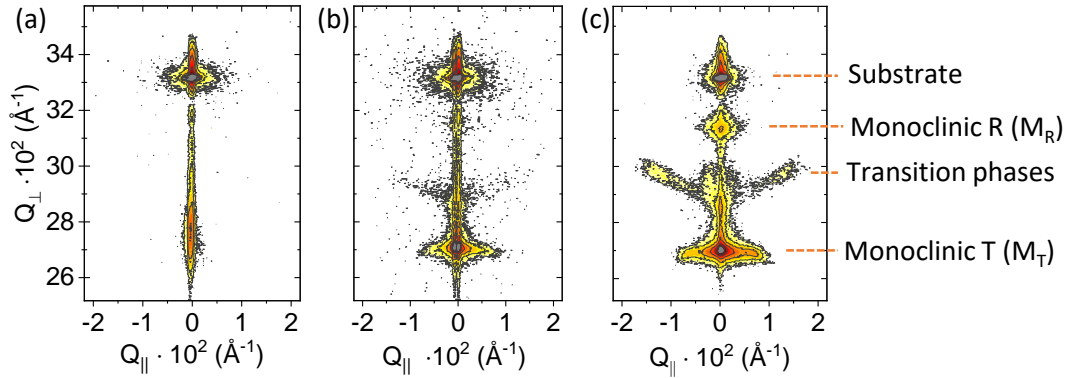
Figure 5.1: X-ray RSM of symmetric reflections for different thicknesses of BiFeO$_3$ films grown at -4.5% lattice mismatch on CCMO-buffered LaAlO$_3$: (a) 10 unit cells, (b) 60 unit cells, (c) 80 unit cells. The reflections corresponding to different monoclinic phases of BiFeO$_3$ are indicated.

5.1 The strain-driven morphotropic phase-boundary in BiFeO$_3$

In BiFeO$_3$, the morphotropic phase boundary is strain-driven and is therefore best accessed in thin films where sufficiently large strain can be imposed in the material by choice of substrate. The phase diagram of this system has already been extensively characterized [81, 83, 89, 90]. It was observed that the films are purely tetragonal (denoted T in the following) at high compressive strain and high temperature. Below ∼450 °C, the tetragonal phase develops a small monoclinic tilt, entering a T-like monoclinic phase, which we denote by M$_T$. At even lower temperatures, inclusions of rhombohedral- (R-) like monoclinic phase, here denoted by M$_R$, together with a set of monoclinic transition phases between M$_T$ and M$_R$, are formed in the films, as a mechanism to relax the epitaxial strain. This strain relaxation occurs gradually with increasing film thickness such that a coexistence of M$_T$ and M$_R$ phases is only observed above a certain film thickness, the value of which is dependent on the growth conditions and defect chemistry of the films [133]. Because of the low energy difference between these metastable polar phases, BiFeO$_3$ films close to the morphotropic phase boundary exhibit very large responses to external stimuli, mediated by phase transformations. Such behavior is the reason for the technological relevance of PZT [42], where the morphotropic phase boundary is composition-driven. Hence, highly strained BiFeO$_3$ reveals itself as a prominent new candidate for ferroelectric-based devices [134].

5.2 Evolution of polar phases in compressive strained BiFeO$_3$ films

So far, the most common approach for investigating the thickness and strain dependence of the different polar phases in BiFeO$_3$ has been through a combination of PFM and XRD. However, both of these methods yield only post-deposition information. The high T$_C$ of BiFeO$_3$ renders it ferroelectric already at the temperature of epitaxial growth, and thus the polar state is set during deposition. Hence, the formation of the polar states in highly strained BiFeO$_3$, especially in the ultrathin regime and in heterostructures, remains so far unexplored. Here, we use ISHG to build on the knowledge attained from PFM and XRD and expand the understanding of polar phase formation in compressive strained BiFeO$_3$ to include the growth process itself, where we access the metastable polar phases in situ. SHG has already been established as a highly sensitive probe of the different monoclinic phases in BiFeO$_3$ films at ambient conditions [121, 135]. Therefore, we can correlate changes in ISHG response both to the onset of polarization in general in the films, directly during heterostructure growth, as well as to its evolution and phase transformations during post-deposition cooling.

By growing our BiFeO$_3$ thin films on a substrate with -4.5% compressive lattice mismatch (here, on (001)-oriented LaAlO$_3$ buffered by conducting Ce$_{0.04}$Ca$_{0.96}$MnO$_3$ (CCMO)) we place the BiFeO$_3$ films close to the morphotropic phase boundary. This state is confirmed by post-deposition x-ray RSM (Fig. 5.1), where the expected, highly thickness-dependent, phase transformations from solely M$_T$ in ultrathin films of 10 unit cells (Fig. 5.1(a)), to multiple phase coexistence (Fig. 5.1(c)) at 80 unit cells are seen by the gradual appearance of additional reflections in the diffraction pattern.

Temperature-dependent ISHG on these films reveals the presence of a spontaneous polarization belonging to the epitaxially stabilized supertetragonal phase at the growth temperature. This is in agreement with previous reports, and here we find that this phase is preserved throughout the growth up to film thicknesses of at least 80 unit cells. This claim is confirmed by our ISHG data (see Fig. 5.2), where signatures of the monoclinic phase transitions are only observed during post-deposition cooling and occurs below 460°C, that is, significantly below the epitaxial growth temperature of 670°C. In agreement with literature [81–83], we relate the transition above 390°C to the global onset of monoclinic distortion in the films, transforming the T phase to the M$_T$ phase. Aside from this transition, the films that exhibit R-like phase inclusions (as confirmed by PFM), also reveal a signature of a second transition around 200°C in the ISHG response (Fig. 5.2(b)), which we therefore associate to the formation of the R-like phase.
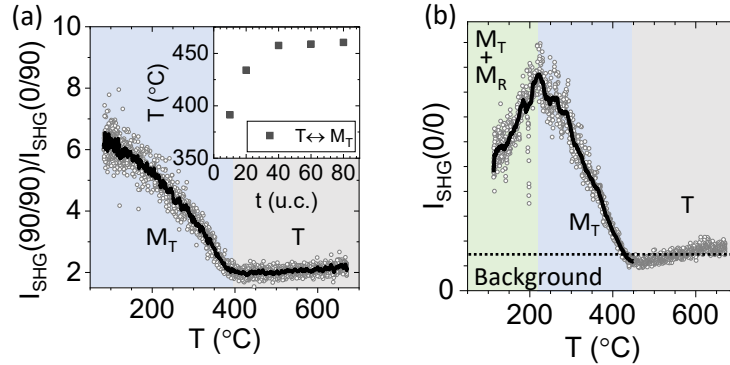
Figure 5.2: The ISHG signal for different light polarization configurations, corresponding to different $\chi^{(2)}$ components, monitored during sample cool-down. A clear transition is observed at the onset of monoclinic distortion. (a) All films exhibit signatures of a phase transition from T to M_T. The inset shows the thickness dependence of this phase transition temperature. (b) For films where inclusions of the M_R phase also exhibit signatures of a second phase transition in one of the SHG components around 200°C. The dotted line indicates the SHG background level caused by surface contributions.

5.3 Stability of the high-temperature supertetragonal polar state in heterostructures

Having established the thickness-temperature phase diagram of our highly strained $BiFeO_3$ films, it is clear that the supertetragonal phase of the $BiFeO_3$ during growth is distinct from the phases at room temperature. To understand the emergence of polarization in these films, it is thus essential to study the polar properties of this high-temperature phase during thin-film growth.

As seen in Fig. 5.3(a), at the start of the $BiFeO_3$ growth on CCMO-buffered $LaAlO_3$, there is an immediate onset of ISHG, where ISHG polarimetry confirms the 4*mm* point-group symmetry of a tetragonal polar phase (Fig. 5.3(b)). Since the evolution of ISHG intensity in the $BiFeO_3$ films is related to the evolution of the spontaneous polarization P_S as $I_{ISHG} \propto |P_S t|^2$, where t is the thickness of the film, the thickness dependence of the ISHG signal shown in Fig. 5.3(c) reveals a striking zero critical thickness for polarization. Indeed, even when omitting the bottom electrode, and depositing the $BiFeO_3$ directly on the insulating $LaAlO_3$ substrate, we find only a small critical thickness of two unit cells. The exceptional robustness of polarization in the ultrathin regime demonstrated here is unusual for most perovskite-structured tetragonal ferroelectrics (as discussed in Ch. 1), and is furthermore in stark contrast to ground-state R-like $BiFeO_3$ films, which exhibit a critical thickness of four unit cells during growth on conducting substrates [78].

To further evaluate this unusual stability of the supertetragonal polar state, we monitor the evolution of polarization during fabrication of ultrathin capacitor-like $CCMO|BiFeO_3|CCMO$ heterostructures. For other tetragonal ferroelectrics, such as
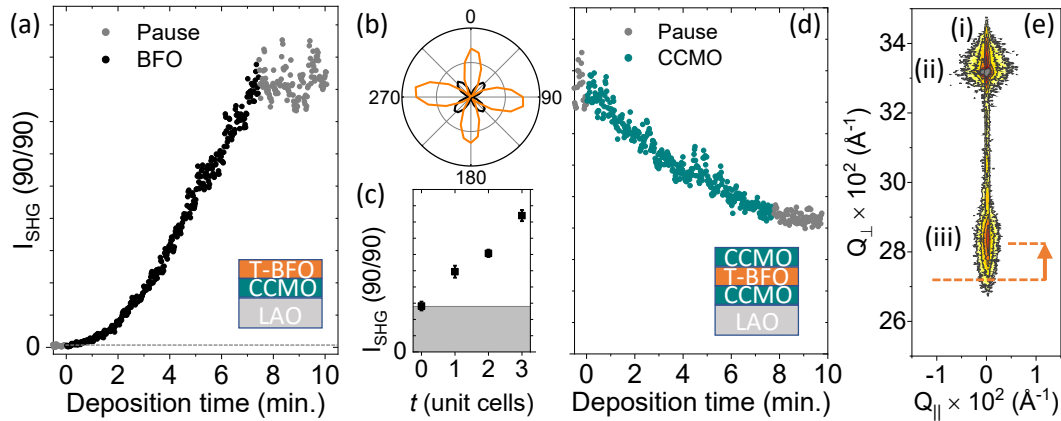
Figure 5.3: (a-c) ISHG measurement during growth of a CCMO | BiFeO₃ | CCMO heterostructure. (a) ISHG response during deposition of a 20-unit-cell BiFeO₃ layer, grown on CCMO-buffered LaAlO₃. (b) The ISHG polarizer scans, with light detected at 0° (black) and 90° (orange), show a polarization dependence compatible with the 4*mm* point-group symmetry of the T phase. (c) ISHG intensity is seen from the very first BiFeO₃ unit cell, indicating an absence of critical thickness. (d) During deposition of the CCMO cap layer, the SHG intensity drops. No discontinuities due to domain splitting or phase transformation of the underlaying tetragonal BiFeO₃ layer are observed, and the reduced intensity is assigned to a combination of optical absorption in CCMO and reduced tetragonality with associated reduced polarization in the BiFeO₃ layer. (e) X-ray RSM of the the capped tetragonal BiFeO₃ film in (d) around the CCMO (i), LaAlO₃(ii) and BiFeO₃(iii) reflections, showing the reduced c lattice constant upon capping (upper dashed line). The c lattice constant of the uncapped sample (data not shown) is indicated by the lower dashed line, where the difference between the two is indicated by the arrow.

BaTiO₃, inserted into such heterostructures, it has been shown that enhancement of the depolarizing field in the ferroelectric layer can occur at the early stages of top electrode deposition, leading to abrupt domain splitting as a means to reduce the net polarization of the system [75]. Here, in contrast, we observe a steady decrease of ISHG intensity (Figure 5.3(d)) that cannot stem from such abrupt domain formation, nor does it exhibit changes in the ISHG symmetry that could be related to a phase transformation into one of the monoclinic phases. While part of the loss in ISHG intensity can be associated to optical absorption in the CCMO electrode layer, we identify a reduced tetragonality by up to 15% of the capped BiFeO₃ (Figure 5.3(e)) as an additional attenuating mechanism: the corresponding reduction of the spontaneous polarization manifests as a reduced ISHG yield. Based on this observation, we suggest that a depolarizing field induced by the imperfect charge screening at the BFO-CCMO interface causes a partial polarization suppression [136] rather than domain splitting. Preliminary theoretical calculations further support this claim, indicating a very large energy cost related to domain
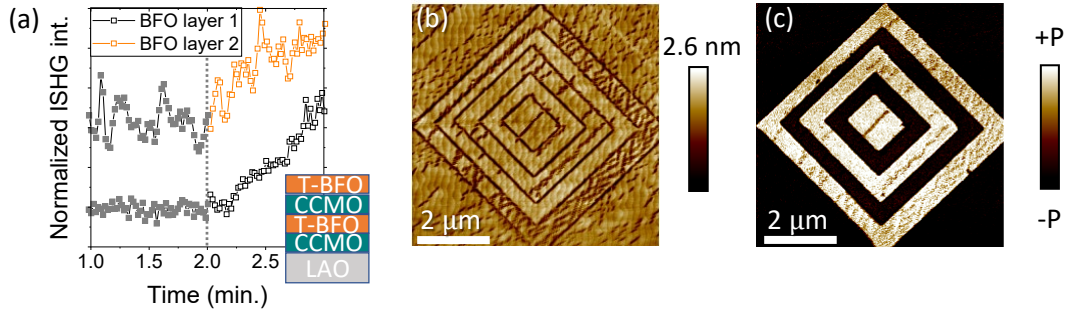
Figure 5.4: (a) Comparison of ISHG response from the first and the second BiFeO$_3$ layer in a BiFeO$_3$ | CCMO multilayer (sketched in the inset). Both layers exhibit immediate onset of ISHG intensity from the first unit cell, and hence a zero critical thickness. The two graphs are shifted along the vertical axis for visibility. (b,c) Ferroelectric phase coexistence in BiFeO$_3$ thin films grown on CCMO-buffered LaAlO$_3$ visualized by PFM. The lower c lattice parameter of the M$_R$ phase compared to that of the M$_T$ phase leads to valleys in the topography scan, such that darker areas can be identified with the presence of M$_R$ phase inclusions. (b) Topography. (c) Out-of-plane PFM signal of the same area as in (b). Electric-field application of ±5 V during PFM switches the polarization direction of the M$_T$ matrix, but also affects the distribution of M$_R$ phase, as seen when comparing the topography scan (b) and the corresponding switched out-of-plane component of the polarization in the PFM scan (c). Note that M$_R$ phase inclusions are always observed at the artificially written domain walls.

formation in supertetragonal BiFeO$_3$.[1] Strikingly, however, this is far from a full suppression of polarization. We therefore find that the supertetragonal polar state prevails in ultrathin heterostructures, pointing to the immense potential of this system for ultrathin ferroelectric-based devices.

5.4 Discussion and outlook

Given the peculiar robustness of polarization in ultrathin, supertetragonal BiFeO$_3$ demonstrated in this work, it is interesting to go on to explore its evolution in more advanced heterostructures, to investigate potential influence of strain relaxation. Our preliminary results on the continued growth of the BiFeO$_3$|CCMO multilayer is seen in Fig. 5.4. The growth of a second layer of BiFeO$_3$ on top of a similar capacitor-like heterostructure as shown in Fig. 5.3, exhibits the same zero critical thickness as the single layers. We further see from XRD analysis that the tetragonality of this (uncapped) top BiFeO$_3$ layer is restored to its initial value of 1.20, even while in the buried BiFeO$_3$ layer it remains suppressed. This serves as further proof that the reduced tetragonality of the capped BiFeO$_3$ is not due to strain relaxation or sample degradation.

We furthermore expect that the robustness against domain formation in the tetragonal phase prevails to some extent in the M$_T$ phase. As seen in Fig. 5.4,

---

[1]B. F. Grosso, N. A. Spaldin et al., in preparation

applying an electric field to switch the polarization of this T-like phase out-of-plane always seems to be accompanied by formation of the R-like phase at the domain walls. Therefore, just as for the supertetragonal phase, $180°$ domain walls between domains of antiparallel polarization states are not observed in the M_T phase. Instead, the polarization reversal is mediated by additional monoclinic phases.

The tetragonal $BiFeO_3$ close to the morphotropic phase boundary thus constitutes a unique polar system that is robust exactly when we want it to be, i.e., to achieve a deterministic domain state during the dynamic electrostatic conditions of thin film heterostructure growth, and still enables switching when we need it to, namely, at room temperature, by virtue of the low-temperature phase co-existence with giant piezoelectric and ferroelectric response. This is in stark contrast to most tetragonal perovskite ferroelectrics, such as $BaTiO_3$, where the early stage of polarization emergence is the most susceptible to perturbations. The results presented in this work therefore reveals the tantalizing polar properties of tetragonal $BiFeO_3$, in particular when inserted in heterostructures. With this work, we lift forward this highly strained $BiFeO_3$ system as topic for further attention and future studies. For example, the comparison between interlayers of different lattice mismatch and different charge-screening properties should be made. Since we observed a finite, albeit small, critical thickness in the tetragonal $BiFeO_3$ grown directly on $LaAlO_3$, we suggest that further studies of depolarizing field effects could be made using $LaAlO_3/BiFeO_3/LaAlO_3$ type heterostructures, where incomplete charge screening at both top and bottom interfaces leads to a stronger depolarizing field. Such experiments could determine routes for manipulation or design of the domain configuration in this, on the one hand, metastable, on the other hand seemingly 'superstable', polar state.

Geometric improper ferroelectricity in epitaxial h-YMnO$_3$ films

6

We have seen that ISHG provides unprecedented insights into both polarization dynamics and thickness-dependent phase transitions in thin films of proper ferroelectrics. In this chapter, we will compare this behavior to that of improper ferroelectrics, where the impact of epitaxially defined electrostatic and mechanical boundary conditions on the driving order parameter also contribute to defining the polar state. Improper ferroelectrics promise a unique robustness against depolarizing-field effects, allowing the presence of exotic domain patterns, polarization discontinuities and suggesting retention of the polar state in the ultrathin limit [99, 104, 105]. However, so far, most of the existing work on improper ferroelectrics deals with bulk properties and experimental studies on epitaxial confinement and size effects at the nanoscale in ultrathin films remain scarce.

Here, we investigate improper ferroelectricity in epitaxial hexagonal manganite films, where the primary order parameter is a lattice distortion. We disentangle the respective behavior of these two coexisting order parameters by independent access using two complementary in-situ techniques. While ISHG follows the emergence of polarization, in-situ STEM provides real-space mapping of the primary order across its phase transition. We demonstrate the crucial impact of epitaxial constraints at the substrate interface on the emergence of polarization. In particular, despite the prediction of zero critical thickness, we nevertheless find a threshold thickness for the improper polarization. We show that this is a result of mechanical rather than electrostatic boundary conditions, which act on the primary order parameter. These results highlight the importance of considering both order parameters in improper ferroelectric thin films for understanding, and ultimately controlling, their functionality. The work summarized in this chapter is published as [137]:

J. Nordlander, M. Campanini, M. D. Rossell, R. Erni, Q. N. Meier, A. Cano, N. A. Spaldin, M. Fiebig, M. Trassin. The ultrathin limit of improper ferroelectricity, *Nature Communications* **10**, 5591 (2019).

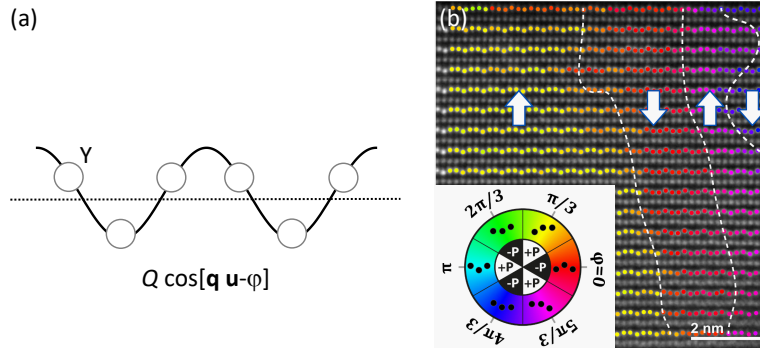The manuscript can be found in its entirety in Appendix C.

Figure 6.1: (a) The relation between structural distortion in terms of Y-ion corrugation in YMnO$_3$ and the trimerization state, parametrized by Q and φ as introduced in Ch. 1, after Ref. [95]. (b) STEM image of YMnO$_3$ film grown on Pt-buffered YSZ, showing the nanoscale trimerization domain structure. The inset shows the color code of the six trimerization states and their corresponding polarization state. Reprinted in part from Ref. [137].

6.1 Improper ferroelectricity in the ultrathin regime

The rich physical phenomena and unusual functionality found in improper ferroelectrics have put these materials in the research spotlight in terms of bulk crystals. As described in Ch. 1, the family of hexagonal manganites stands out in the class of improper ferroelectrics, with its intriguing multiferroic and topological features. The family of hexagonal manganites is one of the most studied classes of improper ferroelectrics and therefore often used as model system. Indeed, in bulk single crystals, the coupling between the primary order parameter – the lattice trimerization $\mathbf{Q}$ – and the improper polarization, $\mathbf{P}_S$, has been extensively studied [92, 93]. However, despite possessing many exotic properties that carry great potential for implementation in novel oxide electronic applications, it is not understood how the improper ferroelectric state transfers to the ultrathin limit of epitaxial films. In particular, even though the polarization properties have been treated both experimentally and theoretically in thin films [105, 138–141], the behavior of the primary order $\mathbf{Q}$ in an epitaxial system, including its coupling to $\mathbf{P}_S$, has not been considered. As will be seen in the following, the interplay between epitaxy and the lattice trimerization completely governs the improper polar state, with unexpected finite size effects as a result. Only by considering the two order parameters together, were we thus able to develop a full understanding of the ultrathin limit of improper ferroelectricity.

6.2 Emergence of improper polarization h-YMnO$_3$ ultrathin films

There are several challenging aspects that have hindered the study of geometrically driven improper ferroelectricity in hexagonal manganite thin films. First, the

achievement of epitaxial growth of the hexagonal phase depends on finding suitable substrate materials. Considering that most commercially available oxide substrates are cubic or orthorhombic, only a selected few provide adequate lattice matching with the hexagonal manganites for achieving high-quality epitaxial growth. Second, suitable techniques for probing both polarization and trimerization in ultrathin films are required. In Ch. 7 we will address the epitaxial-growth optimization of h-RMnO$_3$ films in further detail. In this chapter, we focus on the second issue, namely, probing an improper ferroelectric state and correlating it to its primary order parameter, all in the limit of ultrathin films.

For this study, we choose as our model system hexagonal YMnO$_3$, one of the most studied members among the hexagonal manganites. We grow a thickness series of YMnO$_3$ thin films on (111)-oriented yttria-stabilized zirconia (YSZ) by PLD. We use ISHG as probe for the spontaneous polarization, allowing us, just as in the previous chapter, to probe the emergence of improper ferroelectricity directly in the growth environment. We also note that ISHG allows us to probe the spontaneous polarization in the films even without a bottom electrode for electrical contact. While YMnO$_3$ can be grown on a conducting buffer layer, omitting this layer significantly simplifies our thin-film growth requirements. The lattice trimerization in our films can be conveniently mapped, in terms of both magnitude and domain structure, using STEM [95] (Fig. 6.1). Since the structural distortion, with its characteristic corrugation pattern of Y atoms, corresponds to relatively large atomic displacements (up to 40 pm), it can even be seen in the unprocessed images directly by eye. For this study, a newly developed microchip for in-situ heating during STEM imaging enabled us to perform temperature-dependent real-space mapping of the trimerization for the first time in these films. Hence, by bringing together these two state-of-the-art in-situ probing techniques, we achieve unique and independent access to each order parameter.

Our ISHG study of the emergence of polarization in the films show that, even though our films are grown below the bulk ferroelectric T$_C \approx$ 1250 K, none of these films, up to at least a 120-unit-cell thickness, develops a spontaneous polarization during growth. Instead, we reveal that the onset of improper polarization occurs at much lower temperatures, during post-deposition cooling. We furthermore observe a strong thickness dependence of the ferroelectric T$_C^{film}$, where the transition temperature decreases with decreasing film thickness see Fig. 6.2(a). We find a threshold thickness for polarization of 2 unit cells. We note that such a thickness dependence of polarization resembles that of proper ferroelectrics, where a suppression of polarization is caused by the depolarizing field [63]. However, such behavior is in stark contrast to theoretical predictions on improper ferroelectric thin films [105], where it was shown that the depolarizing field cannot suppress the leading order trimerization and the polarization remains.

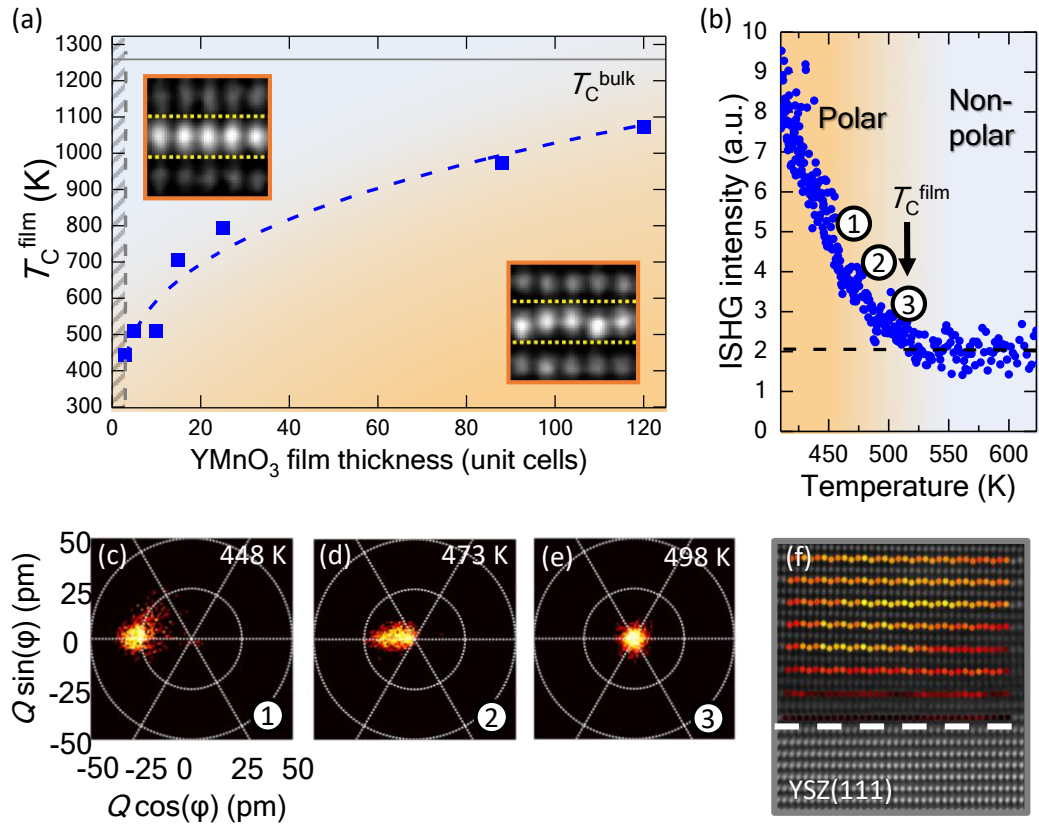To elucidate the origin of this thickness dependence in the YMnO$_3$ films, we

Figure 6.2: (a) Thickness dependence of ferroelectric T_C. The insets show STEM images for polar and nonpolar phase. (b) ISHG intensity vs. temperature from a 10 unit cell thick YMO film. (c-e) STEM measurement of $\mathbf{Q}$ in same sample as in (b) vs. temperature. (f) Clamping of $\mathbf{Q}$ to $Q = 0$ at the substrate interface.

compare the ISHG polarization measurements with temperature-dependent STEM mapping of $\mathbf{Q}$. By mapping the trimerization amplitude using STEM while heating a 10-unit-cell film across the phase ferroelectric transition, identified by ISHG to be 500 K (Fig. 6.2(b)), we find that the primary order vanishes at precisely the same temperature (Fig. 6.2(c-e)). From this observation we draw two important conclusions about the improper ferroelectric state in the thin films: (1) the improper coupling between the two order parameters $\mathbf{Q}$ and $\mathbf{P}_S$ remains rigid down to the ultrathin limit and (2) therefore the reason for suppression of the phase transition and the observed threshold thickness must be explained by mechanisms acting on the primary order parameter and manifested in the polarization through their coupling, rather than by mechanisms affecting primarily the polarization, such as the depolarizing field.

Close inspection of the trimerization near the substrate interface reveals a diminished amplitude Q in the first few YMnO$_3$ layers (Fig. 6.2(f)). We relate this pinning of an untrimerized YMnO$_3$ layer to mechanical boundary conditions of the

substrate incompatible with the immediate onset of a distorted hexagonal lattice. We note that this 'substrate stiffness' is to be differentiated from epitaxial strain. In fact, we find that despite the lattice mismatch of 2.1% between the substrate and film, the films retain bulk-like in-plane lattice constants, mediated by the formation of misfit dislocations at the film–substrate interface. Rather, the density-functional calculations suggest that clamping of the very first unit cell closest to the interface in an untrimerized state is not only the cause of the slow build-up of Q with distance from the substrate, yielding the 2-unit-cell threshold thickness, but also sets structural boundary conditions for the primary order parameter. This imposes strong finite-size effects on the system that decrease the transition temperature of the trimerization at low film thickness. In earlier studies, the mechanical boundary conditions at the substrate interface were not considered, and this may explain the premise for the original prediction of zero critical thickness in the hexagonal manganites [105].

Finally, our detailed visualization using STEM imaging provides unique insights into the structural phase transition. As we approach the transition temperature, we not only observe how the average amplitude Q goes to zero, but we also find an elongation of the average atomic positions. Since the images reflect a projection of many unit cells along the zone axis, such an elongation suggests the presence of a locally defined distortion that is lacking long range order. In fact, the observed elongation is the signature of an unconventional type of structural order-disorder phase transition that was recently seen in high-temperature neutron-diffraction experiments on bulk crystals of $YMnO_3$ [142]. Because of the high transition temperature in bulk, however, real-space visualization of this event has remained impossible so far.

6.3   Discussion and outlook

The results presented here, dealing with the mechanical substrate clamping imposed on a structural type of order parameter such as the trimerization, should have relevance for any structurally driven improper ferroelectric, and are not limited to the specific case of $YMnO_3$. In general, however, our results also points to the need for consideration of epitaxially defined constraints, be it mechanical or otherwise, on the leading order parameter of any type of improper ferroelectric, in order to properly predict and understand the manifestation of polarization in the limit of thin films.

For the specific case of the hexagonal manganite films, it is interesting to consider, if this clamping can be circumvented by growth on a substrate whose mechanical properties are compatible with the lattice trimerization. This could, for example, be a non-trimerizing, yet lattice matching material isostructural to the nonpolar phase of the hexagonal manganites, such as $InGaO_3$ [143]. However, the options for lattice-matching substrate materials are limited (as will be further discussed in Ch. 7), and
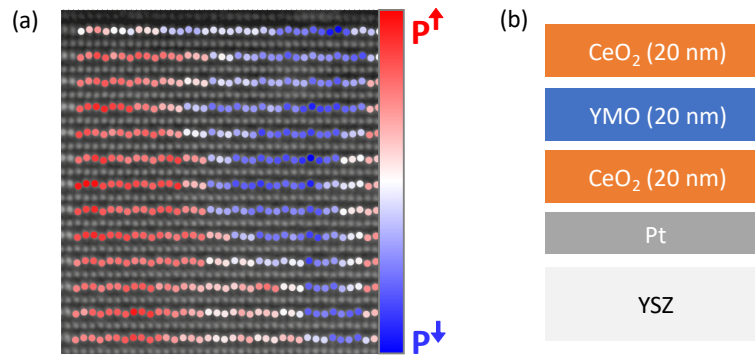
Figure 6.3: (a) STEM image of a YMnO$_3$ film, showing nanoscale domains and absence of polarization at the domain walls. The magnitude of P is inferred from the trimerization amplitude Q. Image courtesy of Marco Campanini and Marta Rossell. (b) Proposed YMnO$_3$-based DE|FE|DE heterostructure for voltage amplification studies.

'clamping-free' growth of the hexagonal manganites has yet to be demonstrated. Even in superlattices between lattice-matching LuFeO$_3$ and LuFe$_2$O$_4$, where the lattice trimerization of LuFeO$_3$ was shown to propagate into the LuFe$_2$O$_4$ layers, a threshold thickness for trimerization was still observed for each LuFeO$_3$ sublayer [144].

Another aspect of the hexagonal manganites that cannot go overlooked is their exotic domains structure and unprecedented domain-wall functionality found in bulk crystals. While the trimerization domain size depends on the cooling rate through the transition temperature in bulk crystals [145], the impact of epitaxial constraints on the domain formation in thin films is not known. Such a study would certainly be an important next step to further understand the physics of the hexagonal manganites under epitaxial confinement. However, the nanometer-sized domains requires atomic-scale characterization by STEM, rendering quantitative investigations challenging. On the other hand, we note that the ISHG characterization presented in this chapter already points to a preferred domain orientation in the films. Indeed, due to the sub-optical-resolution domain size, an equal distribution of polarization domain states should cause complete signal cancellation because of destructive ISHG interference (as described in Ch. 3). In contrast, our ISHG signal persists, and we can thus conclude that there is a predominance of one of the two polarization states. This suggests that the epitaxial constraints of the substrate may indeed have an influence not only on the phase transition temperature, but also on favoring certain trimerization states in h-RMnO$_3$ thin films, further indicating the potential for manipulating their polar properties through epitaxy.

We finally note, that the small domain size observed in the YMnO$_3$ films implies an abundance of domain walls. Here, we propose that a ferroelectric material in such a perpetual multidomain state could find application in the field of negative-

capacitance-driven voltage amplification [146]. This idea is based on the fact that a ferroelectric that is forced to be in a high-energy state corresponding to $\mathbf{P}_S = 0$, such as at a domain wall, is highly susceptible to applied electric fields. Connecting such a material in series with a dielectric in a capacitor can yield a significant voltage amplification equivalent of a 'negative' capacitance. Such an effect has been demonstrated in proper ferroelectric thin films, but it relies on avoiding the single domain state where there are no domain walls. In h-RMnO$_3$ films, the abundance of domain walls guarantees a significant amount of the material to always be in a highly susceptible $\mathbf{P}_S = 0$ state as the polarizaton transitions from up to down across each domain wall (Fig. 6.3(a)). To further explore this idea, the heterostructure shown in Fig. 6.3(b) has been designed and is pending electrical measurements.

Epitaxy of improper ferroelectric h-*R*MnO₃ films

7

As seen in the previous chapter, the epitaxial relationship between the hexagonal RMnO$_3$ film and the substrate all but defines the improper ferroelectric properties of the system. However, to make use of epitaxial constraints as a mode of control of the structurally driven improper polarization in the h-RMnO$_3$ compounds, it is crucial to identify the growth conditions and heterostructure configurations that yield high-quality single crystal h-RMnO$_3$ films. This chapter treats the details of high-quality epitaxy of h-RMnO$_3$ films on different substrates. We find that a an ultraflat substrate surface with step terraces significantly increases the chances of sustaining a 2D growth mode. This yields on the one hand highly oriented smooth films, and on the other hand half-unit-cell precision in film thickness control through RHEED monitoring. We finally identify a route to lattice matching between hexagonal and cubic lattices, opening new opportunities for engineering the improper ferroelectric state through control of epitaxial interfaces.

The results presented in this chapter are found in the attached manuscript:
J. Nordlander, M. D. Rossell, M. Fiebig, M. Trassin. Epitaxial growth of improper ferroelectric h-YMnO$_3$ thin films using surface engineering. *Under submission* (2020).
The manuscript can be found in its entirety in Appendix D.

7.1 Epitaxial growth of h-*R*MnO₃ films on ultraflat surfaces

The progress in studying and controlling the thin-film manifestation of the exotic properties exhibited by the family of hexagonal manganites have been hampered by the difficulty to achieve high-quality epitaxial growth conditions of said material class. A major challenge lies in the identification of commercially available substrates that provide lattice-matching conditions with a hexagonal lattice. Both (001)-oriented hexagonal crystals and (111)-oriented cubic systems exhibit a hexagonal surface symmetry. However, not many substrate materials present an in-plane lattice constant that is compatible with the hexagonal manganites, with an a parameter of
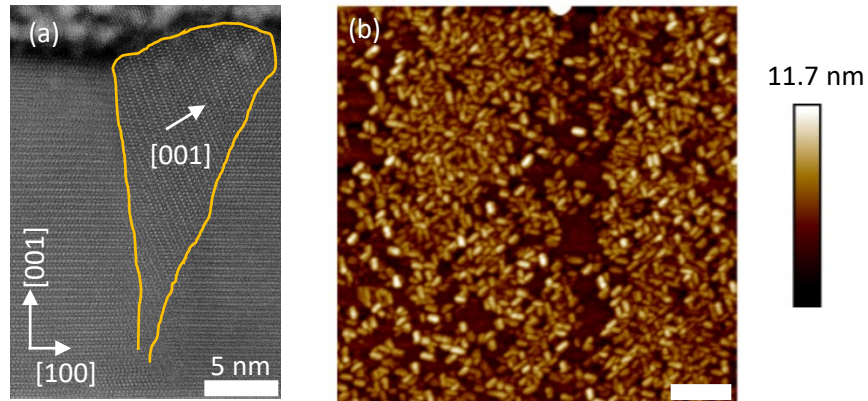
Figure 7.1: Non-optimized growth of h-RMnO$_3$ films often results in inclusions of secondary crystalline orientations compared to the desired c-axis orientation, causing so-called misoriented grains. (a) BF-STEM of such a misoriented grain in YMnO$_3$ grown on YSZ. (b) AFM of YMO thin film surface grown on YSZ. Just as the grains can form inside the film, they can also nucleate on the surface. The scale bar is 200 nm.

about 6.14 Å. The lattices of widely used perovskite-structured substrates such as SrTiO$_3$ are much too small, and tend to coerce the manganites into the orthorhombic phase [147]. The hexagonal phase can however be obtained on (111)-oriented SrTiO$_3$ through a Pt buffer layer [148]. Among the commercially available substrates, fluorite-structured oxides such as YSZ, provide better lattice matching [141, 149, 150]. Yet, studies on the epitaxial growth of h-RMnO$_3$ films on YSZ often report a c-oriented matrix dispersed with misoriented grains [151].

Here, we set out to explore novel routes to achieve improved epitaxy of h-YMnO$_3$ thin films. We find that PLD of YMnO$_3$ directly on as-received YSZ substrates indeed results in such misoriented grains both inside the film and on its surface (Fig. 7.1). While a great reduction of such grains was achieved by lowering the laser fluence for the target ablation, the grains could not be completely eliminated. Instead, we show that the thin-film quality can be greatly improved by substrate surface engineering. By pre-deposition thermal annealing of the YSZ substrates [152], we are able to induce a surface reconstruction resulting in step terraces (Fig. 7.2(a)). We find that YMnO$_3$ growth on this ultraflat surface results in a layer-by-layer growth mode with a significantly smoother thin-film surface than what could be achieved on the as-received substrate (Fig. 7.2(b,c)). We further note that this high-quality growth occurs in spite of the large lattice mismatch between YMnO$_3$ and YSZ, even though we showed earlier [137] that in this case the films form misfit dislocations at the substrate interface rather than being strained to the substrate lattice.

While the YMnO$_3$ growth on annealed YSZ substrates already demonstrates a significant improvement of thin-film quality, there are several reasons for finding a material that can be further lattice-matched to the YMnO$_3$ lattice. From a structural point of view, such lattice matching would allow us to avoid defect formation in the
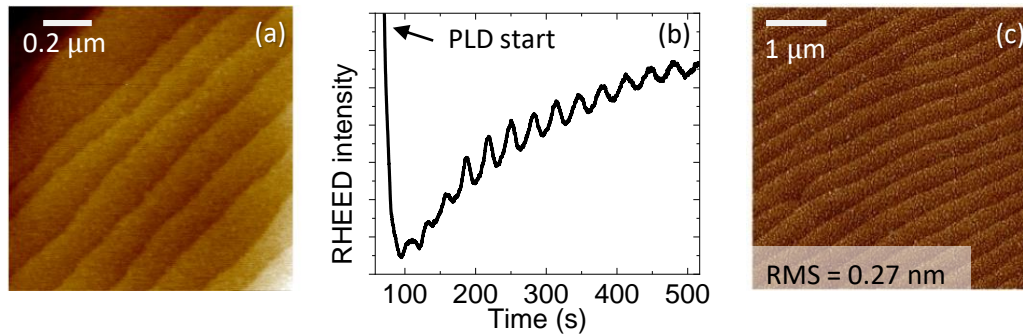
Figure 7.2: (a) AFM topography scan of YSZ substrate after annealing in air at 1250°C for 12 hours. (b) RHEED oscillations during layer-by-layer growth of YMnO$_3$ on the annealed YSZ. (c) AFM topography scan of the deposited YMnO$_3$ thin film.

films from e.g., the misfit dislocations. On the other hand, from a functional point of view, we expect that the improper polarization of YMnO$_3$ is highly susceptible to strain and mechanical boundary conditions in terms of its improper ferroelectric properties. It was already established that YMnO$_3$ did not adopt to the in-plane lattice of YSZ, which would have imposed more than 2% tensile strain in the thin film. Therefore, a smaller lattice mismatch is required in order to strain-engineer the thin film properties. Finally, finding a lattice-matching material for the hexagonal manganites suggests a template for constructing multilayer heterostructures or even superlattices, involving the h-RMnO$_3$ compounds, since this would be a material that could grow epitaxially also on top of the h-RMnO$_3$ films.

We find that indium oxide, In$_2$O$_3$, has excellent lattice matching with YMnO$_3$, and, in the case of tin-doped In$_2$O$_3$ (ITO), it even allows matching the improper ferroelectric with a conducting electrode material. We start by considering the epitaxial growth of ITO films to serve as template for the YMnO$_3$ films. Since ITO has a lattice constant precisely in between that of YSZ and YMnO$_3$, it can be grown directly on YSZ. We find, however, that such growth results in a strained ITO layer that adopts the YSZ in-plane lattice parameter, effectively defeating the purpose of adding this buffer layer. Yet, the ability of ITO to sustain about 1% strain, suggests that this material could also be strained to the in-plane lattice of the hexagonal mangnites. We therefore propose a growth strategy where we insert a 'sacrificial' h-RMnO$_3$ layer between ITO and YSZ. Hence, apart from the conducting properties of ITO, we take advantage of the strain-relaxed nature of the h-RMnO$_3$ films on YSZ to achieve two additional features. First, because the ITO will be strained to the sacrificial layer instead of YSZ, we achieve lattice-matching between ITO and YMnO$_3$Second, while the sacrificial h-RMnO$_3$ layer accommodates the tensile lattice mismatch with respect to YSZ through the formation of local defects (i.e. misfit dislocations), the ITO layer will decouple the sacrificial h-RMnO$_3$ layer from the top YMnO$_3$ film, further increasing the thin film quality.

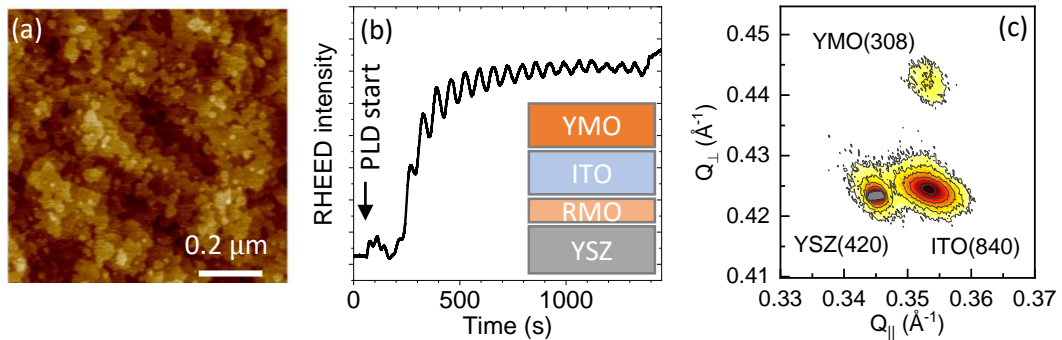Figure 7.3: (a) AFM topography scan of ITO surface when grown on top of an ultrathin sacrificial h-RMnO$_3$ layer (here, h-InMnO$_3$). (b) RHEED oscillations during layer-by-layer growth of YMnO$_3$ on the ITO/h-RMnO$_3$/YSZ stack (see schematic in inset). (c) X-ray RSM of the sample in (b). The h-YMnO$_3$ and ITO films have the matching in-plane lattice spacing, yet neither is strained to the YSZ in-plane lattice parameter.

Following this strategy, we find that upon insertion of the 'sacrificial' h-RMnO$_3$ layer between ITO and YSZ, the ITO adopts to the lattice parameter of this new underlayer, rather than to that of YSZ. This was verified for R=Tb,Y,In in the sacrificial layer. As seen in Fig. 7.3(a), the ITO thin film grown on this sacrificial layer exhibits excellent quality and high surface smoothness. The success of this approach is further confirmed by the layer-by-layer growth mode exhibited by YMnO$_3$ as it is deposited on top of the ultraflat ITO surface (Fig. 7.3(b)), just as was the case for YMnO$_3$ deposition on ultraflat YSZ. Post-growth x-ray characterization reveals that the all the thin-film layers in this heterostructure have the same in-plane lattice constant, yet distinct from the YSZ substrate (Fig. 7.3(c)). Hence, lattice-matching conditions were successfully achieved with RMnO$_3$-buffered ITO as bottom electrode.

We finally note that a layer-by-layer growth mode was also achieved for h-YMnO$_3$ on ultraflat Pt and on CeO$_2$, both grown on YSZ, confirming the importance of an ultraflat substrate for oriented and two-dimensional growth of the hexagonal manganites. Nevertheless, the perfect lattice matching achieved between ITO and YMnO$_3$ renders In$_2$O$_3$-type bufferlayers the most promising candidates for growing and heterostructuring high-quality, epitaxial h-RMnO$_3$ films.

7.2 Discussion and outlook

The growth conditions presented in this work have also been used to grow epitaxial films of hexagonal ErMnO$_3$ and TbMnO$_3$. Because of their compatible in-plane lattices, similar results as for YMnO$_3$ were obtained in both cases. Even growth of hexagonal InMnO$_3$ could be achieved on YSZ, but only for a couple of monolayers as InMnO$_3$ is metastable towards In$_2$O$_3$ with the currently used growth conditions.

The greatly improved growth conditions presented here open up for further studies of the exotic physics of the family of the hexagonal manganites. In particular, the identification of a lattice matching thin-film material, which can also be conducting, suggests on the one hand a route to achieving films with bulk-like properties. This would be interesting not only for further study of the ferroelectric properties of the hexagonal manganites, but also presents an exciting opportunity to explore the low-temperature magnetic order and especially its domain structure, which has so far evaded characterization [153], in these compounds, and potential magnetoelectric coupling effects [104]. On a more applied note, the mutual lattice matching demonstrated here could facilitate the insertion the hexagonal manganites as improper ferroelectric layers in multilayer systems of relevance for ferroelectric device applications [148].

Finally, the exchange of RMnO$_3$ compound in either the sacrificial layer or the ferroelectric, top layer could yield a pathway to tune the improper ferroelectric properties through strain, owing to the different bulk lattice parameters of the different species of the h-RMnO$_3$ family and certainly motivates further studies on the topic.

Inversion-symmetry breaking in layered oxide films

8

So far, we have investigated the polar properties in ultrathin oxide thin films in the form of a ferroelectric state. In those materials, the polarization, and the resulting inversion-symmetry breaking, appears *spontaneously*. In this final chapter, we will explore a different kind of polar state, inherent to sub-unit-cell-layered oxide thin films, where we now break inversion symmetry *deterministically*. Given the prominent standing of a broken inversion symmetry in coercing emergent phenomena in functional materials, such controlled parity engineering in oxide thin films provides a novel route to promote exotic functionality. Here, we use the same layered, hexagonal materials investigated in the previous chapters, but where inversion symmetry used to be broken spontaneously in the improper ferroelectric phase, it is now broken by design in the paraelectric phase. We use ISHG to detect the local, noncentrosymmetric state of individual half-unit-cell layers during h-RMnO$_3$ thin film growth, showing that the global symmetry of the thin-film system alternates between centrosymmetric and noncentrosymmetric states with the deposition of each such sub-unit-cell layer. Precise control of deposition time therefore allows setting the parity of the thin films on demand within an ultrathin thickness range of less than 6 Å. Thus, we reveal layered oxide thin films as a new, so far unexplored, class of materials with great prospects for engineering parity at the nanoscale. The results presented in this chapter are published as [154]:

J. Nordlander, M. D. Rossell, M. Campanini, M. Fiebig, M. Trassin. Inversion-symmetry engineering in sub-unit-cell-layered oxide thin films, arXiv:2005.09083 (2020).

The manuscript can be found in its entirety in Appendix E.

8.1 Local inversion-symmetry breaking in sub-unit-cell-layered oxides

An interesting observation that is not unique to the hexagonal manganites but is valid for many, if not all, naturally layered oxides, is that they tend to grow in blocks of sub-layers rather than by the full unit cell during PLD thin-film synthesis [123,
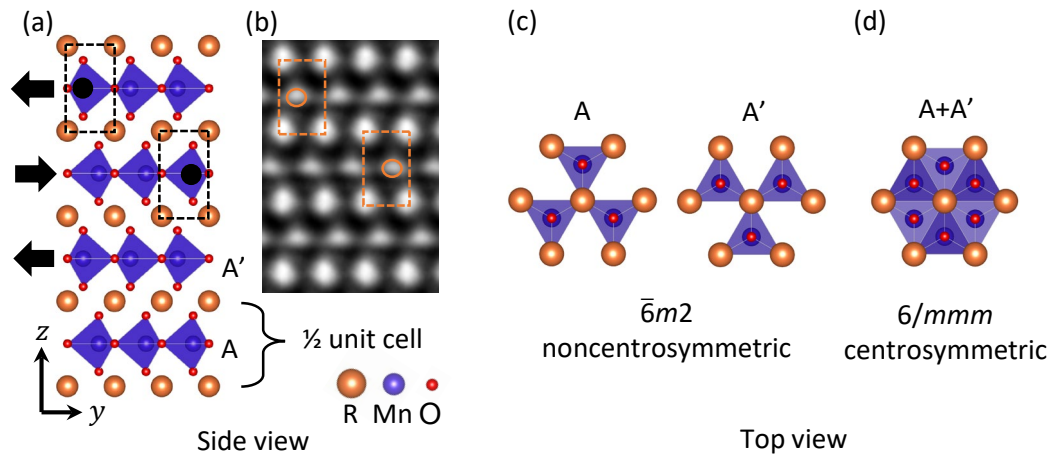
Figure 8.1: Hexagonal $R\text{MnO}_3$ crystal structure in the nonpolar phase. (a) Side view, highlighting the noncentrosymmetry of the individual half-unit-cell layers. (b) Corresponding HAADF-STEM image from a YMnO_3 film. (c) Top view of the crystal structure showing the trigonal symmetry of the half-layers. Note that the two layers, denoted A and A′, exhibit the same structure up to a 60° rotation around the z axis. (d) The combination of the two layers in (c) yields the inversion symmetry of the full unit cell.

155, 156]. In fact, there is no inherent reason for the films to form layers consisting of the full unit cell just because, from a symmetry perspective, that block is the smallest repeating unit. The growth mode is rather decided by surface energy, electrostatics and availability of materials species at each moment of the growth process. In fact, there are other thin-film growth techniques, such as oxide molecular beam epitaxy, where, instead of a stoichiometric composition, only certain atomic species are supplied to the sample surface at a time, such that even nominally non-layered compounds, e.g. the standard perovskite oxides, are grown in sub-unit-cell sequences.

Since symmetries and properties of materials are intimately connected, as discussed in Ch. 1, we consider the case where these sub-unit-cell layers exhibit a lower symmetry than the full unit cell. Then, novel phenomena that are not observed for the parent material can be expected in such sub-unit-cell layers. For example, if inversion symmetry is broken, many technologically relevant properties can emerge, including nonlinear optical responses such as SHG.

In the specific case of hexagonal manganites, as demonstrated in Fig. 8.1, each unit cell consists of two R-ion planes and two MnO_5 planes. During PLD growth of our films we could conclude from the periodicity of RHEED oscillations during layer-by-layer growth in comparison to thickness, that the hexagonal $R\text{MnO}_3$ family grows in layers of one half unit cell at a time, i.e., consisting of only one R plane and one MnO_5 plane. As demonstrated in Ch. 6, the overall symmetry of the $R\text{MnO}_3$ films at the deposition temperature is hexagonal and centrosymmetric; the symmetry-breaking trimerization only sets in during post-deposition cooling. Yet,
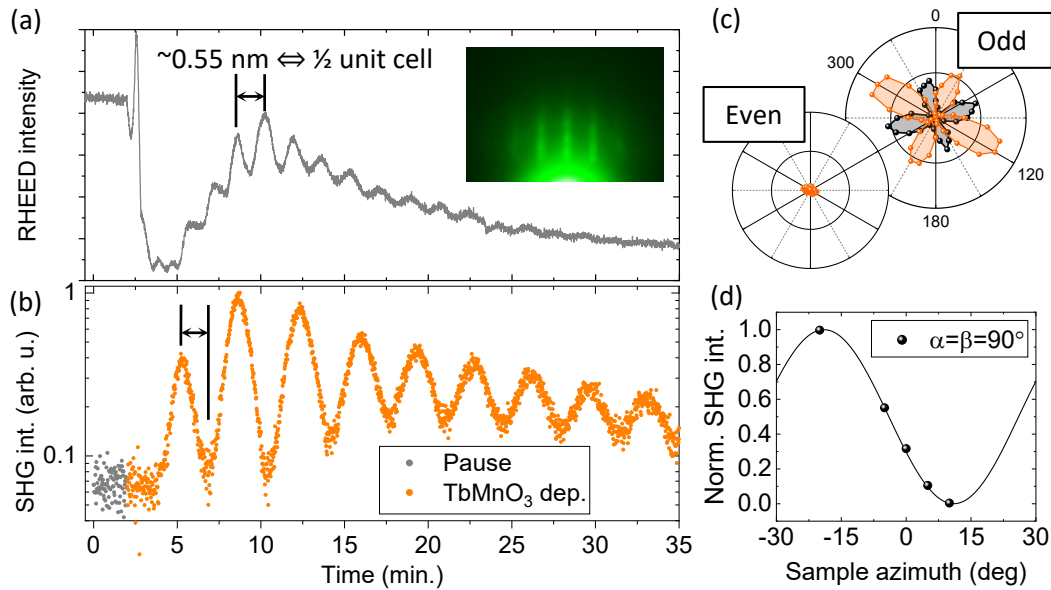
Figure 8.2: (a) RHEED oscillations during growth of hexagonal TbMnO$_3$ correspond to half-unit-cell layers. (b) Simultaneous ISHG monitoring exhibit oscillations but at half the frequency. The even/odd layering of the half-unit-cell layers results in an alternating on/off ISHG signal which reveals a periodic inversion-symmetry breaking. (c) The SHG polarizer scan for odd number of half-unit-cell layers reveals an SHG intensity with a specific symmetry, whereas the even-layered state of the film does not emit SHG at any polarization configuration. (d) The 60° rotational dependence of the SHG symmetry indicates a trigonal system, compatible with the expected half-unit-cell symmetry.

despite this overall inversion-symmetric structure, we note that each half-unit-cell layer is noncentrosymmetric, where two adjoining half-unit-cell layers are identical up to a 60° rotation about the c-axis. The complete unit cell is centrosymmetric, because the first half of the unit cell is the inversion partner of the other half, see Fig. 8.1(c,d).

We can imagine that this local symmetry reduction, which is seen in the individual layers of a layered oxide, can be promoted for an ultrathin film by precise thin-film thickness control. By leaving one half-unit-cell uncomplemented by its mirror layer, the inversion symmetry of the system is broken by design. In particular, the film is then noncentrosymmetric even in the absence of a ferroelectric distortion.

8.2 Deterministic control of inversion-symmetry in ultrathin h-RMnO$_3$

We demonstrate this idea of engineering the symmetry state of a layered oxide by monitoring the ISHG response from uncompensated half-unit-cell layers in h-RMnO$_3$ films during layer-by-layer growth. In this case, the sensitivity of ISHG to

67

broken inversion symmetry of the probed material renders this optical tool perfect for accessing the sub-unit-cell symmetry reduction. While in the previous chapters we have focused on YMnO$_3$, other h-RMnO$_3$ compounds were also grown on YSZ. Here, to demonstrate the generality of our results, we include in our study, apart from YMnO$_3$, both h-ErMnO$_3$ and h-TbMnO$_3$ [1]. In particular, we find that for h-TbMnO$_3$ films up to 20 nm in thickness, no emergence of ferroelectric polarization is observed in the ISHG signal down to room temperature. Therefore, this compound is especially suitable for investigating the symmetry breaking inherent to the half-unit-cell layers, directly excluding ferroelectricity as a contribution to the ISHG response.

The simultaneously monitored RHEED and ISHG intensities during growth of a nonferroelectric hexagonal TbMnO$_3$ film are shown in Fig. 8.2(a,b). Both signals exhibit a periodic modulation of the intensity, where the ISHG response has twice the periodicity of the RHEED oscillations. This means that the periodicity of the ISHG response is one full unit cell and the distance between a maximum and a minimum in the ISHG intensity is equivalent to a half-unit-cell layer in thickness. By ISHG polarimetry, (Fig. 8.2(c,d)), we find that the ISHG signal is consistent with the $\bar{6}m2$ point-group symmetry of the half-unit-cell layers. Importantly, this ISHG signal is only present when there are uncomplemented half-unit-cell layers in the thin film structure. Each point at which the film consists of only complete unit cells (an even number of half-unit-cell layers), inversion symmetry is restored in the system, and the ISHG signal vanishes. For an odd number of half-unit-cell layers, the ISHG signal reflects the breaking of inversion symmetry in the odd half-unit-cell layer. The sub-unit-cell growth mode thus allows setting the symmetry state of the thin film by design.

The lack of inversion symmetry in a half-unit-cell layer can be traced back to the trigonal coordination of MnO$_5$ bipyramids. The sublattice of the R-ions, on the other hand, is hexagonal and perfectly centrosymmetric. Therefore, to unambiguously show that the ISHG response is really related to the symmetry-breaking in the MnO$_5$ planes, we construct a superlattice with alternating Y and Er ions on the R site. As seen in Fig. 8.3, the ISHG oscillations remain coherent during the deposition process and the ISHG amplitude is indeed independent of R species. This observation confirms that the ISHG oscillations are related to the even/odd layering of trigonal MnO$_5$ planes in the RMnO$_3$ films. Through STEM imaging, we can resolve atomically sharp interfaces between the two materials, revealing an exceptional agreement between the layering indicated by ISHG and the distribution of Y and Er layers in the film.

Thus, we are able to detect the alternating symmetry state of the thin-film system, oscillating between centrosymmetric and noncentrosymmetric states, where the inversion symmetry of the system is broken due to uncompensated half-unit-cell

---

[1]While in bulk, TbMnO$_3$ crystallizes in the orthorhombic phase, the hexagonal phase can be achieved in thin film through epitaxial stabilization.
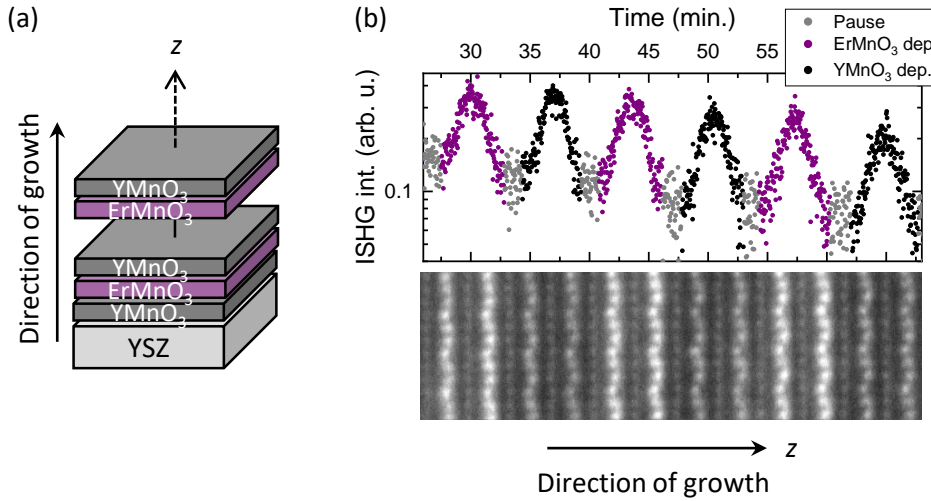
Figure 8.3: (a) Sketch of RMnO$_3$ superlattice combining YMnO$_3$ and ErMnO$_3$. (b) Corresponding ISHG signal and post-deposition HAADF-STEM of a (h-YMnO$_3$)$_1$/(h-ErMnO$_3$)$_1$ superlattice. The heavier Er atoms appear brighter than the Y atoms in the STEM image, which also reveals the lattice trimerization of the film since the imaging is performed at room temperature.

blocks, or, equivalently, for film thicknesses corresponding to an odd number of half-unit-cell layers. The sequencing of these individual half-unit-cell planes during growth enables deterministic control of the symmetry state of the layered films at surfaces and interfaces. We can move from a centrosymmetric to a noncentrosymmetric system within the deposition of a half-unit-cell layer, that is, in less than 6 Å. This control is enabled by the ISHG technique, that perfectly resolves the symmetry evolution of the films in real time and with sub-unit-cell accuracy.

8.3 Discussion and outlook

The results obtained in this work indicate the power of layered oxide materials for engineering emergent properties in the ultrathin regime. Here, we obtained a nonlinear optical response from a material that is expected to be centrosymmetric. However, given the many physical phenomena related to inversion-symmetry breaking and the lack of studies of the properties of sub-unit-cell layers in complex oxides, we can imagine that there is plenty functionality still left unexplored in these systems. These results deal with the sub-unit-cell symmetry breaking in the hexagonal manganites. However, the principle is general and holds for other layered oxide thin films. Indeed, our preliminary results show a similar behavior in the layered Aurivillius compounds and in orthorhombic GaFeO$_3$[2].

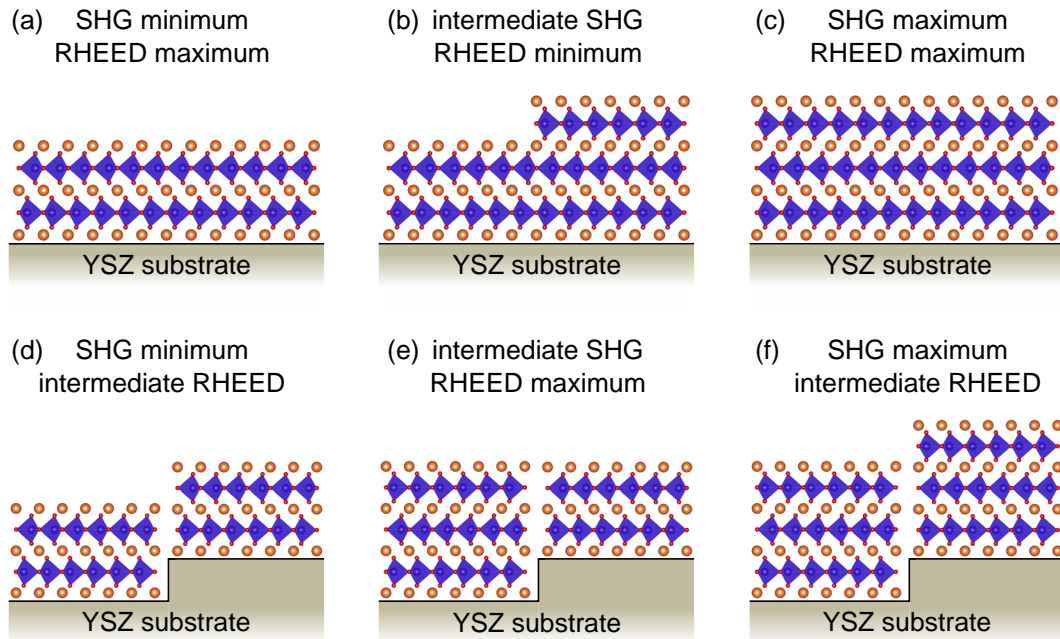[2]J. Nordlander, S. Homkar, M. Fiebig, N. Viart, M. Trassin, in preparation.

Figure 8.4: Idealized schematic illustrating the influence of substrate steps or out-of-phase boundaries on the relative phase between intensity oscillations from ISHG and RHEED. (a-c) In the perfect-interfaces scenario, layer-by-layer growth of the films results in in-phase oscillating ISHG and RHEED intensities, where only the periodicity differs. (d-f) In the presence of discontinuities in the crystal structure, the centrosymmetric state (ISHG minimum) (d) may be reached before the uppermost layer is completed. At a later instance of the deposition, upon top-layer completion (e), RHEED shows a maximum, and only at yet again a later instance does the ISHG reach a maximum (f). Hence, the RHEED and ISHG oscillations decouple and there is a phase shift between the two. We note, however, that this picture is strongly simplified and that in our case, the two-dimensional growth with random island nucleation adds additional complexity.

From a more technical perspective, we note that even though RHEED has similar oscillations but at twice the frequency, this technique cannot replace the ISHG tool for symmetry controlled ultrathin films. This is because of a fundamental difference in what is probed by the two techniques. The RHEED intensity follows the surface morphology. The ISHG intensity is defined by the macroscopic symmetry state of the probed thin-film volume. This difference leads to two distinctions. (1) In case of a less than perfect crystal, the smoothest surface (RHEED maximum) will not necessarily coincide with a maximum or minimum in the SHG signal, that is, the two signals may oscillate out of phase. This concept is illustrated in Fig. 8.4. (2) Even if RHEED happens to follow the symmetry evolution (i.e. RHEED and ISHG oscillations would be in phase), it is not straightforward, based on RHEED alone, to assign which maximum of the oscillations pertain to low symmetry and which pertain to high symmetry. Therefore, only ISHG, which directly accesses the functional property in question, is a reliable indicator based on which the oxide thin

film properties can be predicted.

In this chapter, we put our focus on inversion-symmetry breaking in the paraelectric phase of ultrathin hexagonal manganites. This state can be maintained down to room temperature in h-TbMnO$_3$ or ultrathin h-YMnO$_3$, where the trimerization is suppressed. On the other hand, because of the emergence of improper ferroelectricity at lower temperatures in these very films, we are also presented with an exciting opportunity to investigate the manifestation of the improper polarization state in our h-RMnO$_3$ multilayers. The preservation of the improper ferroelectric state across the interfaces (seen by the corrugation of R-ions along the z axis in Fig. 8.3(b)), even though the ErMnO$_3$ lattice is smaller than the YMnO$_3$ lattice, suggest that the individual RMnO$_3$ layers are coherently strained to each other (this is also confirmed by XRD) and that combining different rare-earth manganites could be an promising approach to strain engineer their properties. An increase the improper ferroelectric transition temperature is indeed observed when combining ErMnO$_3$ with YMnO$_3$: T$_C$ is enhanced from 250 °C in the case of a 10-unit-cell YMnO$_3$ single layer, to 450 °C in a 1.5/1.5 superlattice.

By comparing the ISHG responses related to the half-unit-cell layers and the improper polarization now found in the very same material we can furthermore estimate the magnitude of the emergent half-unit-cell second order nonlinear susceptibility, $\chi^{(2)}_{\mathrm{MnO_5}}$. Comparing the relative ISHG contributions from a paraelectric half-unit-cell layer at the growth temperature (thereby avoiding complicated interference effects from the ferroelectric contribution) with the thickness-normalized ISHG response in the improper ferroelectric (IFEL) phase, we estimate that the respective $\chi^{(2)}$ tensors have a quite similar magnitude at a fundamental wavelength of 860 nm: $|\chi^{(2)}_{\mathrm{MnO_5}}| \sim |\chi^{(2)}_{\mathrm{IFEL}}|$, where $\chi^{(2)}_{\mathrm{MnO_5}}$ could even be up to an order larger. This is an interesting observation, because the nonlinear polar properties originating from the inversion-symmetry breaking of the half-unit-cell layer does not have a threshold thickness, suggesting the possibility to design ultrathin, yet efficient $\chi^{(2)}$ materials. Furthermore, such monolayer functionality is also seen in the field of 2D materials, where the even/odd dependency of the properties on number of monolayers in exfoliated transition-metal dichalcogenides [157–161] is in striking analogy to the case of sub-unit-cell layered oxide seen here, and certainly motivates further investigations into the possibility of emergent physics in these low-dimensional oxide layers.

ISHG is specifically suitable to detect additional functionality that changes the symmetry of these sub-unit-cell layers. This could include changes to atomic coordination, band structure, strain state or stoichiometry. Here, a spectroscopic approach could be enlightening, allowing to couple to specific electronic transitions of the sub-unit-cell layers. Bulk hexagonal manganites are known to host a rich defect chemistry [162, 163]. It would therefore be of interest to investigate if a change in oxygen stoichiometry in the thin films, i.e. a change in coordination of the Mn ions, would indeed reveal itself as a change in the $\chi^{(2)}_{\mathrm{MnO_5}}$-related SHG response.

Conclusions and outlook 9

The work presented in this thesis covers the characterization and control of polar properties in a wide range of oxide thin-film systems, all of which exhibit polar complexity in the ultrathin regime that has evaded detailed study so far. To this point, we have demonstrated the use of laser-optical SHG as a highly sensitive, yet noninvasive, probe to successfully overcome previous experimental limitations. This further let us move beyond traditional polar characterization to even discover emergent symmetry breaking in the ultrathin regime that would likely go overlooked by any other technique. In particular, we have seen that combining this technique with the dynamic environment of thin-film growth or device operation yields unprecedented insight into the formation and evolution of polar states in technologically relevant oxide thin-film materials.

We began by showing in Ch. 4 the effect of a complex ferroelectric domain architecture in $BaTiO_3$ thin films on electric poling in electro-optic device heterostructures integrated on silicon. We found that the intermixing of in-plane- and out-of-plane-oriented polarization domains, due to film–substrate thermal expansion mismatch, results in a characteristic response to electric field application that could not be predicted from standard XRD characterization, nor from predictions based on bulk $BaTiO_3$ poling behavior.

In a next step, we investigated phase coexistence of metastable phases in highly compressive strained $BiFeO_3$ films in Ch. 5. In this epitaxially stabilized system, the polarization was found to emerge in a high-temperature supertetragonal phase that can only be accessed during thin-film growth, lacking both bulk crystal counterpart and room-temperature stability. Strikingly, an exceptional robustness was found for this polar state owing to the epitaxial constraints imposed by the substrate, preventing polarization reversal and suppression.

In the latter half of this thesis, in Chapters 6-8, we explored the thin film manifestation of improper geometric ferroelectricity in the hexagonal manganites. We discovered an unexpected threshold thickness in the ultrathin regime, below which the improper ferroelectric state was suppressed due to mechanical clamping of the primary-order lattice trimerization at the film–substrate interface, significantly altering the temperature and thickness dependence of the spontaneous polarization. We further demonstrated a route to achieve epitaxial growth of these films on

lattice-matched buffer layers, suggesting opportunities for strain engineering of the trimerization as a way to tune improper ferroelectricity and for heterostructuring the films in technologically relevant metal | improper-ferroelectric device architectures. Finally, the ISHG probe allowed us to demonstrate engineering of the symmetry state in these films even in the absence of lattice distortion, which was enabled by the sub-unit-cell growth mode of these layered compounds. We showed that the local inversion-symmetry breaking in the sublayers could be promoted by precise thickness control during thin-film epitaxy. The control of symmetry, serving as a proxy for the control of functionality, at sub-nm film thicknesses is a novel aspect not previously considered for engineering emergent phenomena in layered oxides that is uniquely accessible in epitaxial ultrathin films with finite number of monolayers.

Altogether, the results obtained during this thesis unequivocally demonstrate that the effect of epitaxial constraints all but defines the polar properties of these complex oxide systems, such that extrapolation from bulk crystal properties is no longer an adequate approach to predict their functional responses. This leads on the one hand to new, unexpected challenges in designing polar functionality at the nanoscale, where our expectations often fall short of reality. On the other hand, and infinitely more importantly, oxide thin-film technology clearly presents a playground for discovering emergent physical phenomena that do not have a counterpart in bulk crystals. Indeed, in the last few years of complex oxide research, we have seen a move from the idea of creating a platform for oxide electronics as a parallel to semi-conductor technology, to the idea of designing so-called quantum materials, where the strongly correlated electron system of complex oxides leads to certain effects that can only be fully described by a quantum mechanical approach. In analogy to the rapidly expanding field of 2D materials, the robust and emergent functionality here demonstrated in the ultrathin regime of both $BiFeO_3$ and $RMnO_3$ compounds, even pertaining to individual sub-unit-cell layers, could indicate metastable phases of ultrathin oxides as a so far underexplored platform for low-dimensional phenomena.

In a next step, beyond the fundamental understanding developed within the scope of this work, we expect that the key for controlling the functionality of these oxide thin-film systems, is found in the same epitaxial constraints that we now understand define each thin-film system at the nanoscale. We also note that engineering of the defect chemistry of complex oxides is another promising path for steering their functionality that was however not explored within the scope of this thesis. The dynamic range of growth conditions during state-of-the-art oxide thin-film deposition such as PLD, but also oxide molecular beam epitaxy, presents ample opportunities to explore all of these control parameters in future work. The establishment of in-situ SHG as an indispensable probe of functionalities at the very moment of their creation, as demonstrated throughout this thesis, will greatly benefit and expedite such future explorations. We finally note that a more widespread use of in-situ diagnostic tools for monitoring functional properties during materials synthesis can

help to accelerate the advancement of materials design also beyond the oxide thin film materials presented here. In an ongoing effort to facilitate access to the ISHG tool for non-experts, we are currently developing the system further, to enable table-top use.

Ultimately, the diversity of polar functional states and the next to unlimited control of their formation in thin films opens the doors to a world of opportunities in oxide thin-film engineering for designing new functional materials aiming for both emergent quantum phenomena and technological applications.

Contributions to this thesis

The results presented in this thesis are often based on invaluable collaborative work. In the following, the contributions to the work presented in each chapter, by myself and others, are specified. This work was performed at ETH Zurich, unless otherwise stated. All work was initiated and/or supervised by Manfred Fiebig and Morgan Trassin.

Chapter 4 This work was a collaboration between ETH Zurich, IBM Research and UT Austin. The samples were fabricated and structurally characterized by Jean Fompeyrine, Stefan Abel, Daniele Caimi and Felix Eltes at IBM Research - Zurich. The SHG characterization was performed jointly between Jacob Nürnberg, Gabriele De Luca, Marc Reynaud and myself. The data evaluation and modeling was performed by me.

Chapter 5 All samples were grown by PLD by me and by Aline Maillard under my supervision. The ISHG characterization and data evaluation was performed by me. The (ongoing) DFT calculations are performed by Bastien Grosso and Nicola Spaldin at ETH Zurich.

Chapter 6 PLD growth of the samples was performed by me. The ISHG experiments were performed by me. Structural characterization of the thin-film samples, except for STEM, was performed by me. All STEM analysis including the in-situ heating experiments were performed by Marta Rossell, Marco Campanini and Rolf Erni at Empa. The theoretical calculations were performed by Quintin Meier and Nicola Spaldin at ETH Zurich, and by Andres Cano at CNRS Grenoble.

Chapter 7 All PLD growth optimization, SHG measurements and structural characterization, except STEM, was performed by me. STEM imaging was performed by Marta Rossell at Empa.

Chapter 8 All samples were grown by PLD by me. The ISHG characterization and data evaluation was performed by me. The STEM was performed by Marta Rossell at Empa.

Appendices

Ferroelectric domain architecture and poling of BaTiO$_3$ on Si

A

Reprint: J. Nordlander, F. Eltes, M. Reynaud, J. Nürnberg, G. De Luca, D. Caimi, A. A. Demkov, S. Abel, M. Fiebig, J. Fompeyrine, M. Trassin. Ferroelectric domain architecture and poling of BaTiO$_3$ on Si, *Phys. Rev. Mater.* **4**, 034406 (2020).

Ferroelectric domain architecture and poling of BaTiO$_3$ on Si

J. Nordlander [1,*] F. Eltes [2] M. Reynaud [3] J. Nürnberg,[1] G. De Luca [1,4] D. Caimi,[2]
A. A. Demkov [3] S. Abel,[2] M. Fiebig [1] J. Fompeyrine,[2] and M. Trassin [1,†]

[1]*Department of Materials, ETH Zurich, 8093 Zurich, Switzerland*
[2]*IBM Research–Zurich, 8803 Rüschlikon, Switzerland*
[3]*Department of Physics, The University of Texas at Austin, Austin, Texas 78712, USA*
[4]*Department of Physics, University of Zurich, 8057 Zurich, Switzerland*

We investigate the ferroelectric domain architecture and its *operando* response to an external electric field in BaTiO$_3$-based electro-optic heterostructures integrated on silicon. By noninvasive optical second-harmonic generation, we identify the preexistence of in-plane (*a*-) domains dispersed within a predominantly out-of-plane- (*c*-) oriented matrix. Monitoring the poling behavior of the respective domain populations, we show that the spontaneous polarization of these *a*-domains lack a predominant orientation in the pristine state, yet can be selectively aligned with an in-plane electric field, leaving the *c*-domain population intact. Hence, domain reorientation of a ferroelastic *c*-to-*a* type was directly excluded. Such independent electrical control of ferroelectric *a*-domains in a *c*-oriented BaTiO$_3$ film on silicon is a valuable platform for engineering multidirectional electro-optic functionality in integrated photonic devices.

I. INTRODUCTION

Ferroelectric materials host a range of properties of great technological relevance: their inherent piezoelectric effect motivated their original use as mechanical elements in, e.g., sensors or actuators, and the electric-field controllability of their spontaneous polarization has placed them as key elements for oxide electronics [1,2]. Ferroelectric materials also exhibit characteristic optical properties that extend their device potential to the field of photonics [3–6]. In particular, the pronounced linear electro-optic effect (Pockels effect) exhibited by some ferroelectrics allows energy-efficient control of light propagation through tuning of the refractive index n proportional to an external electric field E^{ext}, that is, $\Delta n_{ij} \propto r_{ijk} E_k^{\text{ext}}$. The Pockels tensor components r_{ijk} parametrize the strength of the effect and relate it to the noncentrosymmetric crystal structure of the material. In ferroelectrics, the electro-optic properties are thus closely connected to their ferroelectric domain configuration, that is, the spatial distribution of the inversion-symmetry-breaking spontaneous polarization.

The many technological prospects of combining such electro-optic ferroelectrics with the established silicon-based electronics platform has been a major driving force for the integration of epitaxial ferroelectric thin films on silicon substrates [7–9]. One of the most prominent ferroelectrics used for this implementation is BaTiO$_3$ (BTO), by virtue of being lead-free in addition to exhibiting exceptionally high Pockels coefficients at typical telecommunication wavelengths, like 1310 and 1550 nm [6]. However, strain relaxation effects accompanying the BTO thin-film growth directly on SrTiO$_3$ (STO)-buffered silicon for electro-optic applications,

excluding the insertion of additional buffer layers [10–12], usually result in a complex domain architecture [13,14]. The spontaneous polarization in BTO films on silicon (BTO | Si) may point along the out-of-plane or either of the two in-plane, principal crystallographic axes. In particular, a mixture of nanoscale domains, each with polarization along one of these three directions, is often observed [15]. The superposition of electro-optic effects specific to each of these domain states in a multidomain sample results in a highly nontrivial electro-optic behavior at the macroscopic level of the device. Hence, characterizing the domain distribution and its response to applied electric fields is crucial for understanding and controlling the optical properties of the ferroelectric layer. This remains challenging, however, in a device heterostructure. So far, probing the polarization state of BTO | Si has mainly been restricted either to invasive characterization such as transmission electron microscopy or to scanning probe techniques [15–18], which are sensitive to surface information only. Direct access to the domain architecture of BTO | Si as it evolves with applied electric fields in the active volume of an electro-optic device requires a simultaneously nondestructive and bulk-sensitive probe technique that, on top of all this, has to be applicable *operando*, that is, during electric-field operation of the device.

Here, we used spatially resolved optical second-harmonic generation (SHG) to characterize the ferroelectric domain distribution noninvasively and throughout the thickness of BTO thin films on silicon. This method allowed us to distinguish between the individual domain states in a multidomain architecture, including, in particular, the detection of disordered as-grown *a*-domains within a *c*-oriented matrix. Monitoring the evolution of *a*- and *c*-domain populations in response to an in-plane electric field in an *operando* approach further allowed us to determine details of the in-plane poling mechanism. We found that the alignment of *a*-domains occurs

purely through in-plane domain reorientation, without any occurrence of ferroelastic *c*- to *a*-domain transformation, so that the *c*-domain population remains intact during the poling.

II. THIN FILM GROWTH AND STRUCTURE

Our electro-optic heterostructure, a 50-nm ferroelectric BTO thin film on STO-buffered (001)-oriented silicon, was grown using molecular beam epitaxy (MBE) as described in Ref. [7]. The orientation of the macroscopic polarization of BTO on STO-buffered silicon is controlled by the thickness-dependent strain relaxation of the BTO layer [14]. The epitaxial relationship between the substrate and the tetragonal BTO thin film was confirmed with x-ray diffraction (Fig. 1). The two *a* axes lie in the plane of the BTO film, [110]$_{\text{BTO}}$ || [100]$_{\text{Si}}$, and the longer (polar) *c* axis of the BTO film is oriented out-of-plane, [001]$_{\text{BTO}}$ || [001]$_{\text{Si}}$. Note that here and in the following, all crystallographic axes refer to this BTO lattice. High resolution $\theta/2\theta$-scans around the out-of-plane and grazing incidence around the in-plane {200}-type BTO reflections are shown in Fig. 1(b). A comparison of the two reflections shows that the average in-plane lattice parameter is shorter than the out-of-plane lattice parameter. In agreement with previous reports [7,15], this indicates that the 50-nm film is mostly *c*-axis-oriented BTO. We note, however, that our peak analysis of the diffraction data is compatible with a small contribution of *a*-oriented domains.

To investigate the influence of an in-plane electric field on the ferroelectric domain distribution in the BTO | Si heterostructure, planar capacitors were fabricated by depositing parallel tungsten electrodes on the BTO thin-film surface. The distance between the electrodes is 5 μm. The in-plane orientation of the electrode gap is varied between devices for testing the effect of in-plane electric fields along [100]$_{\text{BTO}}$, [010]$_{\text{BTO}}$, and [110]$_{\text{BTO}}$. The fabrication process has been described elsewhere [14].

III. EXPERIMENT

We investigated the ferroelectric domain configuration of the BTO film using laser-optical SHG, i.e., frequency doubling of light. This process is parameterized by the material-dependent tensor components of the second-order nonlinear susceptibility, $\chi^{(2)}$. In the electric-dipole approximation, it takes the form

$$P_i(2\omega) = \epsilon_0 \chi^{(2)}_{ijk} E_j(\omega) E_k(\omega). \tag{1}$$

Here $E_{j,k}(\omega)$ are the electric-field components of the incident fundamental beam and $P_i(2\omega)$ denotes the resulting nonlinear polarization in the material which acts as source for the emitted SHG light. Just as for the Pockels effect, the tensor nature of $\chi^{(2)}$ makes the SHG response of a ferroelectric sensitive to the orientation of the inversion-symmetry-breaking spontaneous polarization in the material, and, thus, to its ferroelectric domain state [19,20]. In contrast, scanning probe microscopy (SPM) techniques typically employed to study ferroelectric domain architectures rely on the coupling between the
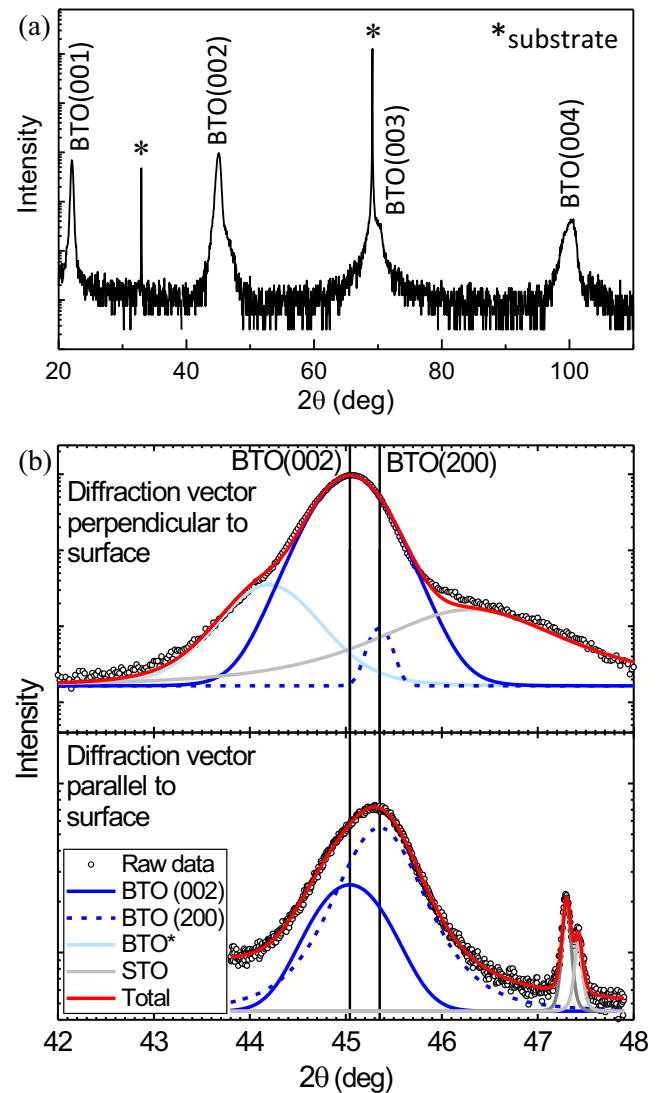

FIG. 1. (a) X-ray-diffraction $\theta/2\theta$ scan revealing a single-phase epitaxial film of tetragonal BTO on Si. (b) High-resolution $\theta/2\theta$ scan around the out-of-plane (top) and grazing incidence scan of the in-plane (bottom) {200}-type BTO reflections. The diffraction profiles are fitted with contributions of both *c*-oriented and *a*-oriented domains. The extracted lattice parameters are $a = 0.3996$ nm and $c = 0.4022$ nm. These values slightly deviate from the bulk parameters, possibly because of tensile strain originating from the difference in the coefficient of thermal expansion between silicon and BTO. The out-of-plane diffraction profile can be fitted with a very small contribution of *a*-domains. For the in-plane diffraction data, the area ratio of the *a*-domain contribution is 30% with respect to the *c*-domains. The difference in *a*-domain contribution between the two measurement configurations suggests that, due to the grazing incidence geometry, the in-plane diffraction profile strongly overestimates the actual volume fraction of *a*-domains predominantly situated close to the surface. The diffraction peak analysis furthermore reveals the convolution of the BTO peaks with the diffraction peaks of the underlying STO buffer as well as the possible presence of a highly compressive strained layer of BTO at the STO interface, labeled BTO*.

polarization state and the piezoelectric response. Hence, while SPM necessitates conducting bottom electrodes for optimal response from surface domain states, SHG has the advantage of being contact-free, yet possessing the bulk sensitivity to address multidomain distributions of polar axes throughout the thickness of the film [21], even during the deposition process [22,23], in absence of electrodes [24], and when this film is integrated into a device architecture [25–27]. For tetragonal BTO, three different crystallographic domains can be defined. These correspond to six polarization states because of the possible ($\pm$)-orientation of the polarization with respect to the long tetragonal axis of each crystallographic domain. Ferroelectric domains whose polarization points along either of the two in-plane crystallographic directions are termed a_1- and a_2-domains whereas out-of-plane-polarized domains are termed c-domains, as defined in Fig. 2(a).

The $\chi^{(2)}$ tensor for tetragonal BTO is defined by its 4mm point-group symmetry [28]. The set of nonzero elements in this point group allows for clear separation of contributions from a_1-, a_2-, and c-domains in an experiment varying the direction of the wave vector of the incident light with respect to the sample orientation as described in detail in Ref. [21]. SHG measurements in normal incidence are only sensitive to a-domain contributions, yielding so-called a-SHG. By tilting the sample, SHG from c-domains (c-SHG) can also contribute to the signal. In thin-film samples, unique a-vs-c selectivity of the SHG response is most conveniently achieved in transmission geometry. However, silicon is a strong absorber in the SHG wavelength range typically employed for probing ferroelectric oxides [20,25], rendering SHG studies of domain distributions in silicon-based thin-film systems scarce. Here, we circumvent the issue of absorption by taking advantage of the near-infrared transparency of silicon and design a transmission experiment with incidence of the fundamental beam at λ_{fund} = 1300 nm onto the back of the silicon wafer [Fig. 2(b)]. Hence, the fundamental light is transmitted through the silicon to the BTO film, letting the SHG light, which would be otherwise absorbed in the substrate, directly exit our heterostructure from the surface of the BTO film.

A Ti:sapphire laser at λ = 800 nm with a pulse width of 120 fs and repetition rate of 1 kHz was converted to λ_{fund} = 1300 nm using an optical parametric amplifier. The $\chi^{(2)}$ components contributing to the SHG signal at λ_{SHG} = 650 nm were evaluated from the dependence of the SHG intensity on the light polarization of incident and detected beams. This so-called SHG anisotropy measurement was performed by rotating the polarization of the fundamental beam by the angle α between $0°$ and $360°$ and detecting the SHG light in parallel configuration under an angle $\beta = \alpha$.

The electric-field dependence of the BTO domain-distribution was investigated by applying square electric field pulses of 50 kV/cm, well above the BTO coercive field [7], for 60 s across the planar electrode pairs on top of the BTO surface. To characterize the BTO domain distribution in just the area where the electric field had been applied, i.e., within the gap between the electrode pairs, we used spatially resolved SHG imaging of the sample as described in Figs. 2(b) and 2(c), with integration times of 2 to 3 min. For domain populations where the individual domains are of suboptical-resolution size (here: $\lesssim 0.7 \mu$m), as is often
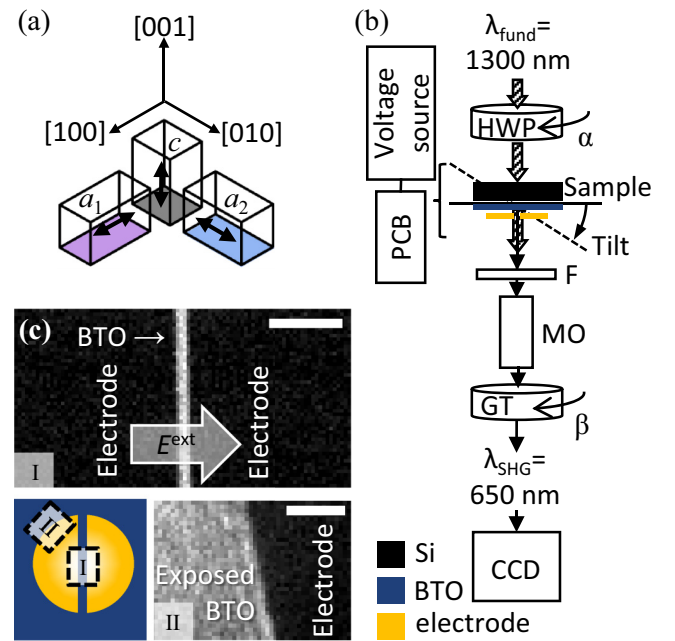

FIG. 2. (a) Schematic showing the relative orientation of a_1-, a_2-, and c-domains. The double-headed arrows indicate the two possible directions for the spontaneous polarization of each crystallographic domain type. (b) Top-view schematic of the experimental setup for SHG imaging in transmission geometry. The light polarization (α) of the fundamental laser beam is then set by a rotatable half-wave plate (HWP). The beam is incident on the back of the Si substrate at the angle of the sample tilt. The SHG signal is separated from the fundamental beam using a bandpass filter (F) and spatially resolved by a microscope objective (MO). The detected SHG polarization (β) is selected by a rotatable Glan-Taylor prism (GT). The resulting SHG image is acquired by a nitrogen-cooled CCD camera. For application of an in-plane electric field to the BTO | Si electro-optic devices, the electrodes are wire-bonded to a printed circuit board (PCB) and connected to a voltage source. (c) SHG images in tilted incidence of the pristine BTO film in the electrode gap (I) and next to the device (II). The corresponding positions are marked in the top-view schematic. The direction of the applied electric field is indicated by the large arrow in (I). The dark regions of the SHG images correspond to areas of the BTO covered by the patterned tungsten electrodes. The scale bars are 20 μm.

the case in thin films, the SHG light from different domain states interferes. SHG waves from domain states with parallel polarization interfere constructively, while antiparallel polarization leads to a $180°$ phase difference between the corresponding SHG contributions so that destructive interference occurs [22,29]. Note that although the domains in our BTO | Si heterostructure are below this resolution limit, we nevertheless obtain information on the overall domain architecture through the characteristic SHG anisotropy yielded by this domain-state interference.

IV. RESULTS

A. Pristine ferroelectric domain architecture

Figure 3(a) shows the SHG anisotropy of the pristine BTO film for normal and tilted incidence. As mentioned, only
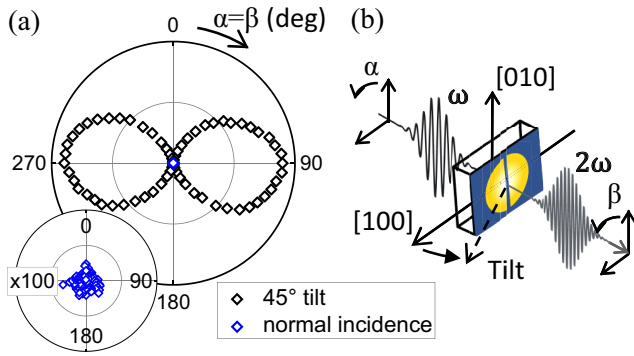
FIG. 3. (a) SHG anisotropy measurement from the pristine BTO film, at 45° sample tilt (black) and in normal incidence (blue), as a function of parallel incident and detected light polarizations, as defined in Sec. III The inset shows a $100\times$ magnification of the SHG anisotropy measurement in normal incidence. The absence of *a*-domain-related *a*-SHG in normal incidence indicates that the nonzero SHG signal in tilted incidence is of pure *c*-SHG type. Hence, only out-of-plane polarized *c*-domains are contributing to the SHG in the pristine state. (b) Schematic of the measurement configuration in (a). For measurements in tilted incidence, the sample is rotated around the vertical axis, corresponding to a projection of the out-of-plane $[001]_{BTO}$-axis onto the horizontal (90°/270°) direction.

a-SHG is allowed in normal incidence. The absence of a SHG signal in this configuration indicates that the nonzero SHG response we obtain in tilted incidence, where *a*- and *c*-SHG are mixed, is of pure *c*-SHG type. Hence, only the ferroelectric polarization of *c*-domains contributes to the net SHG response in the pristine BTO film. The anisotropy of this *c*-SHG signal corresponds to a double lobe pointing along the planar projection of the out-of-plane polar axis (along 90°/270°), which, in the present case, coincides with the horizontal direction of the sample tilt, as defined in Fig. 3(b). Note that the SHG intensity reaches zero for a light polarization perpendicular to the polar axis (0°/180° in Fig. 3), a property we will make use of later on. The SHG anisotropy for the pristine BTO was measured both on the exposed film next to the devices and in the small slit between the electrodes [see Fig. 2(c)]. In both cases, identical SHG polarization anisotropies were obtained with only an overall difference in intensity. This confirms that our SHG probe technique resolves well the small area of BTO serving as active device region.

Even though we observe absence of an *a*-domain contribution in the SHG signal from the as-grown thin film and even though XRD analysis indicates a predominantly *c*-oriented film (Fig. 1), intermixed *a*- and *c*-domains have been previously reported for BTO films as thin as 8 nm on silicon substrates [15]. Our BTO film at 50 nm exceeds this thickness by far. We therefore conclude that the absence of *a*-SHG indicates either (i) a density of *a*-domains below the experimental detection threshold or (ii) complete cancellation of destructively interfering SHG contributions from *a*-domains smaller than the optical resolution limit with equal volume fractions of antiparallel polarization domain states. In the following, we will see that, not only are we able to discriminate between these two cases, but we also provide
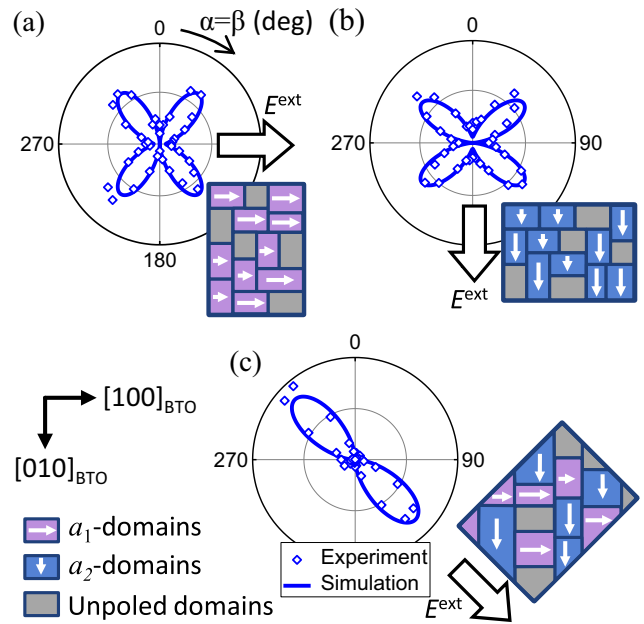

FIG. 4. (a)–(c) SHG anisotropy in normal incidence for the 50-nm BTO film subsequent to in-plane poling along (a) $[100]_{BTO}$, (b) $[010]_{BTO}$, and (c) $[110]_{BTO}$. The solid lines are SHG anisotropy simulations using BTO bulk coefficients of $\chi^{(2)}$ and assuming the domain architecture sketched in the respective insets.

insight into the type of domain reorientation triggered upon electrical poling.

B. Electric poling of *a*-domains

To scrutinize the ferroelectric domain distribution in the 50-nm BTO layer and its response to electrical poling, we used SHG imaging in combination with electric-field application along the plane of the film, as described in Sec. III. Poling was investigated in three device configurations, namely, electric field along $[100]_{BTO}$, $[010]_{BTO}$, and $[110]_{BTO}$. The normal-incidence *a*-SHG anisotropies after in-plane electrical poling are shown for each of these configurations in Figs. 4(a)–4(c). While measurements in the pristine state, as discussed in Sec. IV A, did not yield any *a*-SHG, application of the in-plane electric field led to a remanent *a*-SHG signal in the gap between the electrodes. This signal was more than 30 times larger than the detection threshold of SHG, clearly evidencing electric-field poling of *a*-domains for all device configurations. SHG measurements on BTO films as thin as 26 nm on silicon reveal a similar presence of *a*-SHG that appears only after in-plane electric-field application. We can understand the poling-induced presence of *a*-SHG by comparing the experimental data in Figs. 4(a)–4(c) with SHG anisotropy simulations of different a_1- and a_2-domain configurations using bulk BTO values [30] for the tensor components of $\chi^{(2)}$ in Eq. (1). We find agreement between theory and experiment when assuming that the electric field along $[100]_{BTO}$ only generates a poled a_1-domain population [Fig. 4(a)], whereas the electric field along $[010]_{BTO}$ poles only an a_2-domain population [Fig. 4(b)]. Hence, the two

cases are identical up to a 90° in-plane rotation. With an electric field along $[110]_{BTO}$, equal fractions of the two a-domain types are poled, leading to a fundamental change in the SHG anisotropy [Fig. 4(c)] that corresponds to the coherent superposition of the a_1 and a_2 cases described above. Thus, we see that the in-plane electric field yields a poled a-domain architecture, where the relative field components along the principal crystallographic a axes control the poling ratio of the two in-plane domain variants. To gain a full understanding of the domain dynamics in the system, however, it is necessary to also determine the type of domain architecture in the pristine film that forms the reservoir out of which these a-domains are electrically coerced.

For this purpose, we consider two scenarios for the electric-field alignment of a-domains, following the two cases discussed in Sec. IV A. First we consider a reorientation of c-domains into a-domains in the absence of an as-grown a-domain reservoir to draw from [case (i)]. For example, previous studies have shown c- to a-domain reorientation by electrical poling in both BTO bulk crystals [31] and $Pb(Zr_{0.2}Ti_{0.8})O_3$ (PZT) thin films [32,33]. Alternatively, the generation of a-domains could result from poling of a pre-existing, 1:1 population of oppositely polarized a-domains [case (ii)].

For case (i), the ferroelastic transformation of domains from c- to a-axis orientation would manifest itself as an increase in a-SHG intensity with a corresponding decrease of c-SHG intensity, as the a-domain population would grow at the expense of the c-domain population. For case (ii), on the other hand, the onset of a-SHG from the poling of pre-existing a_1- or a_2-domains would leave the c-SHG contribution constant, as the c-domain population itself would remain unchanged.

C. Electric-field dependence of c-domain population

Independent access to both a- and c-SHG contributions in thin-film ferroelectrics has previously been achieved by performing a set of subsequent measurements in different optical configurations. However, investigation of the actual poling mechanism requires an *operando* approach with simultaneous access to the two SHG contributions during poling within a single experimental setup. In the previous section, all SHG measurements were performed in normal incidence where only a-SHG can contribute to the SHG signal. To allow all SHG contributions, we now turn to a tilted-incidence SHG geometry [Fig. 5(a)]. We used the $[110]_{BTO}$-oriented device for this type of experiment. In contrast to the $[100]_{BTO}$- and $[010]_{BTO}$-oriented device types, here the a-SHG anisotropy exhibits a double-lobe symmetry where the SHG contribution peaks along the electric-field and net-polarization direction but is zero perpendicular to it [see Fig. 4(c)]. Similarly, as seen in Fig. 3, the c-SHG exhibits a double-lobe anisotropy which is maximized along the projection of the out-of-plane polar axis onto the direction of the sample tilt (along 90°/270°), and is zero perpendicular to it. Thus, by tilting the sample and orienting it such that $[110]_{BTO}$ ($||E^{ext}$) is perpendicular to the horizontal sample tilt, a-SHG and c-SHG are polarized orthogonal to each other [see schematic in Fig. 5(b)]. This enables simultaneous and cross-interference-free detection of both contributions.
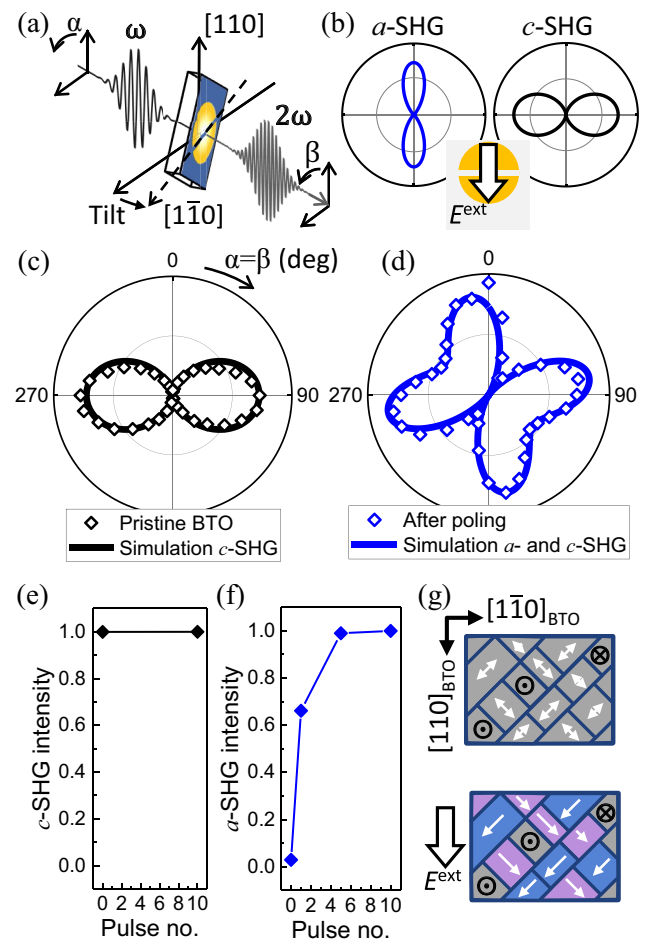

FIG. 5. Independent characterization of a- and c-SHG on BTO thin films in tilted incidence. (a) Schematic of the measurement geometry. (b) Expected a- and c-SHG anisotropies after poling along $[110]_{BTO}$ in the measurement geometry in (a) with a 30° sample tilt. (c), (d) SHG anisotropy before (c) and after (d) in-plane poling of the BTO film. The solid lines show corresponding SHG simulations using bulk values for $\chi^{(2)}$, given the domain architectures sketched in (g). (e), (f) Evolution of the c-SHG (e) and a-SHG (f) intensity as function of the number of applied electric-field pulses (maximum ≡ 1). (g) Sketch of the domain architecture in the pristine BTO film (top) and the same film subsequent to in-plane electrical poling (bottom). Only preexisting a-domains that in the pristine state lack a net polarization direction are poled. The a_1- and a_2-domains are poled in equal fractions, indicated by purple and blue, respectively. The c-domain population remains unchanged during in-plane poling.

In this tilted-incidence configuration, we measured the evolution of the SHG anisotropy [Figs. 5(c) and 5(d)] and SHG intensity [Figs. 5(e) and 5(f)] following the application of consecutive voltage pulses to the $[110]_{BTO}$-oriented device. As noted earlier, only c-SHG is detected for the pristine state before poling [Fig. 5(c)]. Directly after the first voltage pulse, a drastic change in the anisotropy of the SHG signal was observed [Fig. 5(d)]. The a-domain population induced by the poling leads to the onset of a-SHG that appears perpendicular to the c-SHG signal, as detailed above. Given the 30° sample tilt and assuming an initially homogeneously polarized

c-oriented matrix, the SHG simulations [34] provide an estimation of the upper limit for the relative volume fraction of *a*-domains after poling of 34%. Allowing instead a mixed domain configuration rather than a single domain state for the *c*-domain matrix will, however, yield a lower volume fraction of *a*-domains [35], in agreement with the XRD analysis.

Notably, the sudden increase in *a*-SHG was not accompanied by any significant change in the *c*-SHG intensity [Fig. 5(e)]. As seen in Fig. 5(f), the *a*-SHG intensity is fully saturated after five pulses; after applying another five pulses, no further change of either *a*- nor *c*-SHG yields was observed. Furthermore, back switching was not detected; the poled *a*-domain state exhibits long-term remanence.

We recall that a *c*- to *a*-domain reorientation as discussed earlier in case (i) would be expected to lead to a reduction in the *c*-SHG intensity when going from pristine to fully poled state. Clearly, the conservation of the *c*-domain population during in-plane poling in combination with the saturation of the *a*-SHG response is in stark contrast to this scenario and thus excludes such ferroelastic *c*- to *a*-domain reorientation in the BTO heterostructure. Therefore, the reservoir for the poled *a*-domains related to the emerging *a*-SHG signal must be a preexisting *a*-domain population, which in the pristine state consists of equal volume fractions of antiparallel polarization directions, corresponding to case (ii) above and sketched in Fig. 5(g).

V. DISCUSSION

By probing the ferroelectric domain distribution in BTO thin-films integrated on silicon with noninvasive laser-optical SHG, we could clearly distinguish between *c*- and *a*-domain populations and thus monitor their individual response to an external, in-plane-oriented electric field. We characterized this poling behavior directly in the integrated device architecture. The subresolution domain size of the ferroelectric *a*-domain population precluded its detection in the pristine BTO film (a common issue for ultrathin ferroelectric films), yet here we accessed it by aligning the *a*-domains along the in-plane electric field, uncovering a multidomain state for the pristine BTO film. The in-plane electric field acts exclusively on the *a*-domain populations, leaving the *c*-domain population intact for electric fields up to at least 50 kV/cm. We thus excluded the occurrence of (irreversible) ferroelastic *c*- to

a-domain reorientation in the BTO thin films. This stands in contrast to reports on domain reorientation in PZT thin films [32,33] and may be attributed to the stronger coupling between strain and electric dipoles in the BTO thin films compared to PZT, where local rotation of polarization is more frequently observed [36]. We have further shown that the ratio between poled a_1- and a_2-domain populations can be controlled by the choice of in-plane direction of the applied electric field. Conversely, the *c*-domain population can be individually accessed by an out-of-plane oriented field, as has been reported for similar BTO | Si heterostructures even in the absence of a bottom electrode [15]. These nonmixing *a*- and *c*-domain populations that can be individually addressed by the choice of the orientation of the applied electric field thus indicate the possibility of multilevel control of electro-optic response in BTO-based integrated photonic devices. Therefore, we expect our work to stimulate further investigations of oxide heterostructures taking advantage of mixed in-plane and out-of-plane anisotropies.

[1] N. Setter, D. Damjanovic, L. Eng, G. Fox, S. Gevorgian, S. Hong, A. Kingon, H. Kohlstedt, N. Y. Park, G. B. Stephenson, I. Stolitchnov, A. K. Tagantsev, D. V. Taylor, T. Yamada, and S. Streiffer, J. Appl. Phys. **100**, 051606 (2006).

[2] J. F. Scott, Science **315**, 954 (2007).

[3] E. L. Wooten, K. M. Kissa, A. Yi-Yan, E. J. Murphy, D. A. Lafaw, P. F. Hallemeier, D. Maack, D. V. Attanasio, D. J. Fritz, G. J. McBrien, and D. E. Bossi, IEEE J. Sel. Top. Quantum Electron. **6**, 69 (2000).

[4] A. Politi, J. C. Matthews, M. G. Thompson, and J. L. O'Brien, IEEE J. Sel. Top. Quantum Electron. **15**, 1673 (2009).

[5] C. Xiong, W. H. Pernice, J. H. Ngai, J. W. Reiner, D. Kumah, F. J. Walker, C. H. Ahn, and H. X. Tang, Nano Lett. **14**, 1419 (2014).

[6] S. Abel, F. Eltes, J. E. Ortmann, A. Messner, P. Castera, T. Wagner, D. Urbonas, A. Rosa, A. M. Gutierrez, D. Tulli, P. Ma, B. Baeuerle, A. Josten, W. Heni, D. Caimi, L. Czornomaz, A. A. Demkov, J. Leuthold, P. Sanchis, and J. Fompeyrine, Nat. Mater. **18**, 42 (2019).

[7] S. Abel, T. Stöferle, C. Marchiori, C. Rossel, M. D. Rossell, R. Erni, D. Caimi, M. Sousa, A. Chelnokov, B. J. Offrein, and J. Fompeyrine, Nat. Commun. **4**, 1671 (2013).

[8] F. Eltes, C. Mai, D. Caimi, M. Kroh, Y. Popoff, G. Winzer, D. Petousi, S. Lischke, J. E. Ortmann, L. Czornomaz, L. Zimmermann, J. Fompeyrine, and S. Abel, J. Light. Technol. **37**, 1456 (2019).

[9] J. Wang, F. Sciarrino, A. Laing, and M. G. Thompson, Nat. Photonics (2019), doi:10.1038/s41566-019-0532-1.

[10] J. Lyu, I. Fina, R. Solanas, J. Fontcuberta, and F. Sánchez, Sci. Rep. **8**, 495 (2018).

[11] M. Scigaj, C. H. Chao, J. Gázquez, I. Fina, R. Moalla, G. Saint-Girons, M. F. Chisholm, G. Herranz, J. Fontcuberta, R. Bachelet, and F. Sánchez, Appl. Phys. Lett. **109**, 122903 (2016).

[12] M. Scigaj, N. Dix, J. Gázquez, M. Varela, I. Fina, N. Domingo, G. Herranz, V. Skumryev, J. Fontcuberta, and F. Sánchez, Sci. Rep. **6**, 31870 (2016).

[13] Y. L. Li and L. Q. Chen, Appl. Phys. Lett. **88**, 072905 (2006).

[14] K. J. Kormondy, Y. Popoff, M. Sousa, F. Eltes, D. Caimi, M. D. Rossell, M. Fiebig, P. Hoffmann, C. Marchiori, M. Reinke, M. Trassin, A. A. Demkov, J. Fompeyrine, and S. Abel, Nanotechnology **28**, 075706 (2017).

[15] C. Dubourdieu, J. Bruley, T. M. Arruda, A. Posadas, J. Jordan-Sweet, M. M. Frank, E. Cartier, D. J. Frank, S. V. Kalinin, A. A. Demkov, and V. Narayanan, Nat. Nanotechnol. **8**, 748 (2013).

[16] Z. Li, X. Guo, H.-B. Lu, Z. Zhang, D. Song, S. Cheng, M. Bosman, J. Zhu, Z. Dong, and W. Zhu, Adv. Mater. **26**, 7185 (2014).

[17] R. Guo, Z. Wang, S. Zeng, K. Han, L. Huang, D. G. Schlom, T. Venkatesan, Ariando, and J. Chen, Sci. Rep. **5**, 12576 (2015).

[18] S. M. Yang, A. N. Morozovska, R. Kumar, E. A. Eliseev, Y. Cao, L. Mazet, N. Balke, S. Jesse, R. K. Vasudevan, C. Dubourdieu, and S. V. Kalinin, Nat. Phys. **13**, 812 (2017).

[19] M. Fiebig, V. V. Pavlov, and R. V. Pisarev, J. Opt. Soc. Am. B **22**, 96 (2005).

[20] S. A. Denev, T. T. A. Lummen, E. Barnes, A. Kumar, and V. Gopalan, J. Am. Ceram. Soc. **94**, 2699 (2011).

[21] G. De Luca, M. D. Rossell, J. Schaab, N. Viart, M. Fiebig, and M. Trassin, Adv. Mater. **29**, 1605145 (2017).

[22] G. De Luca, N. Strkalj, S. Manz, C. Bouillet, M. Fiebig, and M. Trassin, Nat. Commun. **8**, 1419 (2017).

[23] N. Strkalj, G. De Luca, M. Campanini, S. Pal, J. Schaab, C. Gattinoni, N. A. Spaldin, M. D. Rossell, M. Fiebig, and M. Trassin, Phys. Rev. Lett. **123**, 147601 (2019).

[24] J. Nordlander, M. Campanini, M. D. Rossell, R. P. Erni, Q. N. Meier, A. Cano, N. A. Spaldin, M. Fiebig, and M. Trassin, Nat. Commun. **10**, 5591 (2019).

[25] J. Nordlander, G. De Luca, N. Strkalj, M. Fiebig, and M. Trassin, Appl. Sci. **8**, 570 (2018).

[26] G. De Luca, P. Schoenherr, J. Mendil, D. Meier, M. Fiebig, and M. Trassin, Phys. Rev. Appl. **10**, 054030 (2018).

[27] N. Strkalj, E. Gradauskaite, J. Nordlander, and M. Trassin, Materials **12**, 3108 (2019).

[28] R. R. Birss, *Symmetry and Magnetism*, Vol. 863 (North-Holland Pub. Co., Amsterdam, 1964).

[29] H. Yokota, J. Kaneshiro, and Y. Uesu, Phys. Res. Int. **2012**, 704634 (2012).

[30] Y. Shen, *The Principles of Nonlinear Optics*, Wiley Classics Library (Wiley-Interscience, Hoboken, NJ, 2003).

[31] T. H. E. Lahtinen, K. J. A. Franke, and S. van Dijken, Sci. Rep. **2**, 258 (2012).

[32] A. I. Khan, X. Marti, C. Serrao, R. Ramesh, and S. Salahuddin, Nano Lett. **15**, 2229 (2015).

[33] P. Gao, J. Britson, C. T. Nelson, J. R. Jokisaari, C. Duan, M. Trassin, S.-H. Baek, H. Guo, L. Li, Y. Wang, Y.-H. Chu, A. M. Minor, C.-B. Eom, R. Ramesh, L.-Q. Chen, and X. Pan, Nat. Commun. **5**, 3801 (2014).

[34] Our simulations, using bulk BTO values for $\chi^{(2)}$, indicate relative SHG contributions $a_1 : a_2 : c = 0 : 0 : 1$ before poling, and $a_1 : a_2 : c = 0.255 : 0.255 : 1$ after poling.

[35] The estimated volume fraction of a-domains is relative to the total c-SHG yield. The presence of c-domains of either orientation would reduce the c-SHG yield because of destructive interference between SHG contributions from P_{up} and P_{down}.

[36] B.-K. Lai, I. Ponomareva, I. A. Kornev, L. Bellaiche, and G. J. Salamo, Phys. Rev. B **75**, 085412 (2007).

Emergence of ferroelectricity at the morphotropic phase boundary of ultrathin BiFeO$_3$

<div style="text-align:right">B</div>

Emergence of ferroelectricity at the morphotropic phase boundary of ultrathin BiFeO$_3$

Johanna Nordlander,[*] Aline Maillard, Manfred Fiebig, and Morgan Trassin[†]

Department of Materials, ETH Zurich, CH-8093 Zurich, Switzerland

We demonstrate the robustness of polarization in ultrathin compressive strained BiFeO$_3$ single layers and heterostructures during epitaxial thin-film growth. Using in-situ optical second harmonic generation (ISHG), we explore the emergence of ferroelectric phases at the strain-driven morphotropic phase boundary in the ultrathin regime. We find that the epitaxial films grow in the ferroelectric tetragonal (T-) phase without exhibition of a critical thickness. The robustness of this high-temperature T-phase against depolarizing-field effects is further demonstrated during the growth of capacitor-like (metal | ferroelectric | metal) heterostructures. Using temperature-dependent ISHG post-deposition, we identify the thickness-dependent onset of the monoclinic distortion in the T-matrix and trace the signature of the subsequent emergence of the strain-relaxed rhombohedral-like monoclinic phase. Our results show that strain-driven T-phase stabilization in BiFeO$_3$ yields a prominent candidate material for realizing ultrathin ferroelectric devices.

I. INTRODUCTION

Epitaxial strain engineering in complex-oxide thin films has proven an extremely successful path for designing materials with novel or enhanced functionality.[1] In the case of ferroelectric oxides, epitaxial strain leads to enhanced ordering temperatures, varying domain configurations and even new, metastable phases.[2,3] A prototypical example for the immense impact epitaxial strain can have on ferroelectric properties is seen in BiFeO$_3$ (BFO) thin films. In this system, strain engineering led to the discovery of a strain-driven morphotropic phase boundary with a transition from the bulk-stable rhombohedral-like (R-like) monoclinc phase to a metastable tetragonal-like (T-like) monoclinic phase at compressive strain values exceeding 4%.[4] The epitaxially stabilized T-like phase is in a so-called supertetragonal state with a c/a ratio ~ 1.2 and an unusually large spontaneous polarization of $150\,\mu\text{C/cm}^2$ along the c-axis.[5] Furthermore, because of the flat energy landscape around the morphotropic phase boundary in the phase diagram of BFO, such films tend to relax this strain state with increasing thickness through the formation and coexistence of several metastable monoclinic phases, bridging the transition from T-like to R-like. In this mixed-phase region of the thickness–strain diagram, the system exhibits exceptionally pronounced piezoelectric and ferroelectric response under the application of an electric field.[5,6]

Despite these promising features displayed by highly strained BFO, it is not yet understood how these metastable polar phases behave in the technologically relevant ultrathin regime. Such insight is essential to expedite their device implementation.[7] Since BFO is ferroelectric at the epitaxial growth temperature,[8] it is of particular importance to understand the interplay between strain and depolarizing-field effects on the formation of the ferroelectric state right in the growth environment in both single layers and device-like heterostructures.

Here, we use Ce$_{0.04}$Ca$_{0.96}$MnO$_3$ (CCMO-) buffered, (001)-oriented LaAlO$_3$ (LAO) as substrate (lattice mismatch of about -4.5%) in order to grow epitaxially strained BFO close to the morphotropic phase boundary.[4] We use in-situ optical second harmonic generation (ISHG) during growth to probe the emergence of polarization.[8] At the deposition temperature,

we find that the compressive strain imposed by the substrate results in the epitaxial growth of BFO in a purely tetragonal single-domain state for a thickness of up to at least 80 unit cells. Phase transitions related to the onset of monoclinic distortions are only observed upon sample cooling, where signatures of monoclinic distortion of the T-phase and formation of R-phase are identified at ca. 460°C and 200°C, respectively. We demonstrate zero critical thickness for tetragonal BFO on CCMO-buffered LAO. The single-domain polarization state of tetragonal BFO is preserved during capping with a top electrode in an ultrathin CCMO | BFO | CCMO capacitor heterostructure. The robustness of polarization in the ultrathin regime demonstrated in this work emphasizes the feasibility of supertetragonal BFO as a competitive candidate for ultrathin ferroelectric-based devices.

II. RESULTS

The BFO films are grown by pulsed laser deposition (PLD) on LAO substrates with and without the conducting CCMO buffer layer. The CCMO layer is grown at a substrate temperature of 700°C with an energy fluence of 1.15 J/cm^2 whereas BFO is deposited at 670°C with 1.3 J/cm^2 fluence. Both layers are grown at 0.15 mbar oxygen partial pressure. The CCMO layers are kept at a 15-unit-cell thickness so as to maintain the in-plane lattice parameter of the LAO substrate, i.e., 3.79 Å, whereas the BFO layer thickness is varied from 10 to 80 unit cells. Layer thickness is controlled using in-situ reflection high-energy electron diffraction (RHEED) and post-deposition x-ray reflectivity. Reciprocal space mapping (RSM) by x-ray diffraction is used to characterize the phase and orientation of the thin films.

To probe the emergence of polarization in highly strained BFO, we monitor the ISHG response of the films during deposition in a reflection measurement geometry, as described in Ref. 8. SHG is a symmetry-sensitive nonlinear optical process leading to the emission of frequency-doubled light. This process depends on the point-group symmetry of the material, and is in particular sensitive to the symmetry breaking resulting from the onset or change of spontaneous polarization in a material.[9–11] In the electric-dipole approximation, SHG is

expressed by

$$P_i(2\omega) = \varepsilon_0 \chi_{ijk}^{(2)} E_j(\omega) E_k(\omega), \qquad (1)$$

where the indices i, j, k each take on coordinates x, y and z, P is the generated nonlinear polarization, ε_0 stands for the vacuum permittivity, $E_{j,k}$ are the electric-field components of the incident light and $\chi_{ijk}^{(2)}$ represents the material-dependent tensor components of the second-order susceptibility. The SHG intensity scales with the film thickness t as $I_{SHG} \propto |\chi^{(2)}t|^2$, where, the set of non-zero $\chi^{(2)}$ components is determined by the crystallographic point-group symmetry. In a ferroelectric like BFO, the magnitude of these tensor components is proportional to the spontaneous polarization. We take advantage of this symmetry and polarization sensitivity of SHG to monitor the polar state of the films. SHG has already proven efficient in distinguishing the different polar phases in strained BFO films earlier on.[12-14] By combining the SHG probe with the thin-film deposition process, the in-situ nature of our technique now allows us to directly access the spontaneous polarization in BFO as it evolves during growth and to also follow the temperature-dependent phase transitions BFO experiences during post-deposition sample cooling in the growth chamber.

We first investigate the emergence of polarization in real time during the thin-film growth. Figure 1(a,b) displays the onset of ISHG, and, hence, of a spontaneous polarization, when BFO is deposited on CCMO-buffered LAO. Polarimetry of the ISHG signal [Fig. 1(a)] yields a symmetry compatible with a tetragonal point group with a polar axis normal to the thin-film surface. This observation holds during the growth of all films of this type in the thickness range of up to 80 unit cells investigated by us. In other words, we do not observe a symmetry-changing phase transition during the growth. We therefore postulate that the films are grown in the supertetragonal phase without monoclinic distortions.

Close inspection of the ISHG response at the early growth stages reveals an onset of SHG from the deposition of the very first monolayer. By normalizing the ISHG intensity to the film thickness, we extract the evolution of spontaneous unit-cell polarization of the film, $P_S \propto \chi^{(2)}$,[8] during growth [Fig. 1(b)]. Clearly, the tetragonal BFO grown on CCMO-buffered LAO takes on its polarization from the very first unit-cell layer, remaining constant with increasing thickness. This is noteworthy because the polarization discontinuities at the top and bottom interfaces of a very thin ferroelectric layer leads to a very strong depolarizing field due to incomplete screening of bound charges.[15-17] Consequently, ferroelectrics often exhibit a critical thickness below which the spontaneous polarization is either completely suppressed[15,18] or coerced into a nanoscale multidomain state,[19-21] such that the net polarization is quenched. In particular, R-like BFO has a critical thickness of five unit cells when grown on a conducting buffer, because of the incomplete screening of this depolarizing field.[8] Here, in contrast, we demonstrate a complete absence of critical thickness with an immediate onset of the full polarization in the epitaxially stabilized supertetragonal phase.

To further investigate the apparent robustness of polarization in tetragonal BFO films against depolarizing field effects,
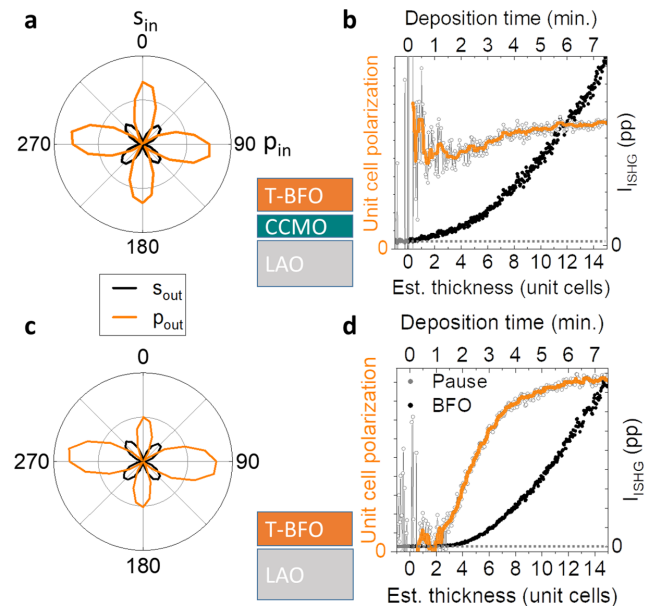

FIG. 1. ISHG measurements during BFO growth. (a,b) For BFO grown on CCMO-buffered LAO. (a) Polarimetry of the ISHG signal from BFO at the growth temperature. The polarization of the incident light is rotated from 0° to 360°, where 0° and 90° correspond to light polarized perpendicular to (s_{in}) and within (p_{in}) the plane of light reflection, respectively. The corresponding intensity of s-polarized (s_{out}) and p-polarized (p_{out}) SHG light is plotted in black and orange, respectively. The symmetry of the ISHG signal is compatible with a tetragonal ferroelectric state, and remains unchanged for film thicknesses up to at least 80 unit cells. (b) The ISHG signal for the $p_{in}-p_{out}$ configuration during growth is shown in black. The dotted line represents the background SHG level. The extracted polarization of the film normalized by the film thickness in unit cells is shown in gray, where a floating average over 20 data points (orange) highlights the onset of the finite polarization directly at the start of the deposition, hence yielding a zero critical thickness. (c,d) For BFO grown directly on LAO. (c) ISHG polarimetry performed as in (a). Similarity to (a) confirms presence of the same type of tetragonal phase. (d) The ISHG response and corresponding polarization acquired as in (a) during growth reveals a 2-unit-cell critical thickness for the spontaneous polarization.

we next compare the emergence of polarization with and without electrical screening at the bottom interface. For this purpose, we keep the growth conditions as before, yet we omit the deposition of the CCMO bottom electrode, growing the BFO film directly on the insulating LAO substrate. In this case, we observe a delayed onset of the ISHG signal, corresponding to a threshold thickness for the emergence of polarization of two unit cells [Fig. 1(c)]. A critical thickness of less than 1 nm in the absence of depolarizing-field screening is a striking confirmation of the exceptional robustness of the polarization state in purely tetragonal BFO. Note that the ISHG polarimetry seen in Fig. 1(d) is identical to the case where BFO is grown on a CCMO buffer [Fig. 1(b)]. This confirms that the films are grown in the same supertetragonal phase in both cases.

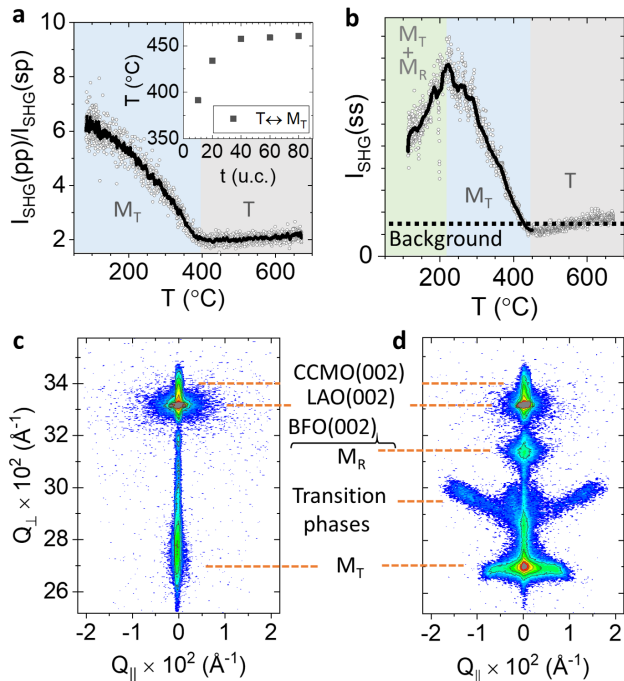The in-plane lattice parameter of 3.79 Å imposed on the

FIG. 2. (a,b) Temperature dependence of the ISHG signal during cooling of the BFO samples after deposition. (a) For a BFO film on CCMO-buffered LAO, a change of relative magnitude of $\chi^{(2)}$ components is observed at 390°C. We assign this change to the onset of monoclinic tilt of the polar axis in the T-phase and hence a phase transition to the M_T phase. As seen in the inset, thicker films on the same substrate exhibit this transition at higher temperatures, saturating around 460°C. (b) For films where our XRD characterization reveals the presence of R-phase, an additional symmetry change can be observed in the s_{in}–s_{out} component around 200°C. This temperature is therefore attributed to the onset of formation of the monoclinic R-phase, here denoted M_R. (c,d) RSM around the (002) reflections of BFO films grown on CCMO-buffered LAO substrates with thicknesses of (c) 10 unit cells and (d) 80 unit cells confirms that the ultrathin films remain in the monoclinic T-phase down to room temperature, whereas strain-relaxation in thicker films promotes phase coexistence of monoclinic phases and inclusions of the R-like phase.

films by the substrates places the BFO close to the morphotropic phase boundary. Hence, whereas at the elevated growth temperature, the purely tetragonal phase of the BFO films prevails, we expect a development of phase coexistence towards room temperature.[4] To follow the temperature-dependent evolution of the polarization in the thin films, we investigate the ISHG response for different film thicknesses during post-deposition cooling of the samples in the growth chamber. Since the onset of a monoclinic distortion corresponds to a reduction of the point-group symmetry from 4mm in the tetragonal phase to m in the monoclinic phases, such transitions are accompanied by new as well as modified components in the $\chi^{(2)}$ tensor. Therefore a corresponding change in the SHG contributions from the BFO film is expected.[12–14]

By tracking different $\chi^{(2)}$ tensor components, we thus identify two transition temperatures (Fig. 2). The first transition is observed in the range of 460°C down to 390°C and the second

transition occurs around 200°C. With the excellent agreement of these transition temperatures with values reported in literature from scanning-probe and x-ray diffraction studies,[22–24] we can assign the high-temperature transition to the point at which the strain-stabilized, purely tetragonal phase develops a monoclinic tilt (here labeled as M_T), see Fig. 2(a). The second transition then represents the formation of monoclinic R-like phase inclusions (here labeled as M_R), leading to a M_R+M_T phase coexistence. The transition to the M_T phase is seen in all films and its transition temperature exhibits a dependence on film thickness, where thinner films exhibit a lower transition point [see inset in Fig. 2(a)]. In contrast, signatures of the low-temperature transition related to the emerge of M_R inclusions are only observed for films with higher thicknesses, where indeed we also see the presence of M_R inclusions at room-temperature by piezo-response force microscopy (not shown) and RSM [Fig. 2(c,d)]. Transition to this state during post-deposition cooling further indicates that R-phase inclusions are absent during the deposition itself so that the films remain coherently strained to the substrate throughout the growth process. It also serves as additional proof that the films are grown in the purely tetragonal phase in absence of monoclinic distortion up to thicknesses of at least 80 unit cells.

Next, we investigate the robustness of polarization in this supertetragonal phase after insertion into a capacitor-like heterostructure. The addition of a capping layer on top of an ultrathin ferroelectric film can often result in effects that are detrimental to an out-of-plane oriented polarization,[15] such as drastically different electrostatic boundary conditions at the new interface. For instance, a transient enhancement of the depolarizing field might emerge during the epitaxial deposition of the top electrode.[21] Such depolarizing-field effects can lead to abrupt domain splitting and a loss of net polarization in the capacitor, even if the ferroelectric layer was initially grown in a single-domain state. Here, we monitor the ISHG response during growth of a 20-unit-cell tetragonal BFO film and the subsequent deposition of a CCMO capping layer, which in total results in a CCMO|BFO|CCMO architecture. As seen in Fig. 3(a,b), the ISHG intensity related to the single-domain polarization in the tetragonal BFO films exhibits a slow, continuous reduction by about 50% during deposition of the CCMO top layer. This decrease cannot be solely attributed to optical losses due to the 5.5 nm thick CCMO layer. It is also incompatible, however, with an immediate quench of net polarization as it is expected for depolarizing-field-induced domain splitting.[21] The unperturbed tetragonal symmetry throughout the growth of the CCMO electrode indicated by the ISHG polarimetry in Fig. 3(a,b) further excludes that nucleation of the R-like phase with its lower spontaneous polarization occurs. We finally note that the onset of monoclinic distortions is only observed when cooling down the sample [Fig. 3(c)]. Post-deposition RSM on films with and without CCMO capping reveals, however, that the electrode deposition results in a reduction of the BFO tetragonality of about 15 %, from 1.20 to 1.17 [Fig. 3(d,e)]. We attribute this decrease in the c lattice parameter to a residual influence of the depolarizing field,[19] causing the polarization reduction in the tetragonal BFO and hence accounting for the reduction of that
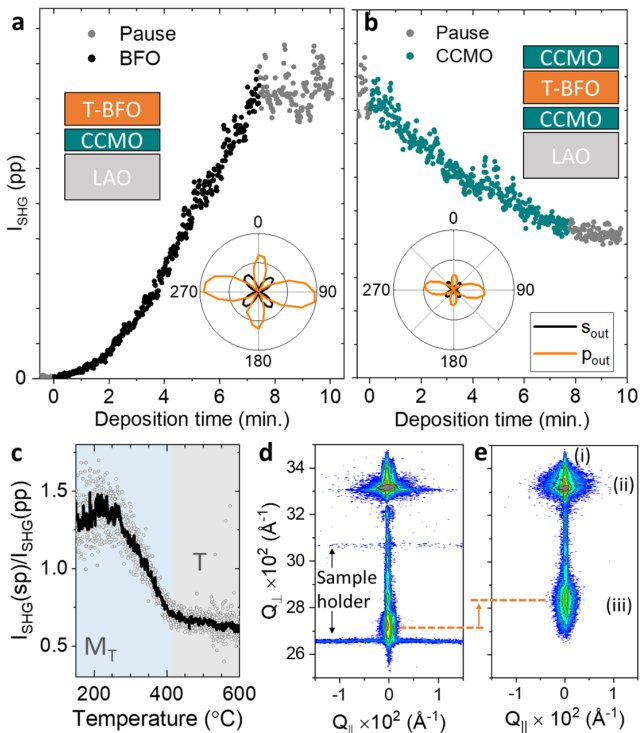
FIG. 3. (a,b) ISHG measurement of polarization in tetragonal BFO during deposition of a multilayer system. (a) Deposition of the first BFO layer on a CCMO buffer yields zero critical thickness and deposition in the tetragonal phase. The film thickness is 20 unit cells. (b) A 15-unit-cell thick CCMO capping layer leads to a gradual reduction in ISHG intensity. The insets show ISHG polarimetry plots subsequent to the respective layer deposition. The films retain their symmetry after CCMO deposition and only an overall reduction in ISHG magnitude is observed. (c) SHG tracking during cooling of the capped BFO sample indicate a shift of the M_T phase transition to slightly lower temperature than in the corresponding uncapped samples. (d,e) RSM of the out-of-plane (002) reflections for a 20-unit-cell BFO on CCMO-buffered LAO, (d) without and (e) with a CCMO top layer. The peaks are labeled as (i) CCMO, (ii) LAO and (iii) BFO. A reduction of the c lattice parameter of BFO of about 2.5% is observed in the film after capping.

part of the ISHG intensity that is not associated to optical loss.

Remarkably, despite the ultrathin thickness of the BFO film, where domain splitting or complete polarization suppression would be expected in the presence of an unscreened depolarizing field, we note that a net polarization remains in the heterostructure.

Preliminary density-functional calculations support the robustness of the high temperature tetragonal phase against polarization suppression and multidomain splitting. We find that the energy cost of polarization reorientation is exceptionally high.[25] The combination of strain and high-temperature stabilization of the supertetragonal phase thus results in a preferred single domain state of our films. Hence, a global reduction of tetragonality, rather than a multidomain breakdown is the more favourable path to reduce the net polarization and, thus, the accumulation of unscreened bound charges at the interfaces. Yet, the high compressive strain imposed by both top and bottom CCMO layers seem to prevent a suppression loss of polarization. This leads to an unusually pronounced polarization at elevated temperature.

III. CONCLUSION

In summary, we have demonstrated an exceptional robustness of polarization in epitaxially stabilized supertetragonal BFO ultrathin films grown on CCMO-buffered LAO. Only upon sample cooling, the monoclinic phase transitions characteristic for the strain-driven morphotropic phase boundary in BFO are observed. We find that the high-temperature tetragonal phase of BFO has zero critical thickness on the conducting buffer layer and grows in a single-domain ferroelectric state. This single-domain state is even preserved under unfavorable electrostatic boundary conditions, such as when the ultrathin tetragonal BFO is incorporated in a heterostructure environment. Strikingly, this system hence displays a polar state that is most robust at the growth temperature, letting it prevail during heterostructure growth, whereas the monoclinic distortions and phase coexistence that facilitate low-energy switching of the ferroelectric state at room temperature conveniently occur post-growth, during cooling of the finalized specimen. Out findings thus proves the great potential of highly compressive strained BFO films for implementation in nanoelectronic devices such as ferroelectric tunnel junctions[7] and ferroelectric field-effect transistors.

* johanna.nordlander@mat.ethz.ch
† morgan.trassin@mat.ethz.ch
[1] R. Ramesh and N. A. Spaldin, Nature Materials **6**, 21 (2007).
[2] D. G. Schlom, L.-Q. Chen, C.-B. Eom, K. M. Rabe, S. K. Streiffer, and J.-M. Triscone, Annual Review of Materials Research **37**, 589 (2007).
[3] A. R. Damodaran, J. C. Agar, S. Pandya, Z. Chen, L. Dedon, R. Xu, B. Apgar, S. Saremi, and L. W. Martin, Journal of Physics: Condensed Matter **28**, 263001 (2016).
[4] R. Zeches, M. Rossell, J. Zhang, A. Hatt, Q. He, C.-H. Yang, A. Kumar, C. Wang, A. Melville, C. Adamo, *et al.*, Science **326**,

977 (2009).
[5] J. Zhang, Q. He, M. Trassin, W. Luo, D. Yi, M. D. Rossell, P. Yu, L. You, C. H. Wang, C. Kuo, *et al.*, Physical Review Letters **107**, 147602 (2011).
[6] P. Sharma, K.-R. Kang, Y.-Y. Liu, B.-K. Jang, J.-Y. Li, C.-H. Yang, and J. Seidel, Nanotechnology **29**, 205703 (2018).
[7] H. Yamada, V. Garcia, S. Fusil, S. Boyn, M. Marinova, A. Gloter, S. Xavier, J. Grollier, E. Jacquet, C. Carrétéro, C. Deranlot, M. Bibes, and A. Barthélémy, ACS Nano **7**, 5385 (2013).
[8] G. De Luca, N. Strkalj, S. Manz, C. Bouillet, M. Fiebig, and M. Trassin, Nature Communications **8**, 1419 (2017).

9 M. Fiebig, V. V. Pavlov, and R. V. Pisarev, Journal of the Optical Society of America B **22**, 96 (2005).

10 S. A. Denev, T. T. A. Lummen, E. Barnes, A. Kumar, and V. Gopalan, Journal of the American Ceramic Society **94**, 2699 (2011).

11 J. Nordlander, G. De Luca, N. Strkalj, M. Fiebig, and M. Trassin, Applied Sciences **8**, 570 (2018).

12 A. Kumar, S. Denev, R. J. Zeches, E. Vlahos, N. J. Podraza, A. Melville, D. G. Schlom, R. Ramesh, and V. Gopalan, Applied Physics Letters **97**, 112903 (2010).

13 R. C. Haislmaier, N. J. Podraza, S. Denev, A. Melville, D. G. Schlom, and V. Gopalan, Applied Physics Letters **103**, 031906 (2013).

14 M. Trassin, G. D. Luca, S. Manz, and M. Fiebig, Advanced Materials **27**, 4871 (2015).

15 J. Junquera and P. Ghosez, Nature **422**, 506 (2003).

16 A. K. Tagantsev and G. Gerra, Journal of Applied Physics **100**, 051607 (2006).

17 C.-L. Jia, V. Nagarajan, J.-Q. He, L. Houben, T. Zhao, R. Ramesh, K. Urban, and R. Waser, Nature Materials **6**, 64 (2007).

18 D. D. Fong, G. B. Stephenson, S. K. Streiffer, J. A. Eastman, O. Auciello, P. H. Fuoss, and C. Thompson, Science **304**, 1650 (2004).

19 C. Lichtensteiger, J.-M. Triscone, J. Junquera, and P. Ghosez, Physical Review Letters **94**, 047603 (2005).

20 C. Lichtensteiger, M. Dawber, N. Stucki, J.-M. Triscone, J. Hoffman, J.-B. Yau, C. H. Ahn, L. Despont, and P. Aebi, Applied Physics Letters **90**, 052907 (2007).

21 N. Strkalj, G. De Luca, M. Campanini, S. Pal, J. Schaab, C. Gattinoni, N. A. Spaldin, M. D. Rossell, M. Fiebig, and M. Trassin, Physical Review Letters **123**, 147601 (2019).

22 H.-J. Liu, C.-W. Liang, W.-I. Liang, H.-J. Chen, J.-C. Yang, C.-Y. Peng, G.-F. Wang, F.-N. Chu, Y.-C. Chen, H.-Y. Lee, L. Chang, S.-J. Lin, and Y.-H. Chu, Physical Review B **85**, 014104 (2012).

23 A. R. Damodaran, S. Lee, J. Karthik, S. MacLaren, and L. W. Martin, Physical Review B **85**, 024113 (2012).

24 C. Beekman, W. Siemons, T. Z. Ward, M. Chi, J. Howe, M. D. Biegalski, N. Balke, P. Maksymovych, A. K. Farrar, J. B. Romero, P. Gao, X. Q. Pan, D. A. Tenne, and H. M. Christen, Advanced Materials **25**, 5561 (2013).

25 B. F. Grosso, N. A. Spaldin, in preparation.

The ultrathin limit of improper ferroelectricity

<div style="text-align:right;">**C**</div>

Supplementary information is available online: Online Supplementary Information

ARTICLE

The ultrathin limit of improper ferroelectricity

J. Nordlander [1,4]*, M. Campanini [2,4], M.D. Rossell [2], R. Erni [2], Q.N. Meier [1], A. Cano [1,3], N.A. Spaldin [1], M. Fiebig [1] & M. Trassin [1]*

The secondary nature of polarization in improper ferroelectrics promotes functional properties beyond those of conventional ferroelectrics. In technologically relevant ultrathin films, however, the improper ferroelectric behavior remains largely unexplored. Here, we probe the emergence of the coupled improper polarization and primary distortive order parameter in thin films of hexagonal $YMnO_3$. Combining state-of-the-art in situ characterization techniques separately addressing the improper ferroelectric state and its distortive driving force, we reveal a pronounced thickness dependence of the improper polarization, which we show to originate from the strong modification of the primary order at epitaxial interfaces. Nanoscale confinement effects on the primary order parameter reduce the temperature of the phase transition, which we exploit to visualize its order-disorder character with atomic resolution. Our results advance the understanding of the evolution of improper ferroelectricity within the confinement of ultrathin films, which is essential for their successful implementation in nanoscale applications.

[1] Department of Materials, ETH Zurich, 8093 Zurich, Switzerland. [2] Electron Microscopy Center, Empa, 8600 Dübendorf, Switzerland. [3] Institut Néel, CNRS, 38042 Grenoble, France. [4] These authors contributed equally: J. Nordlander, M. Campanini. *email: johanna.nordlander@mat.ethz.ch; morgan.trassin@mat.ethz.ch

In improper ferroelectrics, the polarization emerges through a coupling to another, leading order parameter, such as a non-ferroelectric crystal-lattice distortion, charge ordering, or certain spin arrangements[1,2]. The leading order can thus coerce the improper polarization into states that would be avoided in conventional ferroelectrics, allowing the emergence of exotic functional properties to complement those of conventional ferroelectrics, an issue of great interest for the development of next-generation oxide-based electronics[3–5]. In particular, improper ferroelectricity offers routes to achieving the coveted coexistence between electric and magnetic order[6–9]. Furthermore, unlike the polarization in thin proper ferroelectric layers, improper ferroelectricity is expected to exhibit a robustness against typical depolarizing-field effects, such as a critical thickness for spontaneous polarization[10–12]. All this makes improper ferroelectrics a class of materials of great interest, both for the fundamental understanding of complex ferroic order, as well as for their nanotechnological potential. Despite intense investigations of bulk improper ferroelectrics, however, it remains essentially unknown how their extraordinary properties transfer towards the technologically crucial limit of ultrathin films.

Among the different types of improper ferroelectricity, the hexagonal manganites are generally considered as a prototypical family of improper ferroelectrics with hexagonal YMnO$_3$ being particularly well-studied. In this model material, the ferroelectric order is geometrically driven[13,14]. A leading-order structural trimerization of the lattice, described by a two-component order-parameter $\mathbf{Q}$, parametrized by an amplitude Q and a phase φ[15], lowers the YMnO$_3$ symmetry from the centrosymmetric $P6_3/mmc$ to the non-centrosymmetric $P6_3cm$ space group (see Fig. 1a). As a secondary order parameter, the spontaneous polarization $\mathbf{P}_s$ emerges through its coupling to the leading-order parameter $\mathbf{Q}$. The improper nature of $\mathbf{P}_s$ is key to the observed topologically protected ferroelectric domain-vortex pattern[16,17], ferroelectric domain walls with tunable conductance[18–20], and coexistence with magnetic order[2].

However, the elevated ferroelectric transition temperature in bulk hexagonal manganites ($T_C^{bulk} = 1259$ K for bulk YMnO$_3$[21]) imposes major experimental requirements on the probing of the emerging improper polarization, and direct observation and comparison of the two order parameters at the phase transition point has remained elusive. In the ultrathin thickness regime, the challenge in characterizing the emergence of the improper polar state lies foremost in the difficulty in achieving epitaxial, single-crystal growth conditions from the first monolayer on appropriate substrates[22–24]. In earlier studies, analysis of the improper ferroelectric polarization was mainly limited to macroscopic, electrical measurements on films ≥100 nm[25,26]. There have been a few studies of the ultrathin regime, studying either the polarization[27,28], or the lattice trimerization[29–31]. The microscopic interplay between the order parameters, however, and the consequences of their leading or secondary relation in the thin-film limit has to date not been explored. Hence, the consequences of finite thickness and the presence of hetero-interfaces on the improper polarization and its relation to the primary order-parameter are unclear.

Here, we probe the improper ferroelectric state in hexagonal YMnO$_3$ thin films using a combination of two in situ probe techniques. Laser-optical second harmonic generation (SHG) with in situ monitoring of the thin films in the growth environment[32,33] accesses the polarization, while high-resolution scanning transmission electron microscopy (STEM) with in situ heating of the thin-film samples independently measures the trimerization. Density-functional calculations based on the thin-film geometry help interpret the experimental results. We show that the substrate exerts a clamping of the YMnO$_3$ unit cell at
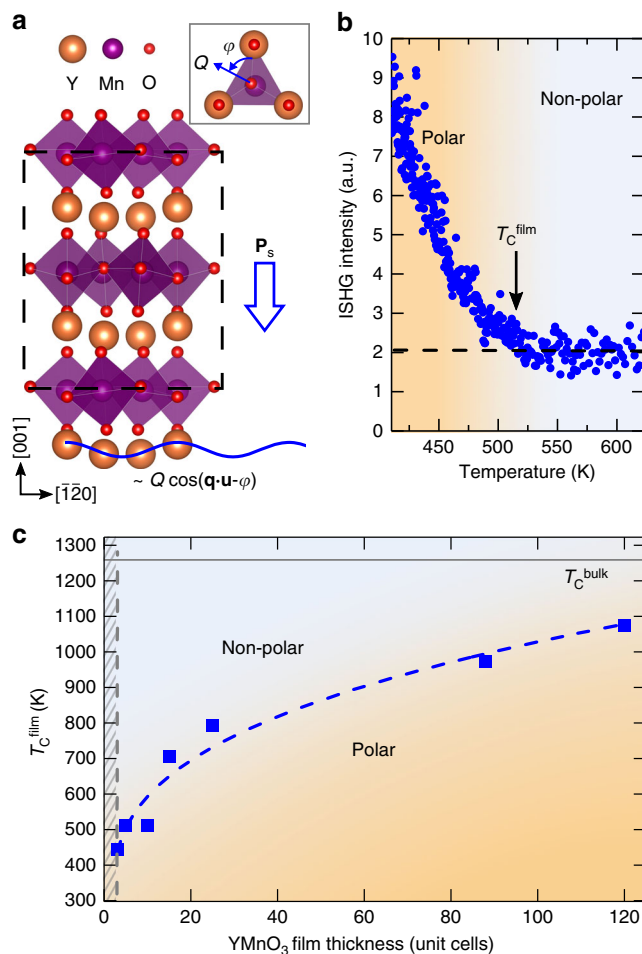

Fig. 1 Evolution of improper polarization in YMnO$_3$ thin films. **a** Schematic of the ferroelectric $P6_3cm$ YMnO$_3$ crystal structure. The lattice trimerization $\mathbf{Q}$ is given by the tilt amplitude Q and azimuthal tilt angle φ of the MnO$_5$ bipyramid (as defined in the inset viewed along [001]), and equivalently by the sinusoidal corrugation pattern of Y atoms. The dashed line outlines the YMnO$_3$ unit cell. **b** Temperature dependence of the ISHG intensity from a 10-unit-cell YMnO$_3$ film grown on YSZ upon cooling in the thin-film growth environment. The dashed line indicates the background level caused by surface contributions. The onset of $\mathbf{P}_s$ at the ferroelectric critical temperature T_C^{film} (indicated by the arrow) breaks inversion symmetry, giving rise to an ISHG wave with an amplitude proportional to $\mathbf{P}_s$. **c** Ferroelectric transition temperatures for different YMnO$_3$ film thicknesses. T_C^{film} is extracted from ISHG measurements as in **a**. Films below three unit cells show no spontaneous polarization down to room temperature, indicated by the hatched gray area. Note that the thin-film crystalline quality could be maintained up to a thickness of 120 unit cells (<140 nm). Within this investigated range, $T_C^{bulk} = 1259$ K (gray horizontal line) has not yet been reached. The dashed line, serving as a guide to the eye, highlights the thickness trend.

the thin-film interface which affects the build-up of the primary-order trimerization and leads to a strong thickness dependence of the improper polarization. By real-space visualization, we reveal an order–disorder type for the structural phase transition driving the emergence of polarization. Our results thus identify the dominant mechanisms steering the polarization in YMnO$_3$ thin films and indicate the prospects of controlling the ultrathin regime of improper ferroelectricity in general by acting on its nonpolar primary order parameter rather than on the polarization itself.

Results

Emergence of improper polarization in the ultrathin regime.
$YMnO_3$ thin films are grown by pulsed laser deposition in the thickness range of 1–120 unit cells on (111)-oriented yttria-stabilized zirconia (YSZ) providing strain-relaxed epitaxial films (Supplementary Figs. 1 and 2). We achieve real-time film thickness control with sub-unit-cell precision through the use of in situ reflection high energy electron diffraction (RHEED) during the thin-film deposition. To detect the ferroelectric order in the samples, we use in situ SHG (ISHG) implemented in the growth chamber. This light-frequency-doubling process is sensitive to the breaking of inversion symmetry so that the amplitude of the ISHG light wave is proportional to P_s[34,35]. ISHG thus has the advantage of being a nondestructive, contact-free probe of the pristine polar state (which distinguishes it from, e.g., scanning-probe techniques) over a large range of temperatures directly in the thin-film growth environment.

For each $YMnO_3$ thin film, we extract the ferroelectric transition temperature (T_C^{film}) from the temperature-dependent onset of ISHG intensity measured during cooling from $T_{growth} = 1070$ K to room temperature (Fig. 1b, Supplementary Fig. 3 and Supplementary Note 1). The dependence of T_C^{film} on the film thickness is shown in Fig. 1c. In all films, we observe ferroelectric phase transitions that are shifted to temperatures much lower than T_C^{bulk}. Even at 120 unit cells thickness, T_C^{film} and T_C^{bulk} differ by more than 100 K. T_C^{film} decreases smoothly with $YMnO_3$ film thickness and at room temperature, P_s reaches zero for the two-unit-cell film, thus establishing a threshold thickness for room-temperature ferroelectricity. To our knowledge, this is the lowest thickness for which an improper ferroelectric polarization in $YMnO_3$ films has so far been stabilized.

These observations are reminiscent of depolarizing-field effects in conventional ferroelectric thin films[36]. In improper ferroelectrics, just as in conventional ferroelectrics, the spontaneous polarization P_s results in the build-up of a depolarizing field. However, the antagonism between P_s and the resulting depolarization field is shifted in favor of P_s, because P_s is induced, and thus stabilized, by the primary order parameter, in this case the trimerization parameter Q. Since this leading-order parameter does not have a polarization, it is not strongly influenced by the electrostatics of the heterostructure. Therefore, while the depolarizing field is present, it is typically less effective in improper ferroelectrics, only supporting a possible small attenuation of P_s but not causing a critical thickness[11,12]. In the $YMnO_3$ films we do observe a threshold thickness, however. This suggests two possible explanations. Either, the order parameters Q and P_s decouple in the thin-film limit and the polarization becomes proper and increasingly susceptible to the depolarizing field after all. Note that even for bulk crystals, a decoupling of Q and P_s was originally considered likely[13]. Alternatively, Q and P_s remain coupled and some other, yet unidentified mechanism is responsible for the suppression of P_s in the first two-unit cells of the $YMnO_3$ thin films.

Direct access to the lattice trimerization. To clarify the relation between the polarization P_s and the crystal-lattice trimerization Q as the primary order parameter, independent access to the latter is required. We map this structural distortion in real-space using high-angle annular dark field (HAADF) STEM at atomic resolution, as a 10-unit-cell-thick sample is heated in situ. In the ferroelectric $P6_3cm$ phase of $YMnO_3$, the trimerized lattice is recognized by its characteristic Q-related "up–up–down" displacement pattern of Y atoms parallel to [001] (see Fig. 1a), seen along the [100] zone axis (see Supplementary Note 2 and ref. 37). This corrugation of Y atoms constitutes a direct measurement of

the leading-order-parameter Q[37]. The behavior of the primary order parameter with temperature can thus be directly visualized. Temperature-dependent fits of Q, shown in Fig. 2, reveal the gradual decrease of the lattice trimerization amplitude with increasing temperature (see also Supplementary Fig. 4). Comparing the temperature dependence of Q with the corresponding evolution of P_s from ISHG (see Fig. 1b) in the thin film, we see that the temperature T_Q at which Q reaches zero coincides with its ferroelectric transition temperature T_C^{film}, and hence the two order parameters emerge at a single transition point.

A similar experimental agreement is found between the observation of a threshold thickness for P_s (two-unit cells) and a suppression of Q close to the film-substrate interface. Figure 3a depicts the averaged displacement $|\langle Q \rangle|$ as a function of the distance from the substrate interface in Fig. 2a. Indeed, we see a complete quench of $|\langle Q \rangle|$ in the initial atomic layer, followed by a continuous increase over the first two-unit cells away from the interface, saturating at a bulk displacement of ~30 pm.

Based on these two observations, we conclude that we can relate the non-bulk-like value of T_C^{film} and the threshold thickness of P_s (measured by ISHG) to the corresponding non-bulk-like value of T_Q and the thickness evolution of the primary order parameter Q (measured by STEM). In other words, we conclude that the improper relation between P_s and Q in the bulk[21] is preserved down to the ultrathin limit, where the behavior of P_s in the thin films is directly guided by the primary structural order parameter Q and any mechanism acting on it. In particular, depolarizing-field effects causing the behavior of P_s to deviate from that of Q, are not observed[11]. This is further corroborated by the observation of similar multidomain structures in the films independent of the charge-screening efficiency of the substrate, see Supplementary Fig. 5.

Impact of epitaxial interface on trimerization. Next, we use density-functional calculations to determine the mechanism for the thickness-dependent reduction of the transition temperature. Since our $YMnO_3$ thin films are strain-free on YSZ substrates (as mentioned, they retain bulk-lattice parameters, see Supplementary Figs. 1 and 2), we exclude relaxation of epitaxial strain as the mechanism, and instead investigate the effect of mechanical clamping at the film-substrate interface on the lattice trimerization. We use density-functional theory (DFT) to calculate the magnitude of lattice distortion across a four-unit-cell film, modeling the interface with the substrate as a clamped, non-trimerized unit cell, with the termination at the surface of the $YMnO_3$ film left free (see "Density-functional calculations" in Methods). We find, that such clamping results in a progressive suppression of the trimerization Q toward the interface with the substrate (Fig. 3b). This is consistent with the experimental data in Fig. 3a and explains the absence of P_s at room-temperature in the ultrathin regime, i.e., the presence of a threshold thickness.

Although suppression of the trimerization because of substrate clamping is expected to lead to a lowering of the transition temperature, such a clamping effect cannot fully account for the reduction of T_C^{film} toward higher film thickness. We propose an additional thickness-related factor to explain this behavior, namely an increase in critical fluctuations of the order parameter as the system approaches the 2D limit. While such fluctuations also occur in conventional ferroelectrics, they are more likely to dominate in improper ferroelectrics, because the primary order parameter is not affected by the depolarizing field. Our preliminary calculations, considering critical fluctuations and using the Landau parameters determined from density-functional calculations[38], are compatible with the observed scaling and the shift of T_C^{film}.
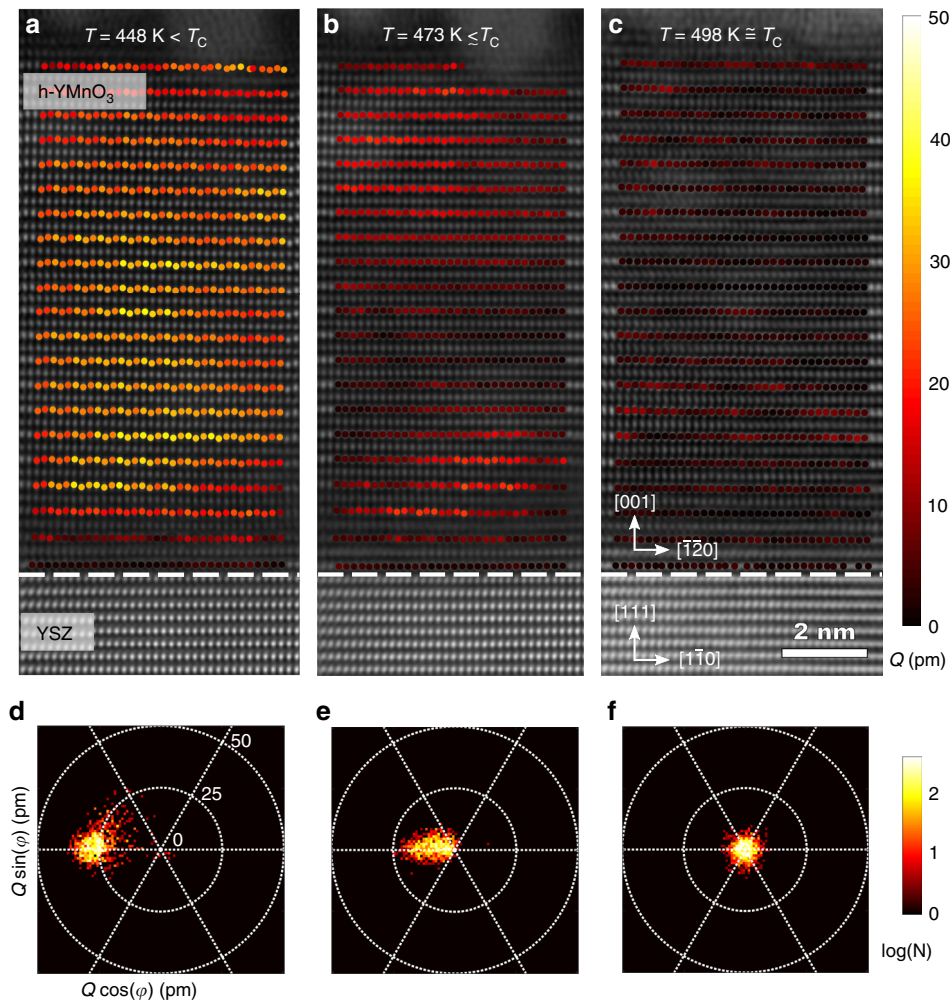
Fig. 2 Real-space visualization of the lattice trimerization amplitude Q across the ferroelectric phase transition. **a–c** HAADF-STEM images of a 10-unit-cell YMnO$_3$ thin film overlaid with the spatial distribution of the trimerization amplitude Q at the temperatures $T = 448$ K (**a**), 473 K (**b**), and 498 K (**c**), with $T_Q = 498$ K as phase transition temperature. **d–f** Histogram plots showing the number of occurences N of the Q and φ values (defined in Fig. 1a) for each temperature in **a–c**, respectively.

Hence, we see that the interface to the substrate and reduced dimension of the thin films have a profound impact on **Q**, and in turn on the improper spontaneous polarization through the coupling between **Q** and **P**$_s$.

Real-space observation of the structural phase transition. Next, we exploit the lowering of transition temperature in the improper ferroelectric thin films to determine the nature of the improper ferroelectric phase transition in the YMnO$_3$ system. We use the thickness dependence of the transition temperature to push T_C^{film} to experimentally accessible temperatures, where we can monitor the paraelectric state at $T > T_C^{\text{film}}$ directly, using in situ STEM (Fig. 4a, b). We find that the atomic positions of the Y atoms do not lose their displacement amplitude in the non-polar $P6_3/mmc$ phase above T_C^{film}. Instead, we observe a spread of intensity of the Y peaks along the c-axis direction. The resulting ellipticity of the atomic peaks arises precisely at T_C^{film} (Fig. 4c) and corresponds to a superposition of atomic states covering the same range of displacement amplitudes as observed in the ordered phase at lower temperatures. Evidently, the displacement of Y atoms is locally preserved in the paraelectric phase but the long-range order is lost. This is a signature of a specific type of order–disorder (here, $Z_6 \rightarrow U(1)$) transition: the amplitude Q is

uniformly nonzero on either side of the phase transition whereas φ exhibits long-range order, taking on one of the six allowed trimerization angles ($n \cdot \pi/3$; $n = 0, 1, \ldots, 5$) below the transition temperature and disorder, with a random distribution of φ between 0 and 2π, above it (Supplementary Fig. 6). Such behavior has also been recently reported from neutron scattering experiments for bulk YMnO$_3$[39], and here we now observe it directly and in real space.

Discussion

In conclusion, we have provided insight into key features of the evolution of improper ferroelectricity in ultrathin YMnO$_3$ by achieving independent access to the leading and the dependent order parameters. On the microscopic level, we have shown how interface clamping and film-thickness effects act directly on the leading order parameter, the lattice trimerization expressed by **Q**. We furthermore identify these effects as the dominant mechanisms defining the nanoscale ferroelectric properties in YMnO$_3$, in terms of its ferroelectric transition temperature and threshold thickness. We have exploited the reduced transition temperature in the thin films to directly visualize the phase transition with atomic resolution and establish that it is of a particular order–disorder type.
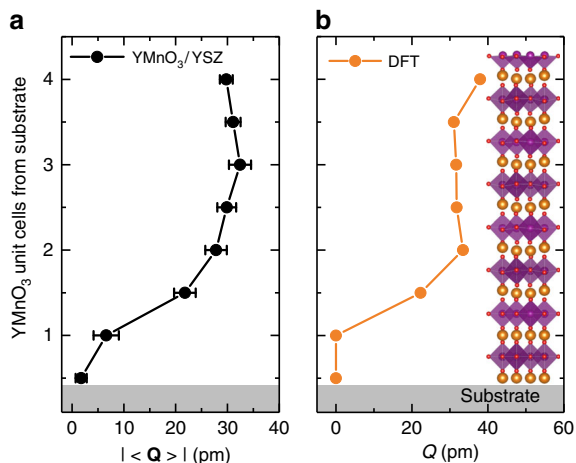
Fig. 3 Influence of the substrate-film interface on the improper ferroelectricity. **a** Averaged displacement $|\langle \mathbf{Q} \rangle|$ for each atomic row in the first four unit cells of the HAADF-STEM image in Fig. 2a. The value of $|\langle \mathbf{Q} \rangle|$ is reduced at the substrate interface and saturates at the bulk displacement value after two unit cells. The error bars are given by the standard error of the mean. **b** Trimerization amplitude Q calculated by density-functional theory (DFT) for a four-unit-cell YMnO₃ film keeping the bulk-lattice parameters and assuming a clamped ($Q = 0$) unit cell toward the substrate interface and a free top surface. The amplitude displays a progressive build up over the thickness of the film and saturates after two-unit cells. The inset in **b** shows a schematic of the corresponding crystal structure with atomic positions as calculated by DFT.

The results presented here point to the criteria setting the lower thickness limits for insertion of geometrically driven improper ferroelectric layers in nanotechnological heterostructures. Rather than the depolarizing field providing the main challenge to achieving polar thin films, as in proper ferroelectrics, improper ferroelectricity in ultrathin films is determined by the thin-film-specific behavior of its driving, non-polar order parameter. The generality of our findings is corroborated by our ongoing experiments on different substrates and using other compounds of the hexagonal-manganite series.

Our results thus indicate that the improper nature of a ferroelectric state can be used for steering polarization in nanotechnologically relevant ultrathin films through a depolarization-free primary order parameter. For example, the leading-order structural distortions may be tuned by choosing a differently sized rare-earth or transition-metal ion than Y or by insertion of spacer or capping layers[25] with different mechanical boundary conditions, independent of their respective charge-screening properties. These approaches available to control improper ferroelectricity in thin films may provide additional degrees of freedom complementing the possibilities available to conventional ferroelectrics.

Methods

Thin-film growth and structural characterization. The YMnO₃ thin films were grown on YSZ(111) substrates by pulsed laser deposition (PLD) using a KrF excimer laser at 248 nm, an energy fluence of 0.5–0.7 J/cm² and a repetition rate of 8 Hz, ablating from a stoichiometric YMnO₃ target. Before thin-film deposition, each substrate was annealed in air at 1250 °C for 12 h. During the thin-film deposition, the substrate was kept at 750–800 °C in 0.12 mbar O₂ environment. The thickness of the thin films was monitored using RHEED during growth and cross-checked with post-deposition X-ray reflectivity. The structural phase and orientation of the epitaxial films was determined using X-ray diffraction (Supplementary Fig. 1a, b). The X-ray characterization was performed using a PanAnalytical X'Pert³ MRD diffractometer. The thin-film
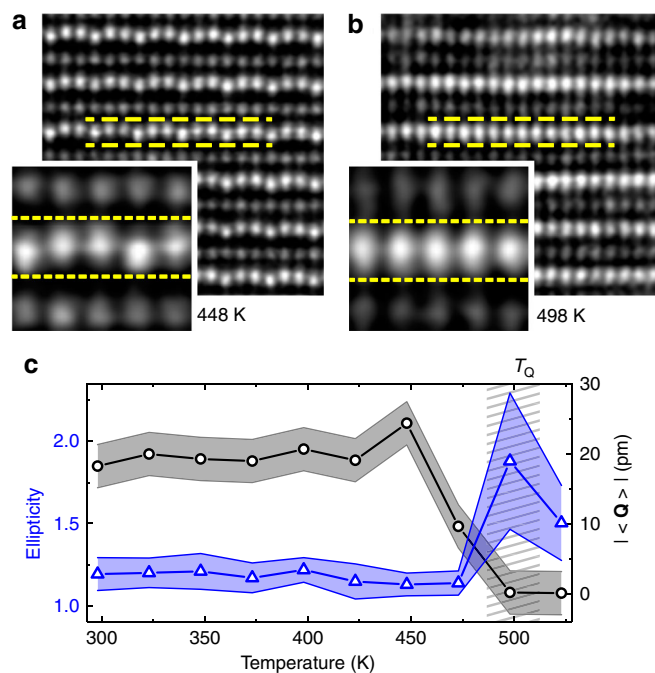

Fig. 4 Real-space observation of the order–disorder-type phase transition. **a**, **b** The dashed yellow lines highlight the agreement between discrete displacement amplitudes in the ferroelectric phase (**a**) and the spread of the Y peaks in the paraelectric phase (**b**) in the 10-unit-cell YMnO₃ thin film. An order–disorder character of the structural phase transition is revealed, where loss of long-range order ($|\langle \mathbf{Q} \rangle| \to 0$) is accompanied by the observation of elliptic Y atomic peaks due to superposition of a continuum of displacement states. **c** The average of $\mathbf{Q}$ (black circles) and average Y atomic peak ellipticity (blue triangles) from HAADF-STEM plotted as function of temperature for the same sample as in **a**, **b**. The increase of ellipticity arises directly as T_Q (indicated by the gray hatched area) is crossed. The error bars for $|\langle \mathbf{Q} \rangle|$ correspond to the estimated experimental error in determining $\mathbf{Q}$ during the in situ heating experiment. The error bars of the ellipticity are given by the standard deviation.

topography (Supplementary Fig. 1c) was characterized using a Bruker Multimode 8 atomic force microscope.

In situ SHG (ISHG). The optical SHG signal was generated in reflection (see schematic in Supplementary Fig. 2a), in situ in the thin-film growth environment[32,33]. A pulsed Ti:Sapphire laser at 800 nm with a pulse duration of 45 fs and repetition rate of 1 kHz was converted using an optical parametric amplifier to a probe wavelength of 860 nm. This probe beam was incident on the sample with a pulse energy of 20 µJ on a spot size 250 µm in diameter. The generated light intensity (ISHG) was subsequently detected using a monochromator set to 430 nm and a photomultiplier system.

Scanning transmission electron microscopy. Samples for STEM analysis were prepared by means of a FEI Helios NanoLab 600i focused-ion beam (FIB) operated at accelerating voltages of 30 and 5 kV. For the in situ heating experiments several thick lamellae of the 10-unit-cell YMnO₃ film grown on YSZ were cut with the FIB and transferred to the Protochips Fusion Heating E-chips by using an EasyLift manipulator. After securing the FIB lamellae to the E-chips with Pt, the lamellae were further milled to electron transparency. The in situ heating studies were conducted using a Protochips Fusion 500 double-tilt holder with a Keithley 2636B power supply. A FEI Titan Themis with a probe CEOS DCOR spherical aberration corrector operated at 300 kV and equipped with a FEI CETA 2 camera was used for HAADF-STEM imaging and nanobeam electron diffraction pattern acquisition.

For the atomic-resolution HAADF-STEM data acquisition, a probe semi-convergence angle of 18 mrad was used in combination with an annular semi-detection range of the annular dark-field detector set to collect electrons scattered between 66 and 200 mrad. The temperature was raised from room temperature to 250 °C in steps of 25 °C at a rate of 1 °C s⁻¹. At each step the temperature was kept constant for approximately 6–7 min in order to allow the sample to sufficiently

stabilize (thermal drift occurs due to thermal expansion of the heating chip) and to acquire several time series consisting of 20 frames. Averages of the time series were subsequently obtained after both rigid and non-rigid registration using the Smart Align Software[40].

Density-functional calculations. For our DFT calculations of the ferroelectric slabs of $YMnO_3$, we used the Vienna ab initio simulation package (VASP)[41–43] which uses the projector augmented wave method[44]. We used the PBEsol + U[45] functional and we consider $4s^2 4p^6 4d^2 5s^1$ for Y, $3s^2 3p^6 3d^6 4s^1$ for Mn and $2s^2 2p^4$ for O as valence. We used an artificial collinear up–up–down, down–down–up configuration for the magnetic moments on the Mn as is common in literature. To take into account electron correlations we used the Liechtenstein approach[46] with a U of 4.5 eV and a J of 0.5 eV. In the relaxation process, we fixed the first unit cell and let the remaining atoms relax until the forces on the atoms were below 10^{-3} eV/Å. Our slab consists of 4 unit cells and around 50 Å of vacuum along the c-axis and we applied dipole corrections along the c-axis.

Data availability
The data that support the findings of this study are available from the corresponding authors upon request.

References
1. Levanyuk, A. P. & Sannikov, D. G. Improper ferroelectrics. *Sov. Phys. Uspekhi* **17**, 199 (1974).
2. Fiebig, M., Lottermoser, T., Meier, D. & Trassin, M. The evolution of multiferroics. *Nat. Rev. Mater.* **1**, 16046 (2016).
3. Setter, N. et al. Ferroelectric thin films: review of materials, properties, and applications. *J. Appl. Phys.* **100**, 051606 (2006).
4. Martin, L. W. & Rappe, A. M. Thin-film ferroelectric materials and their applications. *Nat. Rev. Mater.* **2**, 16087 (2016).
5. Yang, S. M. et al. Mixed electrochemical–ferroelectric states in nanoscale ferroelectrics. *Nat. Phys.* **13**, 812–818 (2017).
6. Hill, N. A. Why are there so few magnetic ferroelectrics? *J. Phys. Chem. B.* **104**, 6694–6709 (2000).
7. Cheong, S.-W. & Mostovoy, M. Multiferroics: a magnetic twist for ferroelectricity. *Nat. Mater.* **6**, 13–20 (2007).
8. Kimura, T. et al. Magnetic control of ferroelectric polarization. *Nature* **426**, 55–58 (2003).
9. Benedek, N. A. & Fennie, C. J. Hybrid improper ferroelectricity: a mechanism for controllable polarization-magnetization coupling. *Phys. Rev. Lett.* **106**, 107204 (2011).
10. Fong, D. D. et al. Ferroelectricity in ultrathin perovskite films. *Science* **304**, 1650–1653 (2004).
11. Sai, N., Fennie, C. J. & Demkov, A. A. Absence of critical thickness in an ultrathin improper ferroelectric film. *Phys. Rev. Lett.* **102**, 107601 (2009).
12. Stengel, M., Fennie, C. J. & Ghosez, P. Electrical properties of improper ferroelectrics from first principles. *Phys. Rev. B.* **86**, 94112 (2012).
13. Van Aken, B. B., Palstra, T. T. M., Filippetti, A. & Spaldin, N. A. The origin of ferroelectricity in magnetoelectric $YMnO_3$. *Nat. Mater.* **3**, 164–170 (2004).
14. Fennie, C. J. & Rabe, K. M. Ferroelectric transition in YMnO3 from first principles. *Phys. Rev. B.* **72**, 100103 (2005).
15. Artyukhin, S., Delaney, K. T., Spaldin, N. A. & Mostovoy, M. Landau theory of topological defects in multiferroic hexagonal manganites. *Nat. Mater.* **13**, 42–49 (2014).
16. Choi, T. et al. Insulating interlocked ferroelectric and structural antiphase domain walls in multiferroic YMnO3. *Nat. Mater.* **9**, 253–258 (2010).
17. Jungk, T., Hoffmann, Á., Fiebig, M. & Soergel, E. Electrostatic topology of ferroelectric domains in $YMnO_3$. *Appl. Phys. Lett.* **97**, 12904 (2010).
18. Meier, D. et al. Anisotropic conductance at improper ferroelectric domain walls. *Nat. Mater.* **11**, 284–288 (2012).
19. Wu, W., Horibe, Y., Lee, N., Cheong, S.-W. & Guest, J. R. Conduction of topologically protected charged ferroelectric domain walls. *Phys. Rev. Lett.* **108**, 77203 (2012).
20. Mundy, J. A. et al. Functional electronic inversion layers at ferroelectric domain walls. *Nat. Mater.* **16**, 622–627 (2017).
21. Lilienblum, M. et al. Ferroelectricity in the multiferroic hexagonal manganites. *Nat. Phys.* **11**, 1070–1073 (2015).
22. Shigemitsu, N. et al. Pulsed-laser-deposited YMnO3 epitaxial films with square polarization-electric field hysteresis loop and low-temperature growth. *Jpn. J. Appl. Phys.* **43**, 9B (2004).
23. Doh, J., Leung, C. W., MacManus-Driscoll, J. L. & Blamire, M. G. Epitaxial and oriented YMnO3 film growth by pulsed laser deposition. *J. Cryst. Growth* **267**, 548–553 (2004).
24. Kordel, T. et al. Nanodomains in multiferroic hexagonal RMnO3 films (R=Y, Dy,Ho,Er). *Phys. Rev. B* **80**, 045409 (2009).
25. Laukhin, V. et al. Electric-field control of exchange bias in multiferroic epitaxial heterostructures. *Phys. Rev. Lett.* **97**, 1–4 (2006).
26. Lee, D. et al. Giant flexoelectric effect in ferroelectric epitaxial thin films. *Phys. Rev. Lett.* **107**, 57602 (2011).
27. Sheng, Z., Ogawa, N., Ogimoto, Y. & Miyano, K. Multiple stable states with in-plane anisotropy in ultrathin YMnO3 films. *Adv. Mater.* **22**, 5507–5511 (2010).
28. Sheng, Z., Ogawa, N., Ogimoto, Y. & Miyano, K. Stability of spontaneous polarization in ultrathin improper ferroelectrics. *Phys. Rev. B.* **84**, 140101(R) (2011).
29. Roddatis, V. V., Akbashev, A. R., Lopatin, S. & Kaul, A. R. Complex structural-ferroelectric domain walls in thin films of hexagonal orthoferrites RFeO3 (R = Lu, Er). *Appl. Phys. Lett.* **103**, 112907 (2013).
30. Mundy, J. A. et al. Atomically engineered ferroic layers yield a room-temperature magnetoelectric multiferroic. *Nature* **537**, 523–527 (2016).
31. Cheng, S. et al. Interface reconstruction with emerging charge ordering in hexagonal manganite. *Sci. Adv.* **4**, eaar4298 (2018).
32. Nordlander, J., De Luca, G., Strkalj, N., Fiebig, M. & Trassin, M. Probing ferroic states in oxide thin films using optical second harmonic generation. *Appl. Sci.* **8**, 570 (2018).
33. De Luca, G. et al. Nanoscale design of polarization in ultrathin ferroelectric heterostructures. *Nat. Commun.* **8**, 1419 (2017).
34. Fiebig, M., Pavlov, V. V. & Pisarev, R. V. Second-harmonic generation as a tool for studying electronic and magnetic structures of crystals: review. *J. Opt. Soc. Am. B* **22**, 96–118 (2005).
35. Denev, S. A., Lummen, T. T. A., Barnes, E., Kumar, A. & Gopalan, V. Probing ferroelectrics using optical second harmonic generation. *J. Am. Ceram. Soc.* **94**, 2699–2727 (2011).
36. Junquera, J. & Ghosez, P. Critical thickness for ferroelectricity in perovskite ultrathin films. *Nature* **422**, 506–509 (2003).
37. Holtz, M. E. et al. Topological defects in hexagonal manganites: Inner structure and emergent electrostatics. *Nano Lett.* **17**, 5883–5890 (2017).
38. Meier, Q. N. et al. Global formation of topological defects in the multiferroic hexagonal manganites. *Phys. Rev. X* **7**, 41014 (2017).
39. Skjærvø, S. H. et al. Unconventional continuous structural disorder at the order-disorder phase transition in the hexagonal manganites. *Phys. Rev. X.* **9**, 031001 (2019).
40. Jones, L. et al. Smart Align—a new tool for robust non-rigid registration of scanning microscope data. *Adv. Struct. Chem. Imaging* **1**, 8 (2015).
41. Kresse, G. & Hafner, J. Ab initio molecular dynamics for liquid metals. *Phys. Rev. B* **47**, 558–561 (1993).
42. Kresse, G. & Furthmüller, J. Efficient iterative schemes for ab initio total-energy calculations using a plane-wave basis set. *Phys. Rev. B* **54**, 11169–11186 (1996).
43. Kresse, G. & Joubert, D. From ultrasoft pseudopotentials to the projector augmented-wave method. *Phys. Rev. B* **59**, 1758–1775 (1999).
44. Perdew, J. P. et al. Restoring the density-gradient expansion for exchange in solids and surfaces. *Phys. Rev. Lett.* **100**, 136406 (2008).
45. Blöchl, P. E. Projector augmented-wave method. *Phys. Rev. B* **50**, 17953–17979 (1994).
46. Liechtenstein, A. I., Anisimov, V. I. & Zaanen, J. Density-functional theory and strong interactions: orbital ordering in Mott-Hubbard insulators. *Phys. Rev. B* **52**, R5467–R5470 (1995).

Author contributions
All authors discussed the results. J.N., M.F., and M.T. wrote the manuscript. J.N. performed the thin-film growth, XRD, and SHG polarization characterization. M.C., R.E., and M.D.R. carried out the STEM analysis. Q.N.M., A.C., and N.A.S. provided the DFT calculations. M.T. and M.F. designed the experiment and supervised the work jointly with M.D.R., A.C., and N.A.S.

Competing interests
The authors declare no competing interests.

Additional information

Epitaxial growth of improper ferroelectric h-YMnO$_3$ thin films using surface engineering

D

Epitaxial growth of improper ferroelectric h-YMnO$_3$ thin films by surface engineering

J. Nordlander,[1, *] M. D. Rossell,[2] M. Campanini,[2] M. Fiebig,[1] and M. Trassin[1, †]

[1] *Department of Materials, ETH Zurich, Zurich, Switzerland*
[2] *Electron Microscopy Center, Empa, Dübendorf, Switzerland*

We report on multiple fundamental qualitative improvements in the growth of improper ferroelectric hexagonal YMnO$_3$ (YMO) thin films and heterostructures by pulsed laser deposition. We improve the quality of the yttria-stabilized zirconia (YSZ) substrates by pre-growth annealing. Together with low-energy-fluence laser ablation we thus obtain a two-dimensional growth mode of YMO films with ultralow roughness and devoid of misoriented nanocrystalline inclusions. By inserting a double layer of sacrificial YMO and conducting indium-tin oxide between the substrate and the final film, we can grow the latter in a fully lattice-relaxed mode and, thus, without any misfit dislocations while maintaining the extraordinary flatness of the films grown directly on pre-annealed YSZ. This provides a template for the fabrication of heterostructures based on hexagonal manganites as promising class of improper room-temperature ferroelectrics and their implementation into technologically relevant epitaxial metal | ferroelectric-type multilayers.

Materials possessing coexisting ferroelectric and magnetic order are interesting for their rich physics and the great potential for novel technological applications resulting from magnetoelectric cross-coupling effects. The hexagonal rare-earth manganites, RMnO$_3$ (RMO) with R = Sc, Y, In, Dy-Lu, are textbook examples of such so-called multiferroic compounds. Here, improper ferroelectricity emerges between 1250 and 1650 K [1, 2] through its coupling to a non-ferroelectric lattice trimerization. A coexistence of this improper ferroelectric state with antiferromagnetic Mn^{3+} order is seen below temperatures between 65 and 130 K [3]. The hexagonal manganites have been studied as bulk crystals and are particularly famous for their characteristic, topologically protected six-fold vortex trimerization–polarization domain pattern [4, 5], unconventional domain-wall conductance [6] and coupling of ferroelectric and antiferromagnetic domains [7]. Hence, these materials can be the source of exotic ferroelectric functionalities not found in conventional ferroelectrics. Exploiting such phenomena in applications, however, depends on the implementability of RMO as single-crystal thin film in epitaxial heterostructures. In the technologically relevant ultrathin regime, it was shown that the epitaxial constraints imposed by the substrate on YMO films can significantly alter the structural distortions related to the primary-order lattice trimerization, which in turn affects the emergence of the improper polarization [8]. The main challenge in studying such nanoscale effects and putting these films to use in devices resides in the difficulty to find lattice-matching substrates and suitable electrode materials promoting high-quality epitaxy of the hexagonal phase. So far, epitaxial hexagonal RMO films have been realized on substrates including (111)-oriented yttria-stabilized zirconia (YSZ), Si, Pt, MgO and c-cut Al$_2$O$_3$ [9–17]. However, in many of these cases, the films exhibited a tendency to form secondary crystalline phases or orientations. Because the hexagonal manganites are uniaxial ferroelectrics with a polarization along the c-axis, strictly c-axis-oriented films are required, in addition to precise control of layer thickness at the nanoscale, for optimal implementation in heterostructures for oxide-electronics applications.

Here, choosing YMO as model compound, we demonstrate a route towards layer-by-layer growth of c-oriented, single-crystal ultrathin hexagonal manganite films on (111)-oriented YSZ, both with and without use of a conducting indium-tin oxide (ITO) buffer layer.

To grow our YMO films, we use pulsed laser deposition. The growth mode is monitored in-situ using reflection high-energy electron diffraction (RHEED) and characterized post growth using atomic force microscopy (AFM), x-ray diffraction (XRD) and high-resolution scanning transmission electron microscopy (STEM). We finally probe the improper ferroelectric polarization of the films using optical second harmonic generation (SHG).

The growth parameters are optimized on as-received, commercial (111)-oriented YSZ substrates (CrysTec GmbH). We use a stoichiometric ceramic target for laser ablation where the substrate is kept at 750°C in an oxygen partial pressure of 0.1 mbar. While the (111)-oriented cubic lattice has a hexagonal surface symmetry, perfect matching with the hexagonal lattice of the manganites remains challenging. For example, the presence of nanoinclusions with secondary c-axis orientations due to multiple lattice-matching conditions on YSZ substrates have been reported [18, 19]. Such nanoinclusions are also observed in some of the films in this work, see
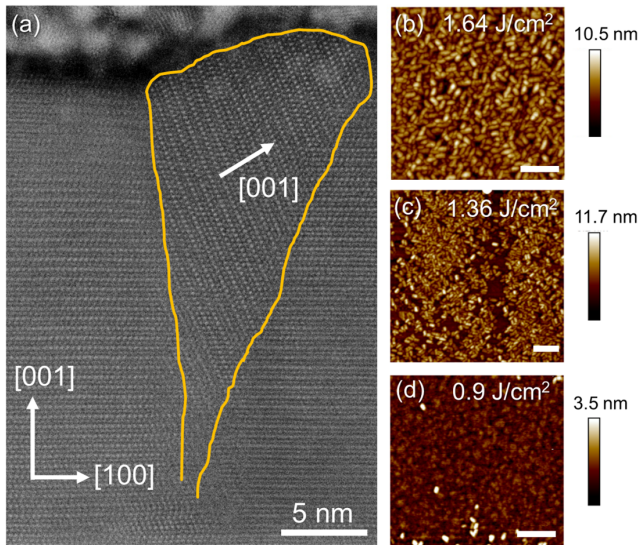

FIG. 1. (a) Bright-field STEM image of a hexagonal YMO thin film showing the presence of a misoriented grain, outlined in yellow. The arrows indicate the direction of the hexagonal c axis. (b-d) AFM topography scans of YMO films that were grown on as-received YSZ substrates at different laser fluences. The scale bar is 200 nm.
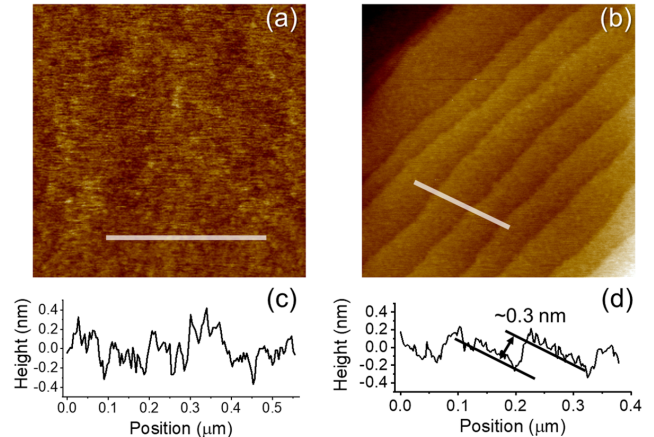

FIG. 2. AFM topography scans of an YSZ substrate in as-received condition (a) before and (b) after subjecting it to thermal annealing. The scan size is 1 μm^2. Line scans at the locations of the white lines are shown in (c) and (d), respectively. After annealing, the substrate exhibits a strikingly improved surface quality with steps of a height of about 0.3 nm, corresponding the the distance between the (111) crystallographic planes.

Fig. 1(a). We thus start our investigation by tracking the grain density as function of the deposition conditions using AFM. The surface topography of YMO films grown at different laser fluences are shown in Fig. 1(b-d). We find that a high laser fluence results in a rough surface with a high density of misoriented nanocrystals. As the fluence is decreased, less nanocrystals are observed and below 1 J/cm^2 they are hardly detected anymore. In this state, we also find a smooth surface with a roughness of 0.34 nm, which therefore is likely to be correlated to the reduction in the density of misoriented grains inside the films.

In order to improve the smoothness and single-crystallinity of the films further, we investigate the influence of the substrate surface topography on the YMO film growth. While the as-received YSZ substrates already have a low roughness of 0.16 nm, a further improvement of the surface quality may facilitate island nucleation for a layer-by-layer growth mode [20]. We therefore induce surface reconstruction by annealing the substrates in air at 1250°C for 12 hours [21]. As seen in Fig. 2, this annealing step significantly improves the surface morphology of the YSZ substrates. Specifically, it results in the formation of terraces with the step height of about 0.3 nm, corresponding to the distance between the (111) lattice planes in YSZ.

Applying the same growth protocol as with the as-received substrates, we use RHEED monitoring to asses

the growth mode for the deposition of YMO on the annealed YSZ subtrates. The RHEED intensity oscillations in Fig. 3(a) indicate a layer-by-layer type growth mode. Film-thickness calibration by post-deposition x-ray reflectivity measurements reveals that each deposited monolayer is half a unit cell in height. Hence, in this growth mode, we achieve thickness control with sub-unit-cell precision. Most strikingly, the surface of the YMO films grown on the annealed YSZ substrates preserves the step-like morphology of the substrate and thus exhibits an ultralow roughness of less than 0.3 nm (Fig. 3(b)). Furthermore, x-ray $\theta/2\theta$ scans reveal a c-oriented YMO film with no trace of secondary phases or orientations (Fig. 3(c)). The high quality of the film is further confirmed through XRD characterization. The visibility of thickness (Laue) oscillations around the YMO film peaks indicates sharp interfaces and the narrow rocking curve with a full-width at half-maximum (FWHM) of 0.05° points to a low mosaicity, see Fig. 3(d,e).

Having optimized the growth of ultrathin YMO films directly on YSZ, we now move on to identify a bottom-electrode material that allows us to preserve the excellent epitaxy and the layer-by-layer growth mode of the YMO. Here we propose ITO as the material of choice. As seen in Table I, the bulk lattice constant of ITO, here taken as that of In$_2$O$_3$, lies close to that of YMO, with a lattice mismatch of less than 1%, suggesting enhanced compatibility with the YMO lattice. As described in Ref. 8, the YMO films grown directly on YSZ are not strained to the substrate, but rather adopt bulk-like in-plane lattice
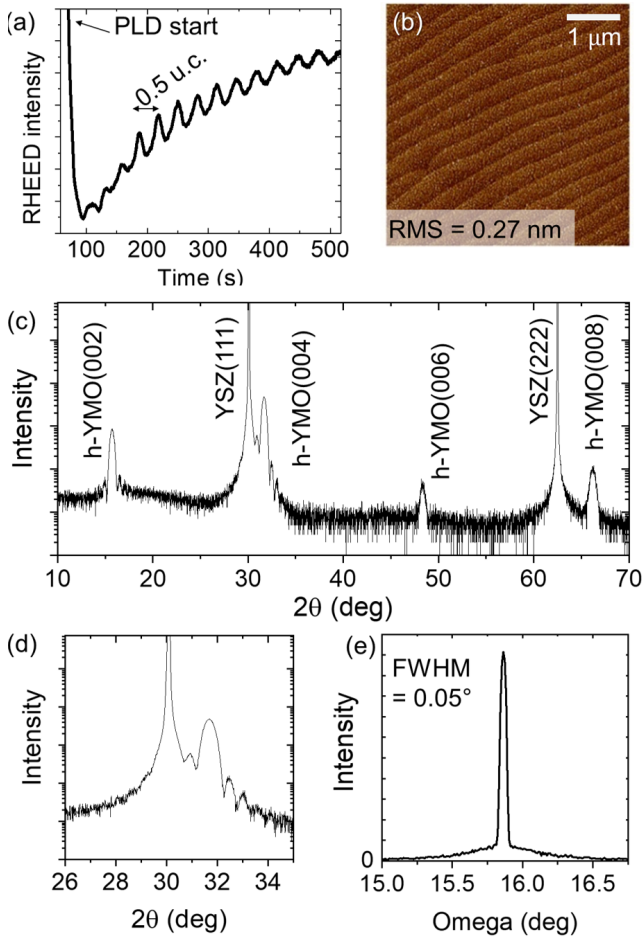
FIG. 3. (a) RHEED intensity during YMO growth. The layer-by-layer-type growth mode is seen by the intensity oscillations, where each period corresponds to half a unit cell. (b) AFM topography scan of a YMO film with a thickness of 15 unit cells. (c) θ/2θ XRD scan showing hexagonal (00l) peaks only. (d) High-resolution θ/2θ scan around YSZ(111) and YMO(004). Laue oscillations around the film peak confirms the exceptional smoothness of the interfaces. (e) Rocking curve of YMO(004) with a narrow FWHM of 0.05°, further indicating a highly oriented YMO film. The corresponding FWHM of YSZ(111) is 0.009°.

its small lattice mismatch to YMO, it can adapt to the lattice constant and the surface flatness of the YMO. Second, it poses a barrier to the development of the misfit dislocations in the sacrificial YMO layer. Third, with its high conductivity it acts as bottom electrode of an YMO heterostructure. In the next step, we deposit the actual YMO layer on top of the ITO. With this strategy the ITO will have already assumed the lattice constant of the YMO, such that this second YMO layer grows with full lattice relaxation and, most importantly, without misfit dislocations. We thus expect to complete our heterostructure with an YMO layer of expected drastically improved quality. At the same time, the option to exchange the YMO in the sacrificial layer by one of the other RMO compounds allows us to exert to introduce a controlled, moderate lattice strain into the final YMO layer.

For verifying the proposed growth strategy, we grow the ITO films at a substrate temperature of 800°C and at a laser energy fluence of 0.7 J/cm^2 with an oxygen partial pressure of 0.12 mbar. We find that ITO films grown on top of an ultrathin ($\lesssim$ 2 unit cells) RMO buffer layer on the YSZ(111) substrate indeed adopt to the lattice constant of the RMO buffer layer. In this case, no strain-relaxation is seen with increasing ITO thickness up to 50 nm and ultraflat, (111)-oriented ITO films were obtained. [Fig. 4(a)]. We note that the route presented above to achieve ultraflat ITO films that are lattice matched to the hexagonal manganites is also applicable for achieving high-quality films of undoped In$_2$O$_3$.

In a next step, we find that our YMO films grown on top of this ITO conducting layer, still at 800°C and an oxygen partial pressure of 0.12 mbar, retain a similar layer-by-layer growth mode as on YSZ [Fig. 4(b)]. Thus, growth of highly oriented hexagonal YMO with smooth interfaces is obtained also in the case of an RMO-buffered ITO film as growth template. Indeed, x-ray reciprocal space mapping (RSM) around the YMO(308) reflection confirms the epitaxial relationship in the trilayer system.

parameters by forming misfit dislocations at the YSZ interface. Remarkably, despite these local lattice defects, the YMO films maintain a smooth surface. This opens up a strategy towards obtaining YMO films of a fundamentally improved epitaxial quality. The strategy is as follows. We first grow a "sacrificial YMO layer" on top of the YSZ. Its purpose is to accommodate to the intrinsic lattice constant of YMO through the development of misfit dislocations but keep the surface flatness of the substrate. On top of this sacrificial YMO layer, we deposit the ITO with a threefold purpose. First, with

TABLE I. Bulk lattice parameters of the substrates (S) with relation to the YMO lattice for $[001]_{YMO}||[111]_S$ and $[\overline{1}20]_{YMO}||[1\overline{1}0]_S$. The equivalent hexagonal lattice parameter of YMO for both substrates are given as well as the corresponding lattice mismatch.

Param.	Cubic a (Å)	Hex. a (Å)	Lattice mismatch (%)
YMO	-	6.14	-
YSZ	5.12	6.27 [a]	+2.1
In$_2$O$_3$	10.117	6.20 [b]	+0.98

[a] Equivalent hexagonal a parameter for $d_{300}^{YMO} = d_{20\overline{2}}^{YSZ}$
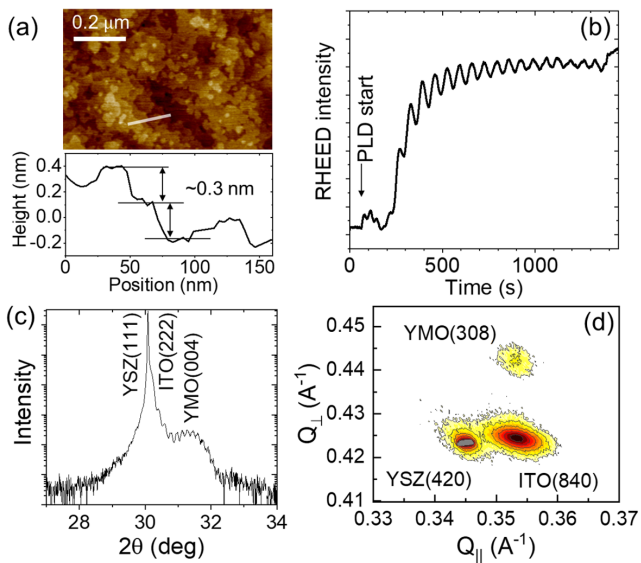[b] Equivalent hexagonal a parameter for $d_{300}^{YMO} = d_{40\overline{4}}^{In_2O_3}$

FIG. 4. (a) AFM topography scan of the ITO film. The steps in the topography are ∼0.3 nm, corresponding to the distance between the (222) crystallographic planes of ITO. (b) RHEED oscillations during YMO growth on the ITO bottom electrode indicate a layer-by-layer growth mode. (c) High-resolution $\theta/2\theta$ scan reveals Laue oscillations around the ITO(222) reflection. (d) RSM of the YMO(308) reflection in the vicinity of the YSZ and ITO peaks. ITO and YMO adopt the same in-plane lattice parameter, yet relaxed against the YSZ substrate.

We find that the thin-film layers all have matching in-plane lattices, yet relaxed against the YSZ substrate. We further confirm the structural quality of the YMO thin films and their interfaces by high-angle annular dark-field (HAADF) STEM (see Fig. 5(a,b)). We find sharp interfaces in both cases. The characteristic ferroelectric trimerization of the hexagonal manganites is seen in both films as an up-up-down displacement pattern of Y atoms along the c axis. Note that our growth strategy not only leads to YMO film of significantly improved quality. The demonstration of mutual lattice matching between RMO and ITO films furthermore presents a route to construct coherently strained (metal| improper ferroelectric)-type multilayers combining hexagonal and cubic thin-film oxides.

Finally, we probe the improper ferroelectric polarization in the epitaxial YMO thin films by laser-optical SHG in reflection, see Fig. 5(c). SHG denotes a frequency-doubling of light which is especially sensitive to inversion-symmetry breaking in a material, thus relating the SHG signal directly to the presence of the spontaneous polarization as ferroelectric order parameter [22–24]. In particular, the light-polarization dependence of the SHG response is dictated by the point-group symmetry of
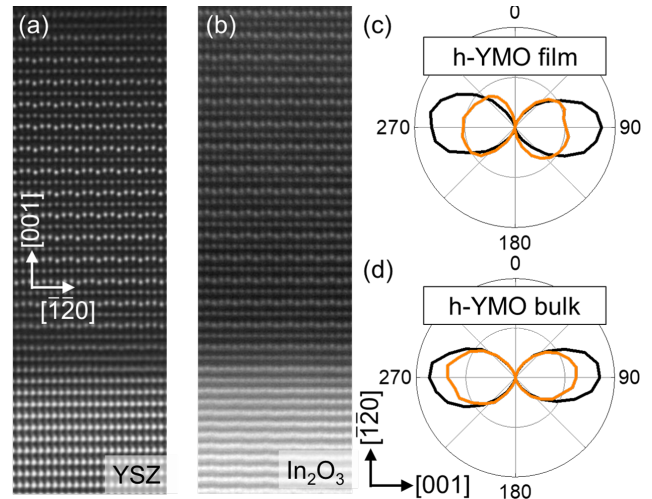

FIG. 5. (a,b) HAADF-STEM along the [100] ((parallel to [x])) zone axis of 15-unit-cell YMO thin films on YSZ (a) and In₂O₃ (b) confirming the high crystalline quality of the YMO thin film samples is confirmed by. Corrugation of the Y plane characteristic of the lattice trimerization driving the ferroelectric order is seen in both samples. (c) SHG characterization of a YMO film grown on an annealed YSZ(111) substrate. The SHG polarimetry is measured by rotating the light-polarization of the incident beam from 0° to 360° and detecting the component of the SHG light polarized parallel (black) and perpendicular (orange) with respect to the polarization of the incoming light. Here, 0° and 90° correspond to light polarized parallel and perpendicular, respectively, to the plane of light reflection. The SHG polarimetry reveals a symmetry compatible with the 6mm point group of YMO in the improper ferroelectric phase with a spontaneous polarization along the normal of the film (projected along 90°/270°). Observation of an identical SHG response from a c-cut YMO bulk crystal (d) further confirms this conclusion.

the material, which for the ferroelectric phase of YMO is 6mm. The emission of SHG light from the YMO thin films indicates that, indeed, thesse films exhibit a macroscopic polarization. Polarimetry of the SHG signal, shown in Fig. 5(c), is compatible with the 6mm point group and further confirms an out-of-plane-oriented polarization in the film [here corresponding to 90° in Fig. 5(c)]. Note that the SHG polarimetry signal is identical to that of a bulk YMO crystal [Fig.5(d)]. In particular, no signature of in-plane polarization components as they would be caused by the aforementioned misoriented nanoinclusions is observed.

In summary, we have demonstrated layer-by-layer growth of ultrathin YMO thin films on insulating YSZ, with and without insertion of an electrode layer. We find that an ultraflat substrate surface can be achieved by YSZ substrate annealing. This, in combination with a low energy fluence during PLD is key to achieving layer-

by-layer growth of epitaxial YMO films with sub-unit-cell thickness control. We have further demonstrated a route to preserve this excellent thin-film quality even after insertion of an intermediate ITO electrode layer. We insert a sacrificial RMO layer on YSZ to seed the growth of ITO. By this method, we find that the ITO layer is lattice-matched to YMO, and mutual heteroepitaxy is thus achieved between the two. Hence, we have demonstrated multifold fundamental improvements in the qual-ity of the notoriously difficult to grow hexagonal manganite films. This approach further suggests the feasibility of constructing epitaxial superlattices of metal|ferroelectric type using the hexagonal manganites as improper room-temperature ferroelectrics. Improper ferroelectrics are presently recognized as a promising class of functional materials because of a variety of properties surpassing those of conventional ferroelectrics. Here our work can advance the implementation of improper ferroelectrics into functional devices considerably.

[1] M. Lilienblum, T. Lottermoser, S. Manz, S. M. Selbach, A. Cano, and M. Fiebig, Ferroelectricity in the multiferroic hexagonal manganites, Nature Physics **11**, 1070 (2015).

[2] S. C. Chae, N. Lee, Y. Horibe, M. Tanimura, S. Mori, B. Gao, S. Carr, and S.-W. Cheong, Direct Observation of the Proliferation of Ferroelectric Loop Domains and Vortex-Antivortex Pairs, Physical Review Letters **108**, 167603 (2012).

[3] B. Lorenz, Hexagonal manganites—(RMnO$_3$): Class (i) multiferroics with strong coupling of magnetism and ferroelectricity, ISRN Condensed Matter Physics **2013**, 497073 (2013).

[4] T. Choi, Y. Horibe, H. T. Yi, Y. J. Choi, W. Wu, and S.-W. Cheong, Insulating interlocked ferroelectric and structural antiphase domain walls in multiferroic YMnO$_3$, Nature Materials , 253–258 (2010).

[5] T. Jungk, Á. Hoffmann, M. Fiebig, and E. Soergel, Electrostatic topology of ferroelectric domains in YMnO$_3$, Applied Physics Letters **97**, 12904 (2010).

[6] D. Meier, J. Seidel, A. Cano, K. Delaney, Y. Kumagai, M. Mostovoy, N. A. Spaldin, R. Ramesh, and M. Fiebig, Anisotropic conductance at improper ferroelectric domain walls, Nature Materials **11**, 284 (2012).

[7] M. Fiebig, T. Lottermoser, D. Fröhlich, A. V. Goltsev, and R. V. Pisarev, Observation of coupled magnetic and electric domains, Nature **419**, 818 (2002).

[8] J. Nordlander, M. Campanini, M. D. Rossell, R. Erni, Q. N. Meier, A. Cano, N. A. Spaldin, M. Fiebig, and M. Trassin, The ultrathin limit of improper ferroelectricity, Nature Communications **10**, 5591 (2019).

[9] N. Fujimura, S.-i. Azuma, N. Aoki, T. Yoshimura, and T. Ito, Growth mechanism of YMnO$_3$ film as a new candidate for nonvolatile memory devices, Journal of Applied Physics **80**, 7084 (1996).

[10] J. Dho, C. W. Leung, J. L. MacManus-Driscoll, and M. G. Blamire, Epitaxial and oriented YMnO$_3$ film growth by pulsed laser deposition, Journal of Crystal Growth **267**, 548 (2004).

[11] X. Martí, F. Sánchez, D. Hrabovsky, J. Fontcuberta, V. Laukhin, V. Skumryev, M. V. García-Cuenca, C. Ferrater, M. Varela, U. Lüders, J. F. Bobo, S. Estradé, J. Arbiol, and F. Peiró, Epitaxial growth of biferroic YMnO$_3$(0 0 0 1) on platinum electrodes, Journal of Crystal Growth **299**, 288 (2007).

[12] S. Imada, S. Shouriki, E. Tokumitsu, and H. Ishiwara, Epitaxial Growth of Ferroelectric YMnO$_3$ Thin Films on Si (111) Substrates by Molecular Beam Epitaxy, Japanese Journal of Applied Physics **37**, 6497 (1998).

[13] S. Cheng, C. Xu, S. Deng, M.-G. Han, S. Bao, J. Ma, C. Nan, W. Duan, L. Bellaiche, Y. Zhu, and J. Zhu, Interface reconstruction with emerging charge ordering in hexagonal manganite, Science Advances **4**, eaar4298 (2018).

[14] S. Imada, T. Kuraoka, E. Tokumitsu, and H. Ishiwara, Ferroelectricity of YMnO$_3$ Thin Films on Pt(111)/Al$_2$O$_3$ (0001) and Pt(111)/Y$_2$O$_3$ (111)/Si(111) Structures Grown by Molecular Beam Epitaxy, Japanese Journal of Applied Physics **40**, 666 (2001).

[15] K. H. Wu, H.-J. Chen, Y. T. Chen, C. C. Hsieh, C. W. Luo, T. M. Uen, J. Y. Juang, J.-Y. Lin, T. Kobayashi, and M. Gospodinov, Marked enhancement of Néel temperature in strained YMnO$_3$ thin films probed by femtosecond spectroscopy, EPL (Europhysics Letters) **94**, 27006 (2011).

[16] C. Dubourdieu, G. Huot, I. Gelard, H. Roussel, O. Lebedev, and G. Van Tendeloo, Thin films and superlattices of multiferroic hexagonal rare earth manganites, Philosophical Magazine Letters **87**, 203 (2007).

[17] V. Laukhin, V. Skumryev, X. Martí, D. Hrabovsky, F. Sánchez, M. V. García-Cuenca, C. Ferrater, M. Varela, U. Lüders, J. F. Bobo, and J. Fontcuberta, Electric-Field Control of Exchange Bias in Multiferroic Epitaxial Heterostructures, Physical Review Letters **97**, 227201 (2006).

[18] T. Kordel, C. Wehrenfennig, D. Meier, T. Lottermoser, M. Fiebig, I. Gélard, C. Dubourdieu, J.-W. Kim, L. Schultz, and K. Dörr, Nanodomains in multiferroic hexagonal RMnO$_3$ films (R=Y,Dy,Ho,Er), Physical Review B **80**, 045409 (2009).

[19] N. Jehanathan, O. Lebedev, I. Gélard, C. Dubourdieu, and G. Van Tendeloo, Structure and defect characterization of multiferroic ReMnO$_3$ films and multilayers by TEM, Nanotechnology **21**, 075705 (2010).

[20] M. Ohring, *The materials science of thin films* (Academic Press, Boston, 1992).

[21] T. Honke, H. Fujioka, J. Ohta, and M. Oshima, InN epitaxial growths on Yttria stabilized zirconia (111) step substrates, Journal of Vacuum Science & Technology A: Vacuum, Surfaces, and Films **22**, 2487 (2004).

[22] M. Fiebig, V. V. Pavlov, and R. V. Pisarev, Second-harmonic generation as a tool for studying electronic and magnetic structures of crystals: review, Journal of the Optical Society of America B **22**, 96 (2005).

[23] S. A. Denev, T. T. A. Lummen, E. Barnes, A. Kumar, and V. Gopalan, Probing Ferroelectrics Using Optical Second Harmonic Generation, Journal of the American Ceramic Society **94**, 2699 (2011).

[24] J. Nordlander, G. De Luca, N. Strkalj, M. Fiebig, and M. Trassin, Probing Ferroic States in Oxide Thin Films Using Optical Second Harmonic Generation, Applied Sciences **8**, 570 (2018).

Inversion-symmetry engineering in sub-unit-cell-layered oxide thin films

E

Inversion-symmetry engineering in sub-unit-cell-layered oxide thin films

J. Nordlander,[1, *] M. D. Rossell,[2] M. Campanini,[2] M. Fiebig,[1] and M. Trassin[1, †]

[1] *Department of Materials, ETH Zurich, CH-8093 Zurich, Switzerland*
[2] *Electron Microscopy Center, Empa, CH-8600 Dübendorf, Switzerland*

Inversion symmetry breaking is a ubiquitous concept in condensed-matter science. On the one hand, it is a prerequisite for many technologically relevant effects such as piezoelectricity, photovoltaic and nonlinear optical properties and spin-transport phenomena. On the other hand, it may determine abstract properties such as the electronic topology in quantum materials. Therefore, the creation of materials where inversion symmetry can be turned on or off by design may be the ultimate route towards controlling parity-related phenomena and functionalities. Here, we engineer the symmetry of ultrathin epitaxial oxide films by sub-unit-cell growth control. We reversibly activate and deactivate inversion symmetry in the layered hexagonal manganites, h-RMnO$_3$ with R = Y, Er, Tb. While an odd number of half-unit-cell layers exhibits a breaking of inversion symmetry through its arrangement of MnO$_5$ bipyramids, an even number of such half-unit-cell layers takes on a centrosymmetric structure. Here we control the resulting symmetry by tracking the growth *in situ* via optical second-harmonic generation. We furthermore demonstrate that our symmetry engineering works independent of the choice of R and even in heterostructures mixing constituents with different R in a two-dimensional growth mode. Symmetry engineering on the atomic level thus suggests a new platform for the controlled activation and deactivation of symmetry-governed functionalities in oxide-electronic epitaxial thin films.

I. INTRODUCTION

According to the fundamental Neumann principle, the symmetry of a material is reflected in its physical properties. Hence, whenever a symmetry is broken, new functionalities arise [1]. A special case is the presence (parity) of or absence (parity breaking) of inversion symmetry, a defining characteristic of a material that governs the emergence of parity-related functionalities. For example, in the field of quantum materials, the conservation or breaking of inversion symmetry distinguishes Dirac from Weyl semimetals [2]. Also many technologically relevant phenomena, like piezoelectricity, photovoltaics and spin-transport effects, depend on a broken inversion symmetry [3–5].

The symmetry of a material may be broken spontaneously. For example, in ferroelectrics, spatial inversion symmetry is lost by the onset of spontaneous polarization, giving rise to the very phenomenon which established their technological relevance: piezoelectricity. However, relying on spontaneous symmetry breaking for enabling functionality in materials lacks control. It would rather be preferable to set the symmetry of a material on demand. Recent progress in materials engineering now allows to achieve inversion-symmetry breaking by design. For example, by combining dissimilar materials to heterostructures, thus disrupting the long-range crystalline order, novel states can be created at the interface between the consituents [6], resulting in phenomena like two-dimensional (2D) superconductivity [7] or emergent magnetic and polar properties [8–10]. In exfoliated 2D materials, the breaking of inversion symmetry on the atomic-monolayer level can lead to a unique electronic band structure [11], valley-selectivity [12], electronic edge-states and nonlinear optical response [13–15].

All this emphasizes the fundamental importance of inversion symmetry – or rather its absence – for functional properties in materials and it highlights the need for deterministic control of inversion-symmetry breaking as a key aspect in state-of-the-art materials engineering. In the vast family of functional oxides, the naturally layered compounds stand out as great candidates for this purpose. In these materials, the unit cell itself is layered, and these layers exhibit a different symmetry than the unit cell in its entity. These sub-unit-cell blocks may therefore locally exhibit properties that are not permitted for the parent material. This aspect has been little explored, however.

Here, we demonstrate symmetry engineering in ultrathin layered oxides, moving repeatedly between centrosymmetric and noncentrosymmetric states, by growth control on the sub-unit-cell level. As our model system, we choose the hexagonal manganites, h-RMnO$_3$ (R = Y, Er, Tb), because of their naturally layered structure. We deposit dielectric h-RMnO$_3$ in a layer-by-layer fashion, where each layer is only half a unit cell in height. Using in-situ optical second harmonic generation (ISHG), we probe the symmetry of the films during deposition [16, 17]. We reveal that while an even number of half-unit-cell layers retain the inversion symmetry of the parent material, an odd number of these layers breaks parity because of the locally noncentrosymmetric MnO$_5$ sublattice within each half-unit-cell block. The parity-sensitive ISHG response follows this alternating symmetry in real time and allows us to set the symmetry state of the thin film system on demand, here within a thickness range of less than 6 Å. By expanding from a single constituent to (R'MnO$_3$)/(R''MnO$_3$) superlattices we show that this
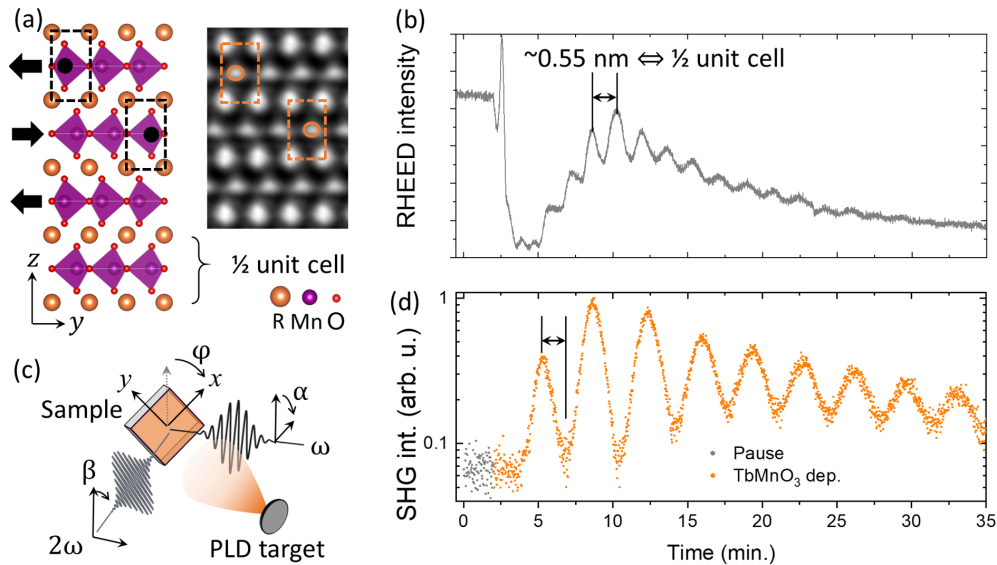
FIG. 1. (a) Prototype crystal structure of the h-RMnO$_3$ family and STEM image from a h-YMnO$_3$ film. The noncentrosymmetric structure of each half-unit-cell layer and their alternating orientation are highlighted by dashed boxes. (b) RHEED intensity oscillations indicate a layer-by-layer growth mode with each layer representing half of unit cell. (c) Experimental ISHG setup. The sample is probed in a reflection geometry in the PLD growth chamber during deposition and with simultaneous RHEED monitoring. The angle of polarization of the fundamental (ω) and the SHG (2ω) light are given by α and β, respectively. The azimuthal angle φ denotes the orientation of the sample x axis with respect to the laboratory vertical axis. (d) ISHG intensity during deposition of 10 nm (9 unit cells) of h-TbMnO$_3$ detected at $(\alpha, \beta) = (90°, 120°)$. Calibration by the RHEED data reveals a periodicity of the ISHG intensity oscillations of 1 unit cell.

phenomenon continues across the interface between constituents, independent of R. With our work, we thus establish layered oxides as a class of materials for exerting inversion-symmetry control and its functionalization in ultrathin epitaxial films.

II. RESULTS

The h-RMnO$_3$ thin films were grown by pulsed laser deposition on (111)-oriented yttria-stabilized zirconia (YSZ) substrates. Their crystal structure is shown in Fig. 1(a). While the h-RMnO$_3$ compounds are usually found in a noncentrosymmetric improper ferroelectric phase, a suppression of the polar mode in the ultrathin regime places the system in the paraelectric phase during the epitaxial deposition [18]. In this phase, the unit cell is centrosymmetric and belongs to the point group $6/mmm$. It consists, however, of two identical noncentrosymmetric half-unit-cell layers rotated by 60° with respect to each other. The symmetry of these is $\bar{6}m2$ because of the trigonal structure of the MnO$_5$ sublattice [19].

For the epitaxial thin films grown by PLD, in-situ reflection high-energy electron diffraction (RHEED) intensity oscillations and post-deposition thickness analysis by x-ray reflectivity indicate a layer-by-layer growth mode where each layer corresponds to half a unit cell in height [Fig. 1(b)]. Therefore, through precise growth control, either a centrosymmetric state (even number of half-unit-

cell layers) or a noncentrosymmetric state (odd number of half-unit-cell layers) should be obtained.

We begin by verifying the symmetry of the half-unit-cell layers in h-TbMnO$_3$ films. To access and control the thin-film properties in real time, we use ISHG during the thin-film synthesis. This symmetry-sensitive technique allows to probe functional properties in thin films remotely and directly, as they emerge during growth. The experimental setup is sketched in Fig. 1(c). SHG is a nonlinear optical process which describes the frequency doubling of light in a material. In the electric-dipole approximation, it is described as

$$P_i(2\omega) = \epsilon_0 \chi^{(2)}_{ijk} E_j(\omega) E_k(\omega), \quad (1)$$

where $E_{j,k}(\omega)$ are the electric-field components of the incident fundamental beam and $P_i(2\omega)$ denotes the resulting nonlinear polarization in the material which acts as source for the emitted SHG light. The process is parametrized by the second-order susceptibility tensor, $\chi^{(2)}$. The simultaneous monitoring of RHEED and ISHG intensity allows us to correlate the symmetry properties of the thin film with its thickness and growth mode [16].

The real-time evolution of the ISHG signal while half-unit-cell layers are added one-by-one during the deposition of h-TbMnO$_3$ on YSZ is shown in Fig. 1(d). A periodic modulation of the ISHG signal is observed where the intensity oscillates with a period of one unit cell. For
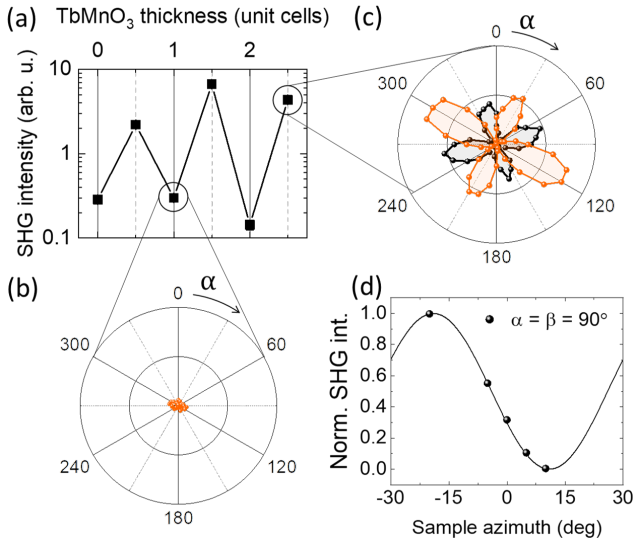
FIG. 2. (a) SHG intensity at $(\alpha, \beta) = (120°, 90°)$ vs. layer thickness in a h-TbMnO$_3$ film at the growth temperature. Minima and maxima as in Fig. 1(d) are reproduced. (b,c) Dependence of the SHG intensity for varying angle α and fixed angle β at 0° (black) and 90° (orange) is shown for (b) an even and (c) an odd number of half-unit-cell layers of h-TbMnO$_3$. (b) and (c) are plotted to the same scale. Because of inversion symmetry, no SHG is detected in (b). The polarization dependence in (c) is compatible with contributions from the nonlinear susceptibility components permitted by the $\bar{6}m2$ point symmetry of the half unit cell. We attribute the slight asymmetry between the four lobes in (c) to the azimuthally varying reflectivity with the 90° reflection geometry of the ISHG setup. (d) Dependence of half-unit-cell SHG intensity at $\alpha = \beta = 90°$ on the azimuthal orientation φ of the sample. The 60° periodicity of the data further supports the $\bar{6}m2$ point group

an even number of half-unit-cell layers, no SHG is detected. In contrast, an odd number of half-unit-cell layers results in a sizeable SHG intensity. Strikingly, the RHEED signal oscillates twice as fast as the SHG signal and therefore reveals the same surface morphology in both cases. This directly excludes surface-morphology-related effects, such as a step density variation during the layer-by-layer growth [20], as possible origin of the ISHG modulation. Instead, we attribute this modulation to the alternating symmetry of the film that occurs with the deposition of each half-unit-cell layer, as described above.

To verify this hypothesis, we analyze the polarization properties of the SHG signal (Fig. 2). The the SHG response for an even and an odd number of half-unit-cell layers are shown in Figs. 2(b) and (c), respectively. The four-lobed symmetry seen for 2.5 unit cells in Fig. 2(c) is compatible with the proposed $\bar{6}m2$ point group of a half-unit-cell layer, where the allowed $\chi^{(2)}$ components in Eq. 1 are [21]: $\chi_{yyy} = -\chi_{yxx} = -\chi_{xxy} = -\chi_{xyx}$, with x lying parallel to the crystallographic a axis. As seen
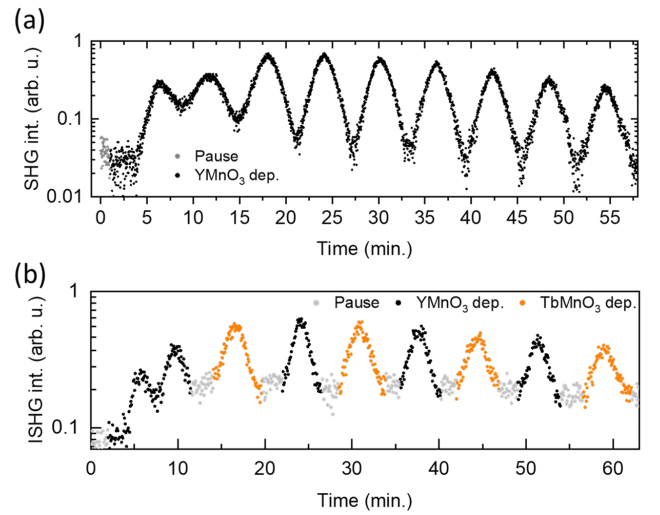

FIG. 3. ISHG intensity during h-RMnO$_3$ deposition of (a) h-YMnO$_3$ and (b) a (h-YMnO$_3$)$_1$/(h-TbMnO$_3$)$_1$ superlattice. In both cases, the measurements correspond to 10 nm (9 unit cells) of thin-film deposition and the ISHG intensity is modulated with a period of one unit cell.

in Fig. 2(d)), the relation of the SHG signal to the trigonal half-unit-cell lattice is further supported by the 60° periodicity the SHG intensity with respect to rotation of sample around its z-axis. Here, the SHG source term for the point group $\bar{6}m2$ dictates $P^{(2\omega)} \propto \cos(3\phi)\chi^{(2)}$.

Given the polarization-independent absence of SHG for even numbers of half-unit-cell layers [Fig. 2(b)], we conclude, that the ISHG intensity oscillations seen in Fig. 1(d) are due to destructive interference of identical antiphase SHG waves from two adjacent half-unit-cell layers, where the antiphase relation comes from their relative 60° rotation, yielding a prefactor $\cos(3 \cdot 60°) = -1$ between the respective SHG source terms. Macroscopically, this destructive interference is in line with the vanishing $\chi^{(2)}$ tensor for the non-polar $6/mmm$ point group of the full unit cell. Following the ISHG response during growth hence follows the alternating breaking and restoration of inversion symmetry with the deposition of each additional half-unit-cell layer.

So far, we have restricted our discussion to h-RMnO$_3$ films with R = Tb. In order to determine the influence of R, we now expand our investigations towards other h-RMnO$_3$ compounds. Figure 3(a) shows that the ISHG oscillations are observed also for the half-unit-cell by half-unit-cell deposition of h-YMnO$_3$ thin films. But even when we combine h-YMnO$_3$ and h-TbMnO$_3$ into a (h-YMnO$_3$)$_1$/(h-TbMnO$_3$)$_1$ superlattice, we find that the the ISHG intensity oscillation prevails (Fig. 3(b)). SHG from the two compounds interferes in the same way as for the single layers and at comparable oscillation amplitudes. Hence, we can conclude that the SHG signal observed here does not originate in the R-ion layer of the compound, as the signal is clearly independent of the R-
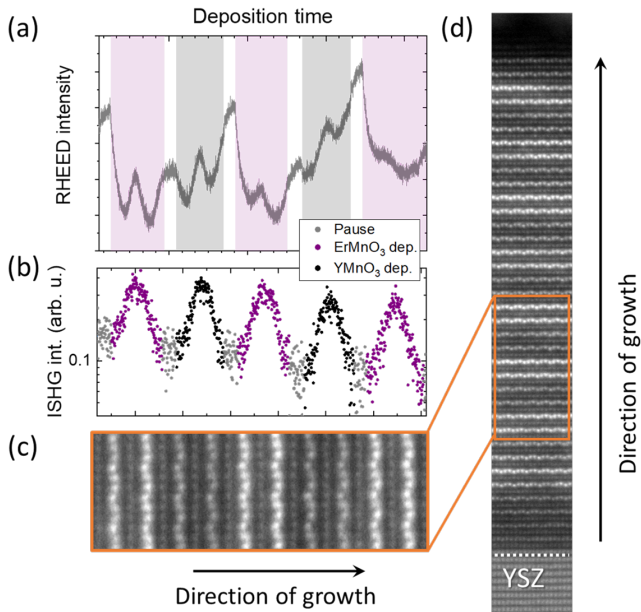
FIG. 4. (a,b) Simultaneously measured in-situ RHEED and SHG intensities during growth of a $(h-YMnO_3)_1/(h-ErMnO_3)_1$ superlattice. (c,d) HAADF STEM confirms atomically sharp interfaces. Note that the heavier Er atoms appear brighter than Y atoms. Further note that the periodic displacement of the R-ions along the c-axis indicates the occurrence of ferroelectric polarization in this superlattice. Its presence or absence is another aspect that can be growth-controlled by epitaxial constraints [18].

ion species. Instead, it originates from the MnO_5 trigonal bipyramid layers uniform to all $h-RMnO_3$ compounds.

In the comparison of the data obtained by RHEED and ISHG, it is important to note that the former probes the structural integrity of a sample surface, whereas the latter senses the symmetry of the crystal lattice. We therefore find complementary information by combining the two in-situ methods, where RHEED contributes surface-morphology information and ISHG reveals the symmetry-related functionality of a specimen in real time. In particular, in the case of crystallographic defects or growth-mode variations, there can be a discrepancy between the smoothest surface (local maximum for RHEED intensity) and a defined symmetry state (local minimum or maximum for ISHG), which would manifest as a phase shift between the RHEED and the SHG oscillations. Therefore, a surface-roughness-controlled heterostructure may not necessarily be the same as a symmetry-controlled heterostructure. On the other hand, by achieving a synchronization of both surface and symmetry variations, through a synchronization of the RHEED and ISHG oscillations, we can combine the two techniques towards the design of symmetry-controlled interfaces with minimal interface roughness.

To demonstrate this, we combined hexagonal $YMnO_3$ and $ErMnO_3$ by growing a $(h-YMnO_3)_1/(h-ErMnO_3)_1$

superlattice. The choice of pairing $YMnO_3$ with $ErMnO_3$ is motivated by their excellent mutual lattice matching. This increases our chances to maintain a layer-by-layer growth mode with smooth interfaces during the deposition of the heterostructure. Figure 4 shows the simultaneous monitoring of RHEED and ISHG during growth of the $(h-YMnO_3)_1/(h-ErMnO_3)_1$ superlattice, where we see that the respective signal oscillations are in phase. At the completion of each layer, i.e., at each RHEED maximum, we find either a maximum or minimum in the ISHG signal. This indicates that the point during growth corresponding to a completely centrosymmetric state, also corresponds to the one with the flattest surface. We verify the expected high quality of this symmetry-controlled interface at the atomic scale using high-angle annular dark-field scanning transmission electron microscopy (HAADF-STEM). Due to the difference in atomic number for Y and Er, the two materials can be clearly distinguished in the images. This reveals perfect alternation of Y and Er layers in the heterostructure. Thus, we not only verify the coveted two-dimensional growth mode but we also confirm that no intermixing at the atomic scale occurs. The synchronization of both surface and symmetry state during thin-film deposition thereby enables the design of heterostructures with sharp interfaces and well-defined symmetry properties, which in turn opens up for deterministic control of functionality at the atomic scale.

III. CONCLUSION

In conclusion, we have demonstrated the use of a sub-unit-cell growth mode in layered oxides for deterministic control of the resulting symmetry. Using the hexagonal manganites, $h-RMnO_3$, as model system, we select a centrosymmetric or noncentrosymmetric state of the system within the deposition of only a half-unit-cell layer. This control is enabled by the inherent noncentrosymmetry of the individual half-unit-cell layers, such that an odd number of these breaks inversion symmetry, while an even number preserves it. We have further shown that this symmetry alternation prevails in superlattices composed of different $h-RMnO_3$ and is independent of our choice of R-ions. We emphasize that the emergence of symmetry-breaking functionalities at the sub-unit-cell level is not at all limited to the $h-RMnO_3$ system. In fact, we expect similar properties in any layered material grown by sub-unit-cell layers with reduced local symmetry. In expanding beyond the aspect of inversion symmetry, we also point out that this sub-unit-cell control can be used to alternate the presence and absence of other parity-like properties like chirality, magnetic reciprocity etc. Thus, tracking and controlling thin-film oxide growth on the sub-unit-cell level has the potential to open up a new route for tailoring symmetry and coercing novel functionality in the ultrathin regime.

[1] M. Livio, Physics: Why symmetry matters, Nature **490**, 472 (2012).

[2] N. P. Armitage, E. J. Mele, and A. Vishwanath, Weyl and Dirac semimetals in three-dimensional solids, Reviews of Modern Physics **90**, 015001 (2018).

[3] S. Trolier-McKinstry and P. Muralt, Thin Film Piezoelectrics for MEMS, Journal of Electroceramics **12**, 7 (2004).

[4] V. M. Fridkin, Bulk photovoltaic effect in noncentrosymmetric crystals, Crystallography Reports **46**, 654 (2001).

[5] F. Hellman et al., Interface-induced phenomena in magnetism, Reviews of Modern Physics **89**, 025006 (2017).

[6] H. Y. Hwang, Y. Iwasa, M. Kawasaki, B. Keimer, N. Nagaosa, and Y. Tokura, Emergent phenomena at oxide interfaces, Nature Materials **11**, 103 (2012).

[7] A. Ohtomo and H. Hwang, A high-mobility electron gas at the $LaAlO_3/SrTiO_3$ heterointerface, Nature **427**, 423 (2004).

[8] N. Sai, B. Meyer, and D. Vanderbilt, Compositional inversion symmetry breaking in ferroelectric perovskites, Physical Review Letters **84**, 5636 (2000).

[9] H. N. Lee, H. M. Christen, M. F. Chisholm, C. M. Rouleau, and D. H. Lowndes, Strong polarization enhancement in asymmetric three-component ferroelectric superlattices, Nature **433**, 395 (2005).

[10] C. Becher, M. Trassin, M. Lilienblum, C. T. Nelson, S. J. Suresha, D. Yi, P. Yu, R. Ramesh, M. Fiebig, and D. Meier, Functional ferroic heterostructures with tunable integral symmetry, Nature Communications **5**, 4295 (2014).

[11] K. F. Mak, C. Lee, J. Hone, J. Shan, and T. F. Heinz, Atomically thin MoS_2: A new direct-gap semiconductor, Physical Review Letters **105**, 136805 (2010).

[12] W. Yao, D. Xiao, and Q. Niu, Valley-dependent optoelectronics from inversion symmetry breaking, Physical Review B **77**, 235406 (2008).

[13] N. Kumar, S. Najmaei, Q. Cui, F. Ceballos, P. M. Ajayan, J. Lou, and H. Zhao, Second harmonic microscopy of monolayer MoS_2, Physical Review B **87**, 161403 (2013).

[14] W.-T. Hsu, Z.-A. Zhao, L.-J. Li, C.-H. Chen, M.-H. Chiu, P.-S. Chang, Y.-C. Chou, and W.-H. Chang, Second harmonic generation from artificially stacked transition metal dichalcogenide twisted bilayers, ACS Nano **8**, 2951 (2014).

[15] X. Yin, Z. Ye, D. A. Chenet, Y. Ye, K. O'Brien, J. C. Hone, and X. Zhang, Edge nonlinear optics on a MoS_2 atomic monolayer, Science **344**, 488 (2014).

[16] G. De Luca, N. Strkalj, S. Manz, C. Bouillet, M. Fiebig, and M. Trassin, Nanoscale design of polarization in ultrathin ferroelectric heterostructures, Nature Communications **8**, 1419 (2017).

[17] J. Nordlander, G. De Luca, N. Strkalj, M. Fiebig, and M. Trassin, Probing Ferroic States in Oxide Thin Films Using Optical Second Harmonic Generation, Applied Sciences **8**, 570 (2018).

[18] J. Nordlander, M. Campanini, M. D. Rossell, R. P. Erni, Q. N. Meier, A. Cano, N. A. Spaldin, M. Fiebig, and M. Trassin, The ultrathin limit of improper ferroelectricity, Nature Communications **10**, 5591 (2019).

[19] C. Degenhardt, M. Fiebig, D. Fröhlich, T. Lottermoser, and R. V. Pisarev, Nonlinear optical spectroscopy of electronic transitions in hexagonal manganites, Applied Physics B **73**, 139 (2001).

[20] V. Jähnke, U. Conrad, J. Güdde, and E. Matthias, SHG investigations of the magnetization of thin Ni and Co films on Cu(001), Applied Physics B: Lasers and Optics **68**, 485 (1999).

[21] R. R. Birss, *Symmetry and magnetism*, Vol. 863 (North-Holland Pub. Co., 1964).

Glossary

AFM atomic force microscopy

BF bright field

ED electric dipole

HAADF high-angle annular dark field

ISHG in-situ second harmonic generation

PFM piezo-response force microscopy

PLD pulsed laser deposition

RHEED reflection high-energy electron diffraction

RSM reciprocal space mapping

SPM scanning probe microscopy

STEM scanning transmission electron microscopy

XRD x-ray diffraction

Bibliography

[1] H. Goesmann and C. Feldmann. Nanoparticulate Functional Materials. *Angewandte Chemie International Edition* **49,** 1362 (2010).

[2] J. Schröder and D. C. Lupascu. *Ferroic Functional Materials*. Springer International Publishing, 2018.

[3] A. Zunger. Inverse design in search of materials with target functionalities. *Nature Reviews Chemistry* **2,** 0121 (2018).

[4] G.-H. Lee et al. Multifunctional materials for implantable and wearable photonic healthcare devices. *Nature Reviews Materials* **5,** 149 (2020).

[5] G. Song, N. Ma, and H.-N. Li. Applications of shape memory alloys in civil structures. *Engineering Structures* **28,** 1266 (2006).

[6] D. Dimov et al. Ultrahigh Performance Nanoengineered Graphene-Concrete Composites for Multifunctional Applications. *Advanced Functional Materials* **28,** 1705183 (2018).

[7] I. P. Parkin and R. G. Palgrave. Self-cleaning coatings. *Journal of Materials Chemistry* **15,** 1689 (2005).

[8] V. A. Ganesh, H. K. Raut, A. S. Nair, and S. Ramakrishna. A review on self-cleaning coatings. *Journal of Materials Chemistry* **21,** 16304 (2011).

[9] G. J. Snyder and E. S. Toberer. Complex thermoelectric materials. *Nature Materials* **7,** 105 (2008).

[10] A. Seeboth, D. Lötzsch, R. Ruhmann, and O. Muehling. Thermochromic Polymers—Function by Design. *Chemical Reviews* **114,** 3037 (2014).

[11] S. Han et al. Thermoelectric Polymer Aerogels for Pressure-Temperature Sensing Applications. *Advanced Functional Materials* **27,** 1703549 (2017).

[12] P. Peterson et al. Practical Use of Metal Oxide Semiconductor Gas Sensors for Measuring Nitrogen Dioxide and Ozone in Urban Environments. *Sensors* **17,** 1653 (2017).

[13] S. Lien, D. Wuu, W. Yeh, and J. Liu. Tri-layer antireflection coatings (SiO_2/SiO_2–TiO_2/TiO_2) for silicon solar cells using a sol–gel technique. *Solar Energy Materials and Solar Cells* **90,** 2710 (2006).

[14] P. K. Nayak, S. Mahesh, H. J. Snaith, and D. Cahen. Photovoltaic solar cell technologies: analysing the state of the art. *Nature Reviews Materials* **4,** 269 (2019).

[15] J. Hillenbrand and G. M. Sessler. High-sensitivity piezoelectric microphones based on stacked cellular polymer films (L). *The Journal of the Acoustical Society of America* **116,** 3267 (2004).

[16] M. Yip, R. Jin, H. H. Nakajima, K. M. Stankovic, and A. P. Chandrakasan. A Fully-Implantable Cochlear Implant SoC With Piezoelectric Middle-Ear Sensor and Arbitrary Waveform Neural Stimulation. *IEEE Journal of Solid-State Circuits* **50,** 214 (2015).

[17] S. S. Zhang. A review on electrolyte additives for lithium-ion batteries. *Journal of Power Sources* **162,** 1379 (2006).

[18] G. Wang, X. Shen, J. Yao, and J. Park. Graphene nanosheets for enhanced lithium storage in lithium ion batteries. *Carbon* **47,** 2049 (2009).

[19] F. Cheng, J. Liang, Z. Tao, and J. Chen. Functional Materials for Rechargeable Batteries. *Advanced Materials* **23,** 1695 (2011).

[20] O. Auciello, J. F. Scott, and R. Ramesh. The Physics of Ferroelectric Memories. *Physics Today* **51,** 22 (1998).

[21] H. Ishiwara. Ferroelectric Random Access Memories. *Journal of Nanoscience and Nanotechnology* **12,** 7619 (2012).

[22] L. K. Baxter. *Capacitive Sensors.* John Wiley Sons, 1996.

[23] R. Ramesh and D. G. Schlom. Whither Oxide Electronics? *MRS Bulletin* **33,** 1006 (2008).

[24] J. Mannhart and D. G. Schlom. Oxide Interfaces–An Opportunity for Electronics. *Science* **327,** 1607 (2010).

[25] H. Y. Hwang et al. Emergent phenomena at oxide interfaces. *Nature Materials* **11,** 103 (2012).

[26] M. Coll et al. Towards Oxide Electronics: a Roadmap. *Applied Surface Science* **482,** 1 (2019).

[27] S. D. Ha and S. Ramanathan. Adaptive oxide electronics: A review. *Journal of Applied Physics* **110,** 071101 (2011).

[28] J. Grollier et al. Neuromorphic spintronics. *Nature Electronics,* (2020).

[29] S. Abel et al. A Hybrid Barium Titanate–Silicon Photonics Platform for Ultraefficient Electro-Optic Tuning. *Journal of Lightwave Technology* **34,** 1688 (2016).

[30] J. Schaab et al. Electrical half-wave rectification at ferroelectric domain walls. *Nature Nanotechnology* **13,** 1028 (2018).

[31] C. N. R. Rao. Transition Metal Oxides. *Annual Review of Physical Chemistry* **40,** 291 (1989).

[32] Y. Tokura and N. Nagaosa. Orbital Physics in Transition-Metal Oxides. *Science* **288,** 462 (2000).

[33] E. Dagotto. Complexity in Strongly Correlated Electronic Systems. *Science* **309,** 257 (2005).

[34] S. Gariglio, N. Reyren, A. D. Caviglia, and J.-M. Triscone. Superconductivity at the $LaAlO_3/SrTiO_3$ interface. *Journal of Physics: Condensed Matter* **21,** 164213 (2009).

[35] J. A. Bert et al. Direct imaging of the coexistence of ferromagnetism and superconductivity at the $LaAlO_3/SrTiO_3$ interface. *Nature Physics* **7,** 767 (2011).

[36] S. Royer and D. Duprez. Catalytic Oxidation of Carbon Monoxide over Transition Metal Oxides. *ChemCatChem* **3,** 24 (2010).

[37] S. Jin et al. Thousandfold Change in Resistivity in Magnetoresistive La-Ca-Mn-O Films. *Science* **264,** 413 (1994).

[38] R. R. Birss. *Symmetry and magnetism.* Vol. 863. North-Holland Pub. Co., 1964.

[39] P. S. Halasyamani and K. R. Poeppelmeier. Noncentrosymmetric Oxides. *Chemistry of Materials* **10,** 2753 (1998).

[40] J. A. Sulpizio, S. I., P. Irvin, and J. Levy. Nanoscale Phenomena in Oxide Heterostructures. *Annual Review of Materials Research* **44,** 117 (2014).

[41] L. W. Martin, Y.-H. Chu, and R. Ramesh. Advances in the growth and characterization of magnetic, ferroelectric, and multiferroic oxide thin films. *Materials Science and Engineering: R: Reports* **68,** 89 (2010).

[42] N. Setter et al. Ferroelectric thin films: Review of materials, properties, and applications. *Journal of Applied Physics* **100,** 051606 (2006).

[43] L. W. Martin and A. M. Rappe. Thin-film ferroelectric materials and their applications. *Nature Reviews Materials* **2,** 16087 (2017).

[44] J. Nordlander, G. De Luca, N. Strkalj, M. Fiebig, and M. Trassin. Probing Ferroic States in Oxide Thin Films Using Optical Second Harmonic Generation. *Applied Sciences* **8,** 570 (2018).

[45] V. M. Fridkin. Bulk photovoltaic effect in noncentrosymmetric crystals. *Crystallography Reports* **46,** 654 (2001).

[46] M. Z. Hasan and C. L. Kane. Colloquium: Topological insulators. *Reviews of Modern Physics* **82,** 3045 (2010).

[47] N. P. Armitage, E. J. Mele, and A. Vishwanath. Weyl and Dirac semimetals in three-dimensional solids. *Reviews of Modern Physics* **90,** 015001 (2018).

[48] S. Trolier-McKinstry and P. Muralt. Thin Film Piezoelectrics for MEMS. *Journal of Electroceramics* **12,** 7 (2004).

[49] V. Wadhawan. *Introduction to ferroic materials*. CRC press, 2000.

[50] J. C. Tolédano and P. Tolédano. *The Landau theory of phase transitions: application to structural, incommensurate, magnetic, and liquid crystal systems*. World Scientific Publishing Company, 1987.

[51] A. P. Levanyuk and D. G. Sannikov. Improper ferroelectrics. *Soviet Physics Uspekhi* **17,** 199 (1974).

[52] J. F. Scott and C. A. Paz de Araujo. Ferroelectric Memories. *Science* **246,** 1400 (1989).

[53] G. H. Haertling. Ferroelectric Ceramics: History and Technology. *Journal of the American Ceramic Society* **82,** 797 (1999).

[54] J. F. Scott. Applications of Modern Ferroelectrics. *Science* **315,** 954 (2007).

[55] S. Mathews, R. Ramesh, T. Venkatesan, and J. Benedetto. Ferroelectric field effect transistor based on epitaxial perovskite heterostructures. *Science* **276,** 238 (1997).

[56] J. F. Scott. Nanoferroelectrics: statics and dynamics. *Journal of Physics: Condensed Matter* **18,** R361 (2006).

[57] E. Y. Tsymbal and H. Kohlstedt. Tunneling across a ferroelectric. *Science* **313,** 181 (2006).

[58] J. Seidel et al. Conduction at domain walls in oxide multiferroics. *Nature Materials* **8,** 229 (2009).

[59] G. Catalan, J. Seidel, R. Ramesh, and J. F. Scott. Domain wall nanoelectronics. *Reviews of Modern Physics* **84,** 119 (2012).

[60] J. A. Mundy et al. A high-energy density antiferroelectric made by interfacial electrostatic engineering**,** ArXiv:1812.09615 (2018).

[61] S. M. Yang et al. Mixed electrochemical–ferroelectric states in nanoscale ferroelectrics. *Nature Physics* **13,** 812 (2017).

[62] D. D. Fong et al. Ferroelectricity in Ultrathin Perovskite Films. *Science* **304,** 1650 (2004).

[63] J. Junquera and P. Ghosez. Critical thickness for ferroelectricity in perovskite ultrathin films. *Nature* **422,** 506 (2003).

[64] N. Sai, A. M. Kolpak, and A. M. Rappe. Ferroelectricity in ultrathin perovskite films. *Physical Review B* **72,** 020101 (2005).

[65] C. Lichtensteiger, S. Fernandez-Pena, C. Weymann, P. Zubko, and J.-M. Triscone. Tuning of the Depolarization Field and Nanodomain Structure in Ferroelectric Thin Films. *Nano Letters* **14,** 4205 (2014).

[66] A. K. Yadav et al. Observation of polar vortices in oxide superlattices. *Nature* **530,** 198 (2016).

[67] A. Ohtomo and H. Y. Hwang. A high-mobility electron gas at the LaAlO$_3$ / SrTiO$_3$ heterointerface. *Nature* **427,** 423 (2004).

[68] M. Ohring. *The materials science of thin films*. Boston: Academic Press, 1992.

[69] D. G. Schlom, L.-Q. Chen, X. Pan, A. Schmehl, and M. A. Zurbuchen. A Thin Film Approach to Engineering Functionality into Oxides. *Journal of the American Ceramic Society* **91,** 2429 (2008).

[70] T. H. Kim et al. Polar metals by geometric design. *Nature* **533,** 68 (2016).

[71] O. Y. Gorbenko, S. V. Samoilenkov, I. E. Graboy, and A. R. Kaul. Epitaxial Stabilization of Oxides in Thin Films. *Chemistry of Materials* **14,** 4026 (2002).

[72] N. Strkalj, E. Gradauskaite, J. Nordlander, and M. Trassin. Design and Manipulation of Ferroic Domains in Complex Oxide Heterostructures. *Materials* **12,** 3108 (2019).

[73] D. G. Schlom et al. Strain Tuning of Ferroelectric Thin Films. *Annual Review of Materials Research* **37,** 589 (2007).

[74] K. J. Choi et al. Enhancement of ferroelectricity in strained BaTiO$_3$ thin films. *Science* **306,** 1005 (2004).

[75] N. Strkalj et al. Depolarizing-Field Effects in Epitaxial Capacitor Heterostructures. *Physical Review Letters* **123,** 147601 (2019).

[76] Y. R. Shen. *The principles of nonlinear optics*. Wiley classics library. Wiley-Interscience, 2003.

[77] R. Boyd. *Nonlinear Optics, 3rd Edition*. Amsterdam Boston: Academic Press, 2008.

[78] G. De Luca et al. Nanoscale design of polarization in ultrathin ferroelectric heterostructures. *Nature Communications* **8,** 1419 (2017).

[79] W. P. Mason and B. T. Matthias. Theoretical Model for Explaining the Ferroelectric Effect in Barium Titanate. *Physical Review* **74,** 1622 (1948).

[80] Y. Xu. *Ferroelectric materials and their applications*. Amsterdam New York New York, NY, USA: North-Holland Pub. Co., 1991.

[81] C. Beekman et al. Phase Transitions, Phase Coexistence, and Piezoelectric Switching Behavior in Highly Strained BiFeO$_3$ Films. *Advanced Materials* **25,** 5561 (2013).

[82] H.-J. Liu et al. Strain-driven phase boundaries in $BiFeO_3$ thin films studied by atomic force microscopy and x-ray diffraction. *Physical Review B* **85,** 014104 (2012).

[83] A. R. Damodaran, S. Lee, J. Karthik, S. MacLaren, and L. W. Martin. Temperature and thickness evolution and epitaxial breakdown in highly strained $BiFeO_3$ thin films. *Physical Review B* **85,** 024113 (2012).

[84] S. Abel et al. Large Pockels effect in micro-and nanostructured barium titanate integrated on silicon. *Nature Materials* **18,** 42 (2019).

[85] J. Wang et al. Epitaxial $BiFeO_3$ Multiferroic Thin Film Heterostructures. *Science* **299,** 1719 (2003).

[86] D. Lebeugle et al. Room-temperature coexistence of large electric polarization and magnetic order in $BiFeO_3$ single crystals. *Physical Review B* **76,** 024116 (2007).

[87] C. Ederer and N. A. Spaldin. Weak ferromagnetism and magnetoelectric coupling in bismuth ferrite. *Physical Review B* **71,** 060401 (2005).

[88] J. T. Heron et al. Deterministic switching of ferromagnetism at room temperature using an electric field. *Nature* **516,** 370 (2014).

[89] R. J. Zeches et al. A Strain-Driven Morphotropic Phase Boundary in $BiFeO_3$. *Science* **326,** 977 (2009).

[90] J. X. Zhang et al. Microscopic origin of the giant ferroelectric polarization in tetragonal-like $BiFeO_3$. *Physical Review Letters* **107,** 147602 (2011).

[91] P. Sharma et al. Optimizing the electromechanical response in morphotropic $BiFeO_3$. *Nanotechnology* **29,** 205703 (2018).

[92] B. B Van Aken, T. T. M. Palstra, A. Filippetti, and N. A Spaldin. The origin of ferroelectricity in magnetoelectric $YMnO_3$. *Nature Materials* **3,** 164 (2004).

[93] M. Lilienblum et al. Ferroelectricity in the multiferroic hexagonal manganites. *Nature Physics* **11,** 1070 (2015).

[94] S. C. Chae et al. Direct Observation of the Proliferation of Ferroelectric Loop Domains and Vortex-Antivortex Pairs. *Physical Review Letters* **108,** 167603 (2012).

[95] M. E. Holtz et al. Topological Defects in Hexagonal Manganites: Inner Structure and Emergent Electrostatics. *Nano Letters* **17,** 5883 (2017).

[96] S. Artyukhin, K. T. Delaney, N. A. Spaldin, and M. Mostovoy. Landau theory of topological defects in multiferroic hexagonal manganites. *Nature Materials* **13,** 42 (2013).

[97] T. Jungk, Á. Hoffmann, M. Fiebig, and E. Soergel. Electrostatic topology of ferroelectric domains in $YMnO_3$. *Applied Physics Letters* **97,** 12904 (2010).

[98] T. Choi et al. Insulating interlocked ferroelectric and structural antiphase domain walls in multiferroic $YMnO_3$. *Nature Materials* **9,** 253 (2010).

[99] D. Meier et al. Anisotropic conductance at improper ferroelectric domain walls. *Nature Materials* **11,** 284 (2012).

[100] J. A. Mundy et al. Functional electronic inversion layers at ferroelectric domain walls. *Nature Materials* **16,** 622 (2017).

[101] B. Lorenz. Hexagonal Manganites—($RMnO_3$): Class (I) Multiferroics with Strong Coupling of Magnetism and Ferroelectricity. *ISRN Condensed Matter Physics* **2013,** 497073 (2013).

[102] Ch. Tzschaschel, T. Satoh, and M. Fiebig. Tracking the ultrafast motion of an antiferromagnetic order parameter. *Nature Communications* **10,** 3995 (2019).

[103] N. A Hill. Why Are There so Few Magnetic Ferroelectrics? *The Journal of Physical Chemistry B* **104,** 6694 (2000).

[104] M. Fiebig, Th. Lottermoser, D. Fröhlich, A. V. Goltsev, and R. V. Pisarev. Observation of coupled magnetic and electric domains. *Nature* **419,** 818 (2002).

[105] N. Sai, C. J. Fennie, and A. A. Demkov. Absence of Critical Thickness in an Ultrathin Improper Ferroelectric Film. *Physical Review Letters* **102,** 107601 (2009).

[106] D. B. Chrisey and G. K. Hubler. *Pulsed laser deposition of thin films*. Wiley New York, 1994.

[107] G. J. H. M. Rijnders, G. Koster, D. H. A. Blank, and H. Rogalla. In situ monitoring during pulsed laser deposition of complex oxides using reflection high energy electron diffraction under high oxygen pressure. *Applied Physics Letters* **70,** 1888 (1997).

[108] R. Eason. *Pulsed laser deposition of thin films: applications-led growth of functional materials*. John Wiley & Sons, 2007.

[109] P. J. Kelly and R. D. Arnell. Magnetron sputtering: A review of recent developments and applications. *Vacuum* **56,** 159 (2000).

[110] Mario Birkholz. *Thin Film Analysis by X-Ray Scattering*. Wiley, 2005.

[111] S. V. Kalinin and A. Gruverman. *Scanning probe microscopy: electrical and electromechanical phenomena at the nanoscale*. Vol. 1. Springer Science & Business Media, 2007.

[112] S. J. Pennycook and P. D. Nellist. *Scanning transmission electron microscopy: imaging and analysis*. Springer Science & Business Media, 2011.

[113] R. Erni. *Aberration-corrected imaging in transmission electron microscopy: An introduction*. World Scientific, 2010.

[114] R. Smith. Theory of intracavity optical second-harmonic generation. *IEEE Journal of Quantum Electronics* **6,** 215 (1970).

[115] R. M. Corn and D. A. Higgins. Optical second harmonic generation as a probe of surface chemistry. *Chemical Reviews* **94,** 107 (1994).

[116] G. Lüpke. Characterization of semiconductor interfaces by second-harmonic generation. *Surface Science Reports* **35,** 75 (1999).

[117] M. Fiebig, V. V. Pavlov, and R. V. Pisarev. Second-harmonic generation as a tool for studying electronic and magnetic structures of crystals: review. *Journal of the Optical Society of America B* **22,** 96 (2005).

[118] S. A. Denev, T. T. A. Lummen, E. Barnes, A. Kumar, and V. Gopalan. Probing Ferroelectrics Using Optical Second Harmonic Generation. *Journal of the American Ceramic Society* **94,** 2699 (2011).

[119] S. H. Wemple, M. Didomenico, and I. Camlibel. Dielectric and optical properties of melt-grown $BaTiO_3$. *Journal of Physics and Chemistry of Solids* **29,** 1797 (1968).

[120] C. W. van Hasselt, M. A. C. Devillers, Th. Rasing, and O. A. Aktsipetrov. Second-harmonic generation from thick thermal oxides on Si(111): the influence of multiple reflections. *Journal of the Optical Society of America B* **12,** 33 (1995).

[121] M. Trassin, G. De Luca, S. Manz, and M. Fiebig. Probing ferroelectric domain engineering in $BiFeO_3$ thin films by second harmonic generation. *Advanced Materials* **27,** 4871 (2015).

[122] M. Fiebig, D. Fröhlich, S. Leute, and R.V. Pisarev. Topography of antiferromagnetic domains using second harmonic generation with an external reference. *Applied Physics B: Lasers and Optics* **66,** 265 (1998).

[123] S. Homkar et al. Ultrathin regime growth of atomically flat multiferroic gallium ferrite films with perpendicular magnetic anisotropy. *Physical Review Materials* **3,** 124416 (2019).

[124] Y. R. Shen. Optical Second Harmonic Generation at Interfaces. *Annual Review of Physical Chemistry* **40,** 327 (1989).

[125] V. Jähnke, U. Conrad, J. Güdde, and E. Matthias. SHG investigations of the magnetization of thin Ni and Co films on Cu(001). *Applied Physics B: Lasers and Optics* **68,** 485 (1999).

[126] J. Nordlander et al. Ferroelectric domain architecture and poling of $BaTiO_3$ on Si. *Physical Review Materials* **4,** 034406 (2020).

[127] Z. Li et al. An Epitaxial Ferroelectric Tunnel Junction on Silicon. *Advanced Materials* **26,** 7185 (2014).

[128] K. J. Kormondy et al. Microstructure and ferroelectricity of $BaTiO_3$ thin films on Si for integrated photonics. *Nanotechnology* **28,** 075706 (2017).

[129] T. H. E. Lahtinen, K. J. A. Franke, and S. van Dijken. Electric-field control of magnetic domain wall motion and local magnetization reversal. *Scientific Reports* **2,** 258 (2012).

[130] S. Abel et al. "Multi-Level Optical Weights in Integrated Circuits". In: *2017 IEEE International Conference on Rebooting Computing (ICRC)*. IEEE, 2017, pp. 1–3.

[131] D. Sando, A. Barthélémy, and M. Bibes. $BiFeO_3$ epitaxial thin films and devices: past, present and future. *Journal of Physics: Condensed Matter* **26,** 473201 (2014).

[132] J. Nordlander, A. Maillard, M. Fiebig, and M. Trassin. Emergence of ferroelectricity at the morphotropic phase boundary of ultrathin $BiFeO_3$**,** arXiv:2005.09685 (2020).

[133] D. Sando et al. Designer defect stabilization of the super tetragonal phase in >70-nm-thick $BiFeO_3$ films on $LaAlO_3$ substrates. *Japanese Journal of Applied Physics* **57,** 0902B2 (2018).

[134] H. Yamada et al. Giant Electroresistance of Super-tetragonal $BiFeO_3$-Based Ferroelectric Tunnel Junctions. *ACS Nano* **7,** 5385 (2013).

[135] A. Kumar et al. Probing mixed tetragonal/rhombohedral-like monoclinic phases in strained bismuth ferrite films by optical second harmonic generation. *Applied Physics Letters* **97,** 112903 (2010).

[136] C. Lichtensteiger, J.-M. Triscone, J. Junquera, and P. Ghosez. Ferroelectricity and Tetragonality in Ultrathin $PbTiO_3$ Films. *Physical Review Letters* **94,** 047603 (2005).

[137] J. Nordlander et al. The ultrathin limit of improper ferroelectricity. *Nature Communications* **10,** 5591 (2019).

[138] N. Fujimura, S. Azuma, N. Aoki, T. Yoshimura, and T. Ito. Growth mechanism of $YMnO_3$ film as a new candidate for nonvolatile memory devices. *Journal of Applied Physics* **80,** 7084 (1996).

[139] X. Martí et al. Epitaxial growth of biferroic $YMnO_3$(0 0 0 1) on platinum electrodes. *Journal of Crystal Growth* **299,** 288 (2007).

[140] J. Dho, C. W. Leung, J. L. MacManus-Driscoll, and M. G. Blamire. Epitaxial and oriented $YMnO_3$ film growth by pulsed laser deposition. *Journal of Crystal Growth* **267,** 548 (2004).

[141] Z. Sheng, N. Ogawa, Y. Ogimoto, and K. Miyano. Multiple stable states with in-plane anisotropy in ultrathin YMnO$_3$ films. *Advanced Materials* **22,** 5507 (2010).

[142] S. H. Skjærvø et al. Unconventional Continuous Structural Disorder at the Order-Disorder Phase Transition in the Hexagonal Manganites. *Physical Review X* **9,** 031001 (2019).

[143] D. A. Rusakov et al. Structural Evolution and Properties of Solid Solutions of Hexagonal InMnO$_3$ and InGaO$_3$. *Inorganic Chemistry* **50,** 3559 (2011).

[144] J. A. Mundy et al. Atomically engineered ferroic layers yield a room-temperature magnetoelectric multiferroic. *Nature* **537,** 523 (2016).

[145] Q. N. Meier et al. Global Formation of Topological Defects in the Multiferroic Hexagonal Manganites. *Physical Review X* **7,** 041014 (2017).

[146] S. Salahuddin and S. Datta. Use of Negative Capacitance to Provide Voltage Amplification for Low Power Nanoscale Devices. *Nano Letters* **8,** 405 (2008).

[147] X. Martí et al. Exchange bias between magnetoelectric YMnO$_3$ and ferromagnetic SrRuO$_3$ epitaxial films. *Journal of Applied Physics* **99,** 08P302 (2006).

[148] V. Laukhin et al. Electric-Field Control of Exchange Bias in Multiferroic Epitaxial Heterostructures. *Physical Review Letters* **97,** 227201 (2006).

[149] C. Dubourdieu et al. Thin films and superlattices of multiferroic hexagonal rare earth manganites. *Philosophical Magazine Letters* **87,** 203 (2007).

[150] K. H. Wu et al. Marked enhancement of Néel temperature in strained YMnO$_3$ thin films probed by femtosecond spectroscopy. *Europhysics Letters (EPL)* **94,** 27006 (2011).

[151] N. Jehanathan, O. Lebedev, I. Gélard, C. Dubourdieu, and G. Van Tendeloo. Structure and defect characterization of multiferroic ReMnO$_3$ films and multilayers by TEM. *Nanotechnology* **21,** 075705 (2010).

[152] T. Honke, H. Fujioka, J. Ohta, and M. Oshima. InN epitaxial growths on Yttria stabilized zirconia (111) step substrates. *Journal of Vacuum Science & Technology A: Vacuum, Surfaces, and Films* **22,** 2487 (2004).

[153] T. Kordel et al. Nanodomains in multiferroic hexagonal R-MnO$_3$ films (R=Y,Dy,Ho,Er). *Physical Review B* **80,** 045409 (2009).

[154] J. Nordlander, M. D. Rossell, M. Campanini, M. Fiebig, and M. Trassin. Inversion-symmetry engineering in sub-unit-cell-layered oxide thin films, arXiv:2005.09083 (2020).

[155] T. Ojima, T. Tainosho, S. Sharmin, and H. Yanagihara. RHEED oscillations in spinel ferrite epitaxial films grown by conventional planar magnetron sputtering. *AIP Advances* **8,** 045106 (2018).

[156] Y. Krockenberger et al. Layer-by-layer growth and magnetic properties of $Y_3Fe_5O_{12}$ thin films on $Gd_3Ga_5O_{12}$. *Journal of Applied Physics* **106,** 123911 (2009).

[157] N. Kumar et al. Second harmonic microscopy of monolayer MoS_2. *Physical Review B* **87,** 161403 (2013).

[158] W.-T. Hsu et al. Second harmonic generation from artificially stacked transition metal dichalcogenide twisted bilayers. *ACS Nano* **8,** 2951 (2014).

[159] X. Yin et al. Edge nonlinear optics on a MoS_2 atomic monolayer. *Science* **344,** 488 (2014).

[160] W. Yao, D. Xiao, and Q. Niu. Valley-dependent optoelectronics from inversion symmetry breaking. *Physical Review B* **77,** 235406 (2008).

[161] K. F. Mak, C. Lee, J. Hone, J. Shan, and T. F. Heinz. Atomically Thin MoS_2: A New Direct-Gap Semiconductor. *Physical Review Letters* **105,** 136805 (2010).

[162] S. Remsen and B. Dabrowski. Synthesis and Oxygen Storage Capacities of Hexagonal $Dy_{1-x}Y_xMnO_{3+\delta}$. *Chemistry of Materials* **23,** 3818 (2011).

[163] S. M. Griffin, M. Reidulff, S. M. Selbach, and N. A. Spaldin. Defect Chemistry as a Crystal Structure Design Parameter: Intrinsic Point Defects and Ga Substitution in $InMnO_3$. *Chemistry of Materials* **29,** 2425 (2017).